THE UNIVERSITY *of* EDINBURGH

Phase Transitions in Low-dimensional Driven Systems

André Costa

Doctor of Philosophy
University of Edinburgh
2012

Abstract

The study of non-equilibrium physics is an area of interest since, unlike for their equilibrium counterparts, there exists no general framework for solving such systems. In this thesis I investigate the emergence of structure and front propagation in driven systems, a special type of system within the area of non-equilibrium physics. In particular I focus on three particular one-dimensional models each of which illustrate this in a different way.

The Driven Asymmetric Contact Process (DACP) describes a system where activity is continuously generated at one end of a one-dimensional lattice and where this activity is allowed to spread in one direction along the lattice. In the DACP one observes a propagating wave of activity which appears to abruptly vanish as the system undergoes a phase transition. Using a modified Fisher equation to model the system reveals the continued existence of the propagating wave, now contained within a decaying envelope. Furthermore this establishes relations between properties of the travelling wave and Directed Percolation critical exponents.

The Zero-Range Process (ZRP) is a much studied system exhibiting a condensation transition. In the ZRP individual particles hop along a lattice at rates which depend only on the occupancy of the departure site. Here I investigate a modification of the ZRP where instead the majority of the particles at a site depart during a single hopping event. For this, the Chipping model, a condensate which propagates along the lattice is observed. It is found that this condensation transition is present even for hop rates which fall foul of the condensation requirements of the normal ZRP. Further it is observed that, unlike for normal ZRP, condensation occurs even in the low-density limit. As a result I suggest a condensation mechanism which depends only on the hop rates of low occupancy sites.

The Host-Solute-Vacancy model (HSV) is a three-species system designed to model electromigration in a circuit. As the parameter space is navigated the system undergoes what appear to be two separate phase transitions from a randomly distributed state to a condensed state with either of two structures. To investigate the model new measures for determining condensation are developed. These show that, again, condensation occurs in the low-density limit. By a reduction to a ZRP an effective hop rate of the system is measured. This effective hop rate is found to be a function of the occupancy of a site as a fraction of the total system size. To explain this behaviour I invoke a description whereby there is a step in the hop rate as a function of occupancy.

Through these three examples I illustrate how minor modifications to the dynamics of known systems can result in a new and rich phenomenology. I draw particular attention to the effect of asymmetry in the dynamics.

Declaration

Except where otherwise stated, the research undertaken in this thesis was the unaided work of the author. Where the work was done in collaboration with others, a significant contribution was made by the author. Some of the original work described in this thesis has also been published in [25, 26]. In addition the figures 2.1[1] and 2.2[2], also the original work of the author, have been published in Wikipedia.

A. Costa
August 2012

[1] https://commons.wikimedia.org/wiki/File:Bond_Directed_Percolation.svg
[2] https://commons.wikimedia.org/wiki/File:Contact_Process.svg

Acknowledgements

My foremost thanks go to my supervisors Richard Blythe and Martin Evans for their guidance and continual support. Thanks also for your patience, especially when faced with my sometimes disjoint explanations.

Many thanks also to everyone on the Omniladder along with the inhabitants, past and present, of the 'retirement room' and the 'call centre'. You have provided me with plenty of distractions and ensured that I've stayed on the right side of sanity.

Finally warm thanks to my family for always being there. *Trots att ni befinner er långt borta är ni ändå alltid nära.*

Contents

List of Figures

List of Tables

Chapter 1

Introduction

Although the microscopic constituents of complex systems evolve according to well-known laws of physics, the observable macroscopic properties of the system cannot normally be solved directly. This is due to the fact that the large number of coupled equations of motion of the constituents cannot be solved exactly, meaning that the microscopic dynamics is not fully understood. Instead, one has to introduce a description where the microscopic constituents behave randomly according to probabilistic rules. The system can then be described by a small set of dynamical variables whilst the remaining large number of degrees of freedom are treated as an effective noise. As an example, a fluid comprising $\sim 10^{23}$ interacting particles may—when in thermodynamic equilibrium—be entirely described by a handful of macroscopic variables such as pressure, volume and temperature. Thus, using statistical mechanics, complex systems can be studied through probabilistic (stochastic) models.

A stochastic model is completely described by the probability distribution $P_t(\omega)$ that, at time t, the system is found in the microscopic configuration ω. If the system is at thermal equilibrium, for example through a heat bath which allows the transfer of energy in and out of the system in such a way as to keep the temperatures of the system and the heat bath equal, then the probability distribution is given by the Boltzmann distribution [40]

$$P_{eq}(\omega) = \frac{\exp(-\mathcal{H}(\omega)/k_B T)}{Z_{eq}} \,, \tag{1.1}$$

where $\mathcal{H}(\omega)$ denotes the Hamiltonian of the microscopic configuration ω, k_B the

Boltzmann's constant and T the temperature. Note that $P_{eq}(\omega)$, unlike $P_t(\omega)$, is not time dependent. The *partition function* is a normalising factor given by $Z_{eq} = \sum_\omega \exp(-\mathcal{H}(\omega)/k_B T)$. From this equation we can in principle compute the expectation value of any time-independent observable by summing over the accessible configurations of the system.

It is of particular interest to study systems as they undergo a *phase transition*, i.e. when the microscopic degrees of freedom change their collective behaviour. A well-known example involves the magnetic spins of the Ising model going from a random arrangement (disordered phase) to gradually being aligned in the same direction (ordered phase) as the temperature T is lowered below a critical value T_c. We now identify a macroscopic quantity, the *order parameter*, whose average vanishes on one side of the phase transition and goes away from zero on the other. For the Ising example a suitable order parameter would be the net magnetisation. Phase transitions are generally characterised by whether the order parameter goes to zero continuously or whether it jumps discontinuously at the critical point. Phase transitions are always considered in the *thermodynamic limit* where the number of microscopic configurations tend to infinity. This is because finite-size effects mean that a transition is never truly sharp in a finite system [74].

For a system exhibiting a continuous—also called second order—phase transition we find that close to the critical point, the values of several thermodynamic variables can be expressed as power laws in the distance away from the critical point. For instance the order parameter ϕ in the Ising example above is given by

$$\phi \propto |T - T_c|^\beta \quad \text{for} \quad T < T_c \tag{1.2}$$

close to the critical point T_c, where β is referred to as a *critical exponent*. It has been observed that many seemingly unrelated systems share the same critical behaviour, i.e. have the same set of critical exponents and other scaling behaviour close to the critical point. This has lead to the notion of phase transitions being categorised into different *universality classes* [63].

As an example we may consider the two-dimensional Lennard-Jones fluid [20] system which also takes on the form (1.2), with the order parameter defined as the difference in density between the liquid and the gas, $\phi = \rho_l - \rho_g$. We find that the critical exponent is the same as that for the two-dimensional Ising model. The same is true for other critical exponents thus putting the two systems in the

same universality class [45]. In chapter 2 I will discuss the concept of universality in more depth.

Most systems in nature are not, however, found in thermal equilibrium. Rather they are found in a *non-equilibrium* state where the probability distribution is not given by the Boltzmann distribution. A simple example of such a system would be one which is driven by an outside force. Non-equilibrium systems primarily fall in one of two categories. They are either in the process of relaxing to equilibrium or they are held far from equilibrium. In this thesis I will focus on the latter of these, systems that reach a non-equilibrium steady-state. Since the Boltzmann distribution cannot be used for non-equilibrium systems, one instead has to consider the microscopic dynamics. Since the coupled equations still cannot be solved one has to consider a probabilistic approach to the dynamics, where the relevant variables become the transition probabilities for the system going between different microscopic configurations. The probability distribution $P_t(\omega)$ can then be derived from the *master equation*

$$\frac{\mathrm{d}P_t(\omega)}{\mathrm{d}t} = \sum_{\omega' \neq \omega} \left(\mathcal{W}(\omega' \to \omega) P_t(\omega') - \mathcal{W}(\omega \to \omega') P_t(\omega) \right) \ , \tag{1.3}$$

where $\mathcal{W}(\omega' \to \omega)$ is the *transition rate* from the configuration ω' to ω. Although (1.3) describes a system with continuous time and discrete configurations it may readily be generalised to a continuous configuration space by changing the sum to an integral over the associated probability density function, or to a discreet time by considering transition probabilities instead of transition rates. These probabilities may then, similar to the equilibrium case, be used to predict macroscopic observables. However unlike the equilibrium case no general expression, such as the Boltzmann distribution, exists for solving the master equation.

To clarify exactly what I mean by a non-equilibrium system I will adopt the definition used in [85]. From the form of the master equation in (1.3) it is clear that the equation describes a flow of probability in configuration space. The first term represents a current of probability into configuration ω and the second term is the current out of ω. The steady-state of such a process is reached when $\mathrm{d}P_t(\omega)/\mathrm{d}t = 0$ for all ω, i.e. when there is a zero net flow from any configuration. The process is said to obey *detailed balance* if each term of the sum is identically

zero, i.e.

$$P(\omega')\mathcal{W}(\omega' \to \omega) = P(\omega)\mathcal{W}(\omega \to \omega') \; . \tag{1.4}$$

Thus we say a system is not in thermal equilibrium if the resulting steady-state is such that detailed balance is not satisfied. Alternatively, a non-equilibrium system is one in which there still exist non-zero probability currents—and thus non-zero physical currents—within the steady-state.

Fortunately many of the concepts, such as universality of phase transitions, encountered in the analysis of equilibrium systems generalise to non-equilibrium systems. Some behaviour on the other hand is distinctly different. It has for instance been shown that one-dimensional systems with local dynamics cannot undergo phase transitions when in thermal equilibrium at a finite temperature [45]. By contrast this has been observed in several driven one-dimensional systems [71]. This means that interesting phenomena may be observed even in one dimension where, based on experience from equilibrium systems [12], we would expect exact solutions to be easier to obtain. This thesis focuses exclusively on such one-dimensional driven systems. Furthermore I will consider models with a discretised spatial structure so that the system may be investigated on a lattice. This allows the models to be straightforwardly explored using Monte Carlo simulation methods (see section 2.4).

In this thesis I will study low-dimensional driven systems that undergo well known non-equilibrium phase transitions. An example of such a transition is the absorbing state transition where, as the dynamical rates are changed, the system undergoes a transition from an inactive to an active phase. Another example is a condensation transition where, as the particle density of a homogeneous system is increased past some critical value, the spatial symmetry is broken and an increasing fraction of the particles are found on a single site. By making relatively simple modifications to the dynamics of these systems I am able to induce changes in their phenomenology. I explore such changes—e.g. low-density condensation and transitions becoming discontinuous—by looking at three separate models, each with asymmetric dynamics. To give a foundation to this study I introduce the necessary concepts in chapter 2. In particular I consider phase transitions into absorbing and condensed states and the main universality class for each of these. I also describe how effects, such as increased density, propagate through a system.

I then start by investigating a driven exclusion process in the presence of an active boundary, chapter 3. This model is known to undergo a phase transition which belongs to a universality class normally associated with absorbing state phase transitions. The model exhibits a region of high density which propagates away from the active boundary. I study the dynamics of the propagating front of this high-density region as the system undergoes a phase transition.

Then in chapter 4 I consider a propagating region of high density but now in the context of condensation. Through a simple variation of the much studied zero-range process (introduced in chapter 2) I find that not only does the condensate propagate it also appears that the condensation transition relies on a different mechanism from that normally associated with the zero-range process.

In chapter 5 I introduce the final model, a driven multi-species system undergoing a condensation transition. I show that the system exhibits a rich condensation transition where the condensate displays internal structure. Again we find that the mechanism for condensation is different from both that of the zero-range process and the model described in the previous chapter.

In the final chapter, chapter 6, I bring together the observations from the previous chapters and comment on the modification of system dynamics and resulting phenomena.

Chapter 2

Concepts and Methods

In this thesis I will primarily be dealing with three concepts: absorbing states, propagating wavefronts and condensation. Although these may at the outset seem unrelated we will discover, in this and later chapters, that they are often connected. In this chapter I aim to give an introduction to, and short review of, each of these three concepts thereby setting the stage for more involved implementations in later chapters. In addition I will give an introduction to Monte Carlo simulations as this is a method of analysis which I employ in each of the chapters to follow.

2.1 Absorbing state phase transitions

An area of much interest within non-equilibrium dynamics is that of systems which display an *absorbing state*. Here an absorbing state is defined as entering a configuration which can be reached through the dynamics but which cannot be left once entered. By contrast we say that a system is in the *active state* when it is still free to explore different configurations. Therefore detailed balance cannot be obeyed between an absorbing and an active state and as a result such systems are examples of non-equilibrium processes.

To illustrate this we can consider a simple model for survival/extinction. Consider a population where individuals are either infected or healthy. Infected individuals can either infect healthy individuals or recover and themselves become healthy. Then clearly if at any point all infected individuals have recovered, an absorbing state has been reached where no new infections are possible (extinction

of the infection in the population).

In this section I will give a brief introduction to absorbing state phase transitions. I will focus on the Directed Percolation universality class which has been the focus of much research and is thought to be *"as important as the Ising universality class in equilibrium statistical mechanics"*[1]. Of the many models within this universality class I will look at the Contact Process in particular which, using a similar analogy, was described as *"the Ising model of absorbing state transitions"*[2]. The subject developed here will be the starting point for the Driven Asymmetric Contact Process studied in chapter 3. For a more in-depth review of the area I recommend [55, 81].

2.1.1 The Directed Percolation universality class

On a practical level the Directed Percolation (DP) universality class is of interest since it includes models which have been used to describe a wide variety of systems including percolation, epidemic spreading, wetting, branching and annihilating random walks, reaction-diffusion processes and forest fires [55].

Despite this experimental observation of DP has for a long while proved both difficult and inconclusive [56]. In 2009 however the phase transition between two turbulent states in nematic liquid crystals was conclusively confirmed to be in the DP universality class [106].

The main reason why DP has attracted theoretical interest is that it has become the archetypal class of absorbing state phase transitions. In fact it is so prevalent that it is thought to pertain to any microscopic model exhibiting a continuous phase transition from a fluctuating active phase into a unique absorbing state, in the absence of any additional symmetries, conservation laws or other special attributes [59, 46][3]. Not only have no counterexamples to this conjecture been found but it may be even more general since models violating some of these requirements have still been identified as belonging to DP [54].

It is therefore interesting that although easily defined and very robust the critical behaviour of DP is highly non-trivial. It is even the case that no model

[1] p.7 of [55].
[2] p.161 of [81].
[3] In addition the *DP conjecture* requires the transition to be characterised by a non-negative one-component order parameter and that the dynamics rules are short-ranged.

in the class has been solved exactly even in 1+1 dimensions[4]. There has even been discussion on whether the models are non-solvable [51, 15] and it has been suggested that the critical exponents may be irrational numbers [55]. Still DP is well suited for numerical studies meaning that, although not exactly solved, many features, such as critical exponents, are known to great accuracy (see below).

I will now discuss how the DP universality class is characterised in terms of scaling relations and critical exponents. Following this I will describe two classical models of the universality class. The first being the one from which the universality class got its name and the second being the one which is most commonly studied. Although the latter is the one I shall build upon in later chapters showing both allows us to get a better understanding for the range of models falling within a universality class.

Scaling and critical exponents

To characterise the DP universality class we will consider the scaling behaviour of a spreading process undergoing a phase transition as the parameter p (e.g. the probability that an inactive site gets activated by a neighbouring active site) is decreased past the critical point p_c. For such a system the order parameter is the (average) density of active sites $\phi(t)$ which decays (or grows depending on initial conditions) to a stationary value ϕ_{ss} in the steady-state. The stationary density varies continuously as p is decreased and vanishes at the critical point. Close to the transition the order parameter scales as a power law

$$\phi_{ss} \sim \Delta^{\beta} \,, \tag{2.1}$$

where $\Delta = (p - p_c)$ is the distance from the critical point and β is the critical exponent associated with the steady-state density of activity.

For the special case of a phase transition into an absorbing state there exists a related but subtly different quantity, the probability of ultimate survival P_∞ that a randomly chosen site remains active in the limit of time $t \to \infty$. This probability is finite in the active phase and scales as

$$P_\infty \sim \Delta^{\beta'} \,. \tag{2.2}$$

[4]With the notation $x + 1$ dimensions I mean an x-dimensional system evolving in time.

Additionally there will exist characteristic correlation lengths associated with the process. These are characterised by the two independent variables $\xi_\perp$ and $\xi_\parallel$, the spatial and the temporal length scales. As an example we may consider the density of active sites which, in the active phase, is expected to scale as

$$\phi(t) \sim \phi_{ss} + A \exp(-t/\xi_\parallel) \tag{2.3}$$

close to criticality. These length scales are present on either side of the phase transition and are expected to diverge as

$$\xi_\perp \sim |\Delta|^{-\nu_\perp} \ , \qquad \xi_\parallel \sim |\Delta|^{-\nu_\parallel} \tag{2.4}$$

close to the transition.

As a result of (2.3) and (2.4) we expect the spreading process to exhibit *scale invariance* under some spatial dilation $\mathbf{x} \to \Lambda\mathbf{x}$ followed by the appropriate rescaling of time and distance to criticality:

$$\mathbf{x} \to \Lambda\mathbf{x} \ , \qquad t \to \Lambda^z t \ , \qquad \Delta \to \Lambda^{-1/\nu_\perp}\Delta \ , \qquad \phi \to \Lambda^{-\beta/\nu_\perp}\phi \ , \tag{2.5}$$

where $z = \nu_\parallel/\nu_\perp$ is referred to as the *dynamical exponent*. This allows scale-invariant combinations such as tx^{-z} and $\Delta t^{1/\nu_\parallel}$ to be constructed.

For an absorbing state process there are two additional time dependent quantities which are related to ϕ_{ss} and P_∞. The first is the density of activity $\phi_{all}(t)$ given that all sites are initially active. To distinguish this from $\phi(t)$ above, where the initial condition is not specified, we here add a subscript. The second is the survival probability $P_{one}(t)$ that there is still activity in a system where, initially, there was only one active site. Both of these quantities are expected to scale as

$$\phi_{all}(t) \simeq t^{-\alpha} f(\Delta t^{1/\nu_\parallel}) \ , \qquad P_{one}(t) \simeq t^{-\delta} g(\Delta t^{1/\nu_\parallel}) \ , \tag{2.6}$$

where α (δ) is a critical exponent related to decay (survival) [47, 84][5]. We note that f and g are functions of scale-invariant combinations as shown above. These functions are *universal scaling functions* which have the same functional form in all models belonging to the same universality class. Both tend to constants for

[5]I here use the notation '$\sim$' to indicate the asymptotic behaviour of a function and '$\simeq$' to denote the approximate value of a function/parameter.

small arguments ζ and scale in such a way that the time dependence drops out in the limit $\zeta \to \infty$,

$$f(\zeta) \sim \zeta^{\alpha\nu_\parallel}, \qquad g(\zeta) \sim \zeta^{\delta\nu_\parallel} \ . \tag{2.7}$$

In this limit however we find that $\phi_{all}(t)$ and $P_{one}(t)$ become ϕ_{ss} and P_∞, respectively. Thus from (2.3) and (2.2) we find that

$$\alpha = \beta/\nu_\parallel, \qquad \delta = \beta'/\nu_\parallel \ . \tag{2.8}$$

So we observe that several of the critical exponents, more than shown here[6], are related through simple *scaling relations*. As an aside we note that for a finite system with $N = L^d$ sites the scaling functions also depend on the invariant ratio $\xi_\perp^d/N$ where d is the dimensionality of the system.

Thus we arrive at the definition that non-equilibrium phase transitions in different systems are considered to belong to the same universality class if their critical exponents *and* scaling functions coincide. The described scaling relations further mean that a universality class is normally labelled by what is considered the fundamental set of critical exponents, namely the triplet $\left(\beta, \nu_\perp, \nu_\parallel\right)$, with the addition of the fourth exponent β' for an absorbing state phase transition. It is also worth noting that the critical exponents depend on the dimensionality of the system. We therefore talk about DP having a certain set of critical exponents for some given dimension d.

At this point the above reasoning holds for any non-equilibrium process undergoing a continuous phase transition (including into an absorbing state), assuming that the parameter p and the order parameter $\phi(t)$ are suitably defined. For DP it was shown [47] that due to symmetry under time reversal the single site survival probability $P_{one}(t)$ is exactly equal to the density of active sites $\phi_{all}(t)$ from a process started from a fully activated system. As a result we find that

$$\beta = \beta' \tag{2.9}$$

and so DP is described by only three critical exponents. The time symmetry will become apparent when I introduce the geometrical model for DP in section 2.1.2. We note however that (2.9) does not apply in general for other absorbing state

[6]For a more complete list of critical exponents and scaling functions see Table 4.1 and Appendix B in [54].

phase transitions such as models with several absorbing states. The best estimates for the DP exponents are presented in table 2.1.

	$d = 1$ [61]	$d = 2$ [111, 48]	$d = 3$ [60]	$d \geq 4$
β	0.276486(8)	0.583(3)	0.813(9)	1
$\nu_\perp$	1.096854(4)	0.733(8)	0.584(5)	1/2
$\nu_\parallel$	1.733847(6)	1.295(6)	1.110(10)	1

Table 2.1: Critical exponents for Directed Percolation (DP) in different dimension. Exponents for $d \geq 4$, where $d_c = 4$ is the upper critical dimension of DP, are given exactly by mean-field values. Table taken from [54].

2.1.2 Directed Percolation

The geometrical model for Directed Percolation was introduced in 1957 [19] as a model for the influence of a medium on the percolation of a fluid through it. Here we consider a two-dimensional lattice where the layers are connected by diagonal oriented bonds, see Fig. 2.1. Bonds are either open with some probability p, or closed with probability $1 - p$. The state of any specific bond is taken to be independent of the state of any other bond. Thus designating a site to be the source we may construct a cluster of sites which are all connected to the source by a directed path. The different phases of the system are characterised by the *percolation probability*, $P(p)$, the probability that there exists a directed path extending arbitrarily far away from the source. For all systems where the probability of bonds being open is less then some critical value, $p < p_c$, the percolation probability is zero.

Whereas the geometrical description brings to mind a liquid flowing, under gravity, through porous rock one can also view DP as the activity of a one-dimensional lattice evolving over (discrete) time. In this description each lattice site is either active (A) or inactive ($\emptyset$). Sites can become inactive ($A \to \emptyset$) or activate a neighbouring site ($A + \emptyset \to A + A$). Since spontaneous activation ($\emptyset \to A$) is not allowed we see that if, at any time, all sites are inactive then the system can never leave that state. Thus it becomes apparent that DP describes a system with an absorbing state.

In this realisation of DP the time reversal symmetry becomes apparent when we consider Fig. 2.1 as a 1+1 system with time increasing as we move down the

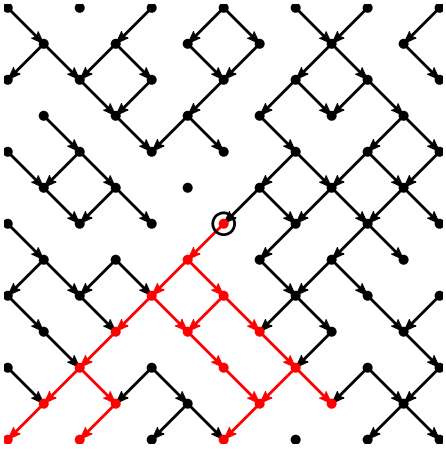

Figure 2.1: Directed Percolation as a geometrical model in two dimensions. Bonds can either be open (solid line) or closed (no line). The cluster of sites connected by a directed path (following the arrows) to the source (circled point) is indicated in red.

y-axis. A reversal of time is then equivalent to reversing the direction of the path. Thus any active sites at time t_0 must be exactly those from which a cluster at some later time $t > t_0$ originate.

2.1.3 The Contact Process

The Contact Process was first introduced in 1974 [52] as a model for epidemic spreading in the absence of immunisation. Here however I shall describe it using the previous language of active and inactive sites on a lattice. The model is defined as a lattice, evolving over (continuous) time, where an active site ($\tau_i(t) = 1$) can become inactive ($\tau_i(t) = 0$), with rate 1, or activate a neighbouring inactive site, with rate r/z where z is the number of nearest neighbours to the activating site. Fig. 2.2 illustrates the model in 1+1 dimensions.

Even though the model has not been solved exactly, numerical and approximate techniques have shown that the model exhibits a phase transition [75, 30] which in turn has been shown to be continuous [14]. As r is increased the system goes from a phase where the lattice is completely inactive (absorbing) to one where there are still active sites in the large time limit, $t \to \infty$. Thus the order parameter is the (average) density of active sites in the limit of an infinite system

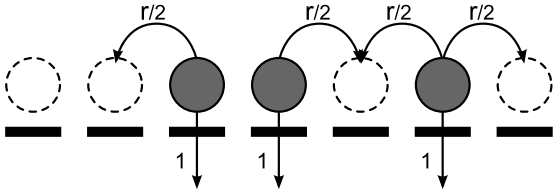

Figure 2.2: The Contact Process (on a 1D lattice): Active sites are indicated by grey circles and inactive sites by white/dashed circles. Active sites can activate inactive sites to either side of them at a rate $r/2$ and become inactive at a rate 1.

as time tends to infinity

$$\phi = \lim_{t\to\infty} \lim_{N\to\infty} \frac{1}{N} \sum_{i=1}^{\infty} \langle \tau_i(t) \rangle \ , \tag{2.10}$$

where the angle brackets indicate an ensemble average. Note that the order of the limits matter since the contact process is guaranteed to die out in the limit $t \to \infty$ for a finite lattice. Close to criticality we find that the density scales as

$$\phi = \begin{cases} 0 \ \text{ for } \ r \leq r_c \\ |r - r_c|^{\beta} \ \text{ for } \ r > r_c \end{cases} \tag{2.11}$$

where $r_c = 3.29784(2)$ [54] (in 1D) and the critical exponent β has been found to agree with that of DP (in e.g. [62]), see table 2.1. Numerical studies of the remaining critical exponents have further been used to show that the contact process is in the DP universality class.

Varieties of the contact process have been studied, an asymmetric version where left and right activation rates differed was studied by Schonmann [98] and in 2001 a driven asymmetric version (DACP) was introduced, and shown to belong to the DP universality class [15]. We shall come back to the DACP model in chapter 3.

2.2 Non-linear wavefront propagation

In a spatially extensive system it is often of great interest to understand how the activity, once introduced, spreads throughout the system. When *diffusion*

plays an important role in the spreading process we find that many biological, chemical and mechanical systems exhibit spreading as described by a *travelling wave* propagating through the system. As we shall see, later in this section, this also has strong ties to Directed Percolation phenomena. Here we take travelling wave to mean a wave which travels without change of shape, i.e.

$$\rho(x,t) = \rho(x-ct) = \rho(z) \text{ for } z = x - ct \,, \tag{2.12}$$

where c is the, constant, speed of propagation. Thus if if we change to a reference frame travelling at speed c the wave would appear to be stationary.

However a system governed by a linear parabolic equation, such as the diffusion equation

$$\frac{\partial \rho}{\partial t} = D\frac{\partial^2 \rho}{\partial x^2} \,, \tag{2.13}$$

has no physical solution which allows a travelling wave since solutions of the form (2.12) require $\rho(z) = A + Be^{-\lambda z}$ where A, B and $\lambda = c/D$ are all constants. For $\rho(z)$ not to become unbounded in the limit $z \to \pm\infty$ (i.e. the large t or x limit) we require $B = 0$ thus leaving as the only solution $\rho(z) = A$, which is not a propagating wave.

We therefore consider a system which, in addition to diffusion, allows some reaction kinetics. The spread of the activity is then described by the non-linear *reaction diffusion equation*. In one dimension the equation becomes

$$\frac{\partial \rho}{\partial t} = D\frac{\partial^2 \rho}{\partial x^2} + f(\rho) \,, \tag{2.14}$$

where ρ is the density describing the activity, $f(\rho)$ represents the kinetics and D is the diffusion coefficient, here taken to be constant.

Now, depending on the form of $f(\rho)$, travelling wave solutions are possible. As a result reaction diffusion equations, and the associated non-linear wavefronts, have been studied extensively by both physicists and mathematicians.

To illustrate what a kinetic term may look like we now consider the basic kinetics of directed percolation (section 2.1.2). In this example there are two processes $A + \emptyset \to A + A$ occurring at rate r and $A \to \emptyset$ at rate 1. For this example we will consider the system to be well mixed so that any A, $\emptyset$ pair may interact. Heuristically we can see that the rate at which the second process

occurs is clearly proportional to the particle density ρ_A whereas the first is also proportional to the density of empty sites $\rho_\emptyset = 1 - \rho_A$. Thus, dropping the A subscript, the kinetics are described by

$$f(\rho) = +r\rho(1-\rho) - \rho \; . \tag{2.15}$$

As we shall see below this is the form of the kinetic term in the Fisher-KPP equation.

In this section I shall focus on the simplest case of a non-linear equation resulting in such a propagating wavefront. For more general information I suggest [109] for a review or [87] for an applied (biology) approach.

2.2.1 Fisher-KPP waves

The simplest case of the reaction diffusion equation which yields a propagating wavefront is described by the *Fisher-KPP*[7] equation:

$$\frac{\partial \rho(x,t)}{\partial t} = D\frac{\partial^2 \rho}{\partial x^2} + \alpha\rho(1-\rho) \; , \tag{2.16}$$

where ρ is some density field whilst α and D are positive parameters. For this reason Fisher-KPP has become the prototype equation for propagating wavefronts.

The particular choice of $f(\rho) = \alpha\rho(1-\rho)$ in (2.14) was suggested by Fisher in 1937 [37] in his study of the dynamics of the spread of a favoured gene in a population. In the same year Kolmogorov, Petrovskii, Piskunov also released a paper [69] which was focused on the analytics of this equation. From this point the equation was mainly studied by mathematicians resulting in the comprehensive set of results published in [6, 7]. Within the physics community the interest in the equation was reawakened in the 1980s when it was found to be applicable to fluid dynamics and plasma physics. However, travelling waves in chemical reactions were first reported by Luther in 1906 [77][8]. Luther obtained the wavespeed in terms of experimental parameters but the analytic form is the same as that which Fisher and Kolmogorov *et al.* found starting from equation (2.16) [101].

[7] Here Fisher-KPP stands for Fisher-Kolmogorov-Petrovskii-Piskunov. It is alternatively called the *Fisher-Kolmogorov* or *Fisher's* equation.

[8] The paper was rediscovered and translated from German in 1987 [5].

We may further identify that the kinetic term for directed percolation in (2.15) above is of the same form as that used here. To see this let $\alpha = (r-1)$ and rescale $\rho \to \frac{r}{r-1}\rho$ in (2.16) to recover (2.14) with $f(\rho)$ given by (2.15). I shall return to the link between directed percolation and the Fisher-KPP equation towards the end of this subsection.

By inspection of (2.16) we see that the steady-states of the equation occur when $\rho = 0$ or 1. A Taylor expansion of $f(\rho)$ near $\rho = 0$ shows that $f(\rho) \simeq f'(0)\rho = \alpha\rho$. Thus $f(\rho)$ drives ρ away from zero meaning $\rho = 0$ is the unstable state. Thus the equation describes a wavefront invading the $\rho = 0$ phase leaving everything behind in the $\rho = 1$ phase, Fig. 2.3.

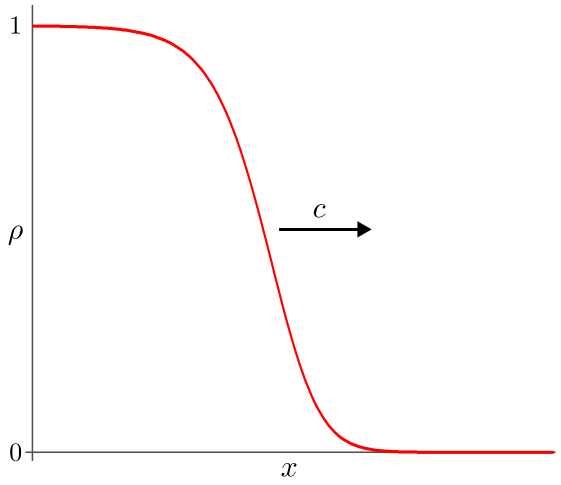

Figure 2.3: The Fisher-KPP wave: A wavefront invades the $\rho = 0$ state and leaves everything behind in the $\rho = 1$ state. The wavefront travels with the linear spreading velocity c.

To find the velocity at which the wave travels one first assumes a travelling wave form solution (2.12) to the Fisher-KPP equation. Without loss of generality we assume that the initial conditions are such that $\rho(-\infty, 0) = 1$, $\rho(+\infty, 0) = 0$ so that the front moves to the right and $c > 0$. Thus we get an ordinary differential equation

$$D\rho'' + c\rho' + \alpha\rho(1-\rho) = 0\,, \tag{2.17}$$

where primes denote differentiation with respect to z. The equation is then linearised for large z where ρ is small. Solutions are then of the form $\rho = e^{-\lambda z}$

with $\lambda \in \mathbb{R}_+$ given by

$$\lambda = \frac{c \pm \sqrt{c^2 - 4D\alpha}}{2D} \ . \tag{2.18}$$

For λ to be real we require $c \geq 2\sqrt{D\alpha} = c_{\min}$. Thus we find that there is a family of travelling wave solutions of the Fisher-KPP equation, each with a different wavefront velocity, the asymptotic linear spreading velocity, c. To reiterate, c is the asymptotic rate at which initially local activity will spread, as determined by linearising the non-linear equations about the unstable state.

I will now show an important feature of systems described by the Fisher-KPP equation, namely that for an initial condition where the front is *'steep'* the linear spreading velocity takes on the value $c = c_{\min}$ [109]. For the purpose of this introduction it is sufficient to note that any initial condition with compact support, whereby the front is continuous and contained within a finite range of x, may be considered steep [109]. Henceforth this is the only initial condition we shall consider. I shall however comment on the steepness requirement again after I have shown how the selection principle is used to derive the linear spreading velocity, below.

The Selection Principle: Deriving the linear spreading velocity

In this derivation I will largely follow a path similar to that in [109]. We start by assuming that the homogeneous stationary state $\rho = 0$ is linearly unstable.

Taking the spatial Fourier transform of ρ

$$\tilde{\rho}(k,t) = \int_{-\infty}^{\infty} \rho(x,t) e^{-ikx} \mathrm{d}x, \tag{2.19}$$

and substituting in the ansatz

$$\tilde{\rho}(k,t) = \bar{\rho}(k) e^{-i\omega(k)t} \ , \tag{2.20}$$

gives the dispersion relation $\omega(k)$[9] of Fourier modes of the linearised equation. We note that $\bar{\rho}(k)$ is simply the Fourier transform of the initial condition. That $\rho = 0$ is linearly unstable is then equivalent to there existing some range of k-values for which $\mathrm{Im}[\omega(k)] > 0$ such that the Fourier modes grow with time.

[9]We shall assume that the dispersion relation only has a single branch of solutions. For a discussion on more than one branch of solutions see [109].

Let the speed of the wavefront, the linear spreading velocity, be v^*. Now take the inverse Fourier transform of (2.20) and change to a reference frame moving with the wave, through $\xi = x - v^*t$,

$$\rho(\xi,t) = \frac{1}{2\pi}\int_{-\infty}^{\infty}\bar{\rho}(k)e^{ikx-i\omega(k)t}\mathrm{d}k \tag{2.21}$$

$$= \frac{1}{2\pi}\int_{-\infty}^{\infty}\bar{\rho}(k)e^{ik\xi-i[\omega(k)-kv^*]t}\mathrm{d}k\ . \tag{2.22}$$

In the co-moving frame we should observe a stationary state, thus requiring ρ to neither increase nor decrease exponentially as $t \to \infty$, for finite ξ. The large-time limit suggests the use of a saddle-point approximation to deform the contour to go through the saddle-point k^* in the complex k-plane where the temporal part of the exponent in (2.22) varies the least with k. As t grows the integral then becomes increasingly dominated by contributions from the region near k^*, defined through:

$$\frac{\mathrm{d}}{\mathrm{d}k}[\omega(k)-kv^*]\bigg|_{k*} = 0 \Rightarrow v^* = \frac{\mathrm{d}\omega(k)}{\mathrm{d}k}\bigg|_{k*}\ . \tag{2.23}$$

Assuming $\bar{\rho}(k)$ is an *entire function* (analytical in every finite region of k-space) the dominant term in the integral is given by $e^{-i[\omega(k^*)-k^*v^*]t}$. However, since we further required this term neither grow nor decay exponentially it follows that

$$\mathrm{Im}[\omega(k^*)-k^*v^*] = 0 \Rightarrow v^* = \frac{\mathrm{Im}[\omega(k^*)]}{\mathrm{Im}[k^*]}\ . \tag{2.24}$$

Now return to the Fisher-KPP equation (2.16). Linearising it about the unstable state, $\rho = 0$, gives

$$\frac{\partial\rho}{\partial t} = D\frac{\partial^2\rho}{\partial x^2} + \alpha\rho + \mathcal{O}(\rho^2)\ . \tag{2.25}$$

Taking the Fourier transform (2.19) of (2.25) and substituting in the ansatz (2.20) we find that the dispersion relation for the Fisher-KPP is

$$-i\tilde{\rho}\omega(k) = \alpha\tilde{\rho} - Dk^2\tilde{\rho} \Rightarrow \omega(k) = i(\alpha - Dk^2)\ . \tag{2.26}$$

Using the dispersion relation (2.26) in the saddle-point equation (2.23) gives the following expression for the velocity:

$$v^* = -2iDk^*\ . \tag{2.27}$$

Denote the imaginary and real parts of k^* by k_I and k_R respectively and note that, since v^* must be real, (2.27) requires $k^* = ik_I$. Putting the dispersion relation (2.26) into the self-consistency requirement (2.24) and equating this to (2.27) gives

$$2Dk_I = \frac{\alpha + Dk_I^2}{k_I} \Rightarrow k_I^2 = \frac{\alpha}{D} \Rightarrow k^* = i\sqrt{\frac{\alpha}{D}} \,. \tag{2.28}$$

It thus follows from (2.27) that the asymptotic linear spreading velocity is $v^* = 2\sqrt{D\alpha} = c_{\min}$.

We note that, as before, this is the *linear* spreading velocity obtained by linearising the fully non-linear equation (2.16). The only additional constraint needed to identify the unique solution v^* from the family of solutions $c \geq c_{\min}$ is that the initial condition is steep. We may now link the steepness requirement to our assumption that $\bar{\rho}(k)$, the Fourier transform of the initial condition, is an entire function. Initial conditions such as a delta function or compact support clearly satisfy the $\bar{\rho}(k)$ assumption and thus also fulfil the steepness requirement. The explicit definition of a steep initial condition is given in [109] as one where

$$\lim_{x\to\infty} \rho(x, t = 0)e^{\lambda^* x} = 0 \,, \tag{2.29}$$

where $\lambda^* = \mathrm{Im}[k^*]$. Or as van Saarloos puts it[10]:

> According to the linear dynamics, initial conditions whose exponential decay rate ("steepness") λ is larger than λ^* lead to profiles which asymptotically spread with the linear spreading velocity v^*. Initial conditions which are less steep than λ^* evolve into profiles that advance with a velocity $v_{\mathrm{env}} > v^*$.

Fisher-KPP and Directed Percolation

At this point it is worth noting the connection between the Fisher-KPP equation and Directed Percolation. We saw in section 2.1.2 that DP can be described by a reaction diffusion equation obeying the rules

$$\begin{aligned} A &\to \emptyset \,, \\ A + \emptyset &\rightleftharpoons A + A \,. \end{aligned} \tag{2.30}$$

[10] p.49 of [109].

In [59] it was shown that in the continuous limit such a system may be described by the Langevin equation (using the Itō prescription)

$$\frac{\partial \rho(x,t)}{\partial t} = D\frac{\partial^2 \rho}{\partial x^2} + \alpha\rho(1-\rho) + \Gamma_0\sqrt{\rho}\eta(x,t) \ , \tag{2.31}$$

where η is Gaussian white noise defined through

$$\begin{aligned} \langle \eta(x,t) \rangle &= 0 \ , \\ \langle \eta(x,t)\eta(x',t') \rangle &= \delta(x'-x)\delta(t'-t) \ . \end{aligned} \tag{2.32}$$

Thus we see that the mean-field description ($\Gamma_0 = 0$) of the DP system has the same form as the Fisher-KPP equation. Note that the noise term in the Langevin equation is real, unlike the 'imaginary' noise which appears in Langevin equations for annihilation processes [57].

This equivalence is an often quoted but rarely derived result, for a derivation of (2.31) from (2.30) I therefore recommend appendix A of [9]. The essence of the derivation is to derive a field theory for (2.30) and (2.31) and show that they are equivalent. This is done by writing the probability of observing the evolution of the density $\rho(x,t)$ of large scale behaviour as $\mathcal{P}\left[\rho(x,t)\right] = \int \mathcal{D}\left[\hat{\rho}\right] \exp[-S]$. The theories are then deemed to be equivalent if it can be shown that the action S is the same in either case.

2.3 Condensation transitions

The last concept which we shall consider in this chapter is that of *condensation*. I will especially consider real space condensation which I define as the process whereby a finite fraction of the particles (or mass) in the system accumulate onto the same site. These phenomena are abundant in nature and as such it is a natural area of study. As an experimental example we may consider granular particles uniformly distributed between compartments where there is some means of moving from one compartment to another. Once the container is shaken the granules spontaneously start to cluster (condense) into one of the compartments [31, 76, 108]. Dynamical models exhibiting spatial condensation include biological flocking behaviour [88, 110], the aggregation of wealth by few individuals in macroeconomics [21] and jamming in traffic [32, 23]. I will illustrate

the statistical mechanics view of condensation by briefly looking at condensation in the Bose gas equilibrium system. Even though this describes condensation in phase space it serves as a reference when we afterwards take a closer look at the zero-range process, a simple one-dimensional non-equilibrium system undergoing a spatial condensation transition.

2.3.1 Bose-Einstein condensation

By now Bose-Einstein condensation is a well known subject which is discussed in several textbooks, here I will follow the approach used in [63] and [8]. For this example we will think of an ideal Bose gas simply as being a gas of non-interacting and indistinguishable particles, without any internal degrees of freedom, in contact with a particle and energy reservoir. Thus the microstates of the gas are described by $r = \{n_i\}$, where $n_i = 0, 1, 2 \dots$ is the occupation number of single particle state i. Thus the grand canonical partition function is given by the product of single particle partition functions

$$\begin{aligned} \mathcal{Z} &= \prod_i \mathcal{Z}_i \ , \\ \mathcal{Z}_i &= \sum_{n_i=0}^{\infty} \exp\left[-\beta n_i(\epsilon_i - \mu)\right] = \frac{1}{1 - z\exp[-\beta\epsilon_i]} \ \text{ for } \ \epsilon_i > \mu \ . \end{aligned} \tag{2.33}$$

Here μ is the chemical potential which gives the fugacity z through $z = e^{\beta\mu}$ where $\beta = (k_B T)^{-1}$. The fugacity is determined so as to fix the (average)[11] total particle number through $N(z) = z\partial \ln \mathcal{Z}/\partial z = \sum_i \overline{n_i}$ where the average occupancy is

$$\overline{n_i} = \frac{1}{z^{-1}\exp[\beta\epsilon_i] - 1} \ . \tag{2.34}$$

Now approximate the sum by an integral over energy space to find

$$N = \sum_i \overline{n_i} \to \int_0^{\infty} \frac{g(\epsilon)}{\exp[\beta(\epsilon - \mu)] - 1} \mathrm{d}\epsilon \ , \tag{2.35}$$

where $g(\epsilon)$ is the density of states. For a boson without any internal degrees of freedom, $g(\epsilon) \propto V\epsilon^{1/2}$ (in three dimensions)[12]. Since the average occupancy

[11] For a sufficiently large N fluctuations about this number are negligible.

[12] This is found by calculating the energy of a particle in a 3D box of volume V.

must be positive even for low-energy states it follows that μ must be negative. Thus we find that as $\beta\mu$ increases towards zero, $z \to 1$, the integral increases until it finally reaches a maximum for $\mu = 0$ at a non-zero temperature T_c [13]. Inserting the value for $g(\epsilon)$ into the above integral and changing to a dimensionless integration variable $x = \epsilon/\beta$ the maximum density is found at

$$\rho_{\max} = N/V = CT_c^{-3/2} \int_0^\infty \frac{x^{1/2}}{\exp[x] - 1} \mathrm{d}x = DT_c^{-3/2} \,, \tag{2.36}$$

where C and D are both constants. However since the particles are non-interacting there should be nothing preventing us from adding more particles to the system. Similarly for $T < T_c$ it would appear that (2.35) cannot be satisfied. To account for the missing density we need to consider the $\epsilon = 0$ state. i.e.

$$\overline{n_0} = \frac{1}{z^{-1} - 1} \,. \tag{2.37}$$

Since $g(0) = 0$ the contribution from this term is lacking in (2.35) and a correction term must be introduced,

$$N = \overline{n_0} + \int_0^\infty \frac{g(\epsilon)}{\exp[\beta\epsilon] - 1} \mathrm{d}\epsilon \;\text{ for }\; T < T_c \,. \tag{2.38}$$

Thus as the temperature decreases below T_c a finite fraction of all the particles may be found condensing into the ground state.

In summary, there is an apparent maximum density which can be supported by the system. At densities above this, additional particles go into the condensate.

2.3.2 The Zero-Range Process

The Zero-Range Process (ZRP) describes a system where interacting, indistinguishable, particles occupy sites on a lattice. Each site can hold an unlimited number of particles. Particles are allowed to hop between neighbouring sites at a rate which depends on the departure site only. In particular we consider rates which depend on the occupancy, n, of the departure site. Although the dynamics appear very simple the system nevertheless displays interesting behaviour such as a condensation transition. However what makes this a key model in the study

[13] This is due to $g(\epsilon) \propto \epsilon^{1/2}$. We find that T_c is defined through $N = \int_0^\infty \frac{g(\epsilon)}{\exp[\epsilon/k_B T_c] - 1} \mathrm{d}\epsilon$ [8].

of non-equilibrium systems is that the steady-state is described, exactly, by a factorised form. As a result several of its properties can be analysed exactly and the results can be used to better understand non-equilibrium systems in general.

The ZRP was first introduced by Spitzer [104] in 1970. Spitzer solved the model for its steady-state for the case of a general hop rate $u(n)$ on a finite lattice. This was extended to infinite lattices [1] and the system was later shown, for spatially homogeneous hop rates, to undergo a condensation transition [33]. For a density ρ above some critical value ρ_c the system phase separates into a homogeneous background density at ρ_c with all the remaining particles, the condensate, at a single site. This transition has since been thoroughly studied and explained, see e.g. [50]. Since its introduction the ZRP has been used to describe a large selection of different phenomena. Amongst these can be mentioned a model for buses serving a single route which shows how the buses cluster together, thus leaving passengers waiting for longer [89]. The link to ZRP comes from considering the distances between buses as particles in the ZRP. Further examples include interface growth, polymer dynamics, sandpile dynamics and the dynamics of avalanches [33]. An in-depth review of ZRP and related systems can be found in [33] and the more recent [34].

The particular version of ZRP considered here is defined on a homogeneous one-dimensional lattice with L sites and periodic boundary conditions. We only consider the asymmetric dynamics whereby one particle may hop from site i to site $i+1$ with rate $u(n_i)$ where n_i denotes the number of particles at site i *before* the hop. The total number of particles are conserved such that $N = \sum_i n_i$. See Fig. 2.4a for an illustration.

It is also worth noting that the ZRP can be mapped onto a *simple exclusion process*. This is done by considering the sites of the ZRP becoming particles in the exclusion process whilst each particle in the ZRP becomes an unoccupied site, Fig. 2.4. Thus it follows that the densities $\rho = N/L$ in the two models are related through

$$\rho_Z = \frac{N_Z}{L_Z} = \frac{L_E - N_E}{N_E} = \frac{1-\rho_E}{\rho_E} \,. \tag{2.39}$$

where the Z and E subscripts denote ZRP and exclusion process respectively.

The resulting exclusion process is one where each particle jumps to the neighbouring empty site with a rate proportional to the number of empty sites in front of it. Thus we observe that the dynamics introduce long range interactions.

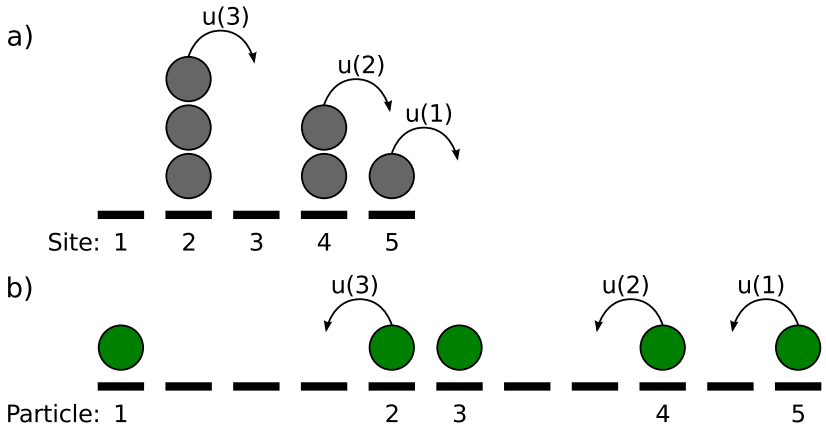

Figure 2.4: The one-dimensional ZRP (a) and its mapping to an asymmetric simple exclusion process (b).

Whereas this mapping is useful for connecting ZRP phenomena to other models there is one caveat. Since the mapping requires the particle order to be preserved in the exclusion process it only really holds in one dimension. Towards the end of this section we will observe that this mapping plays a key role in generalising ZRP results to other non-equilibrium systems.

ZRP and the steady-state

A key property of the ZRP is that the steady-state is given by a simple factorised form. It is therefore worthwhile deriving this explicitly. The calculations below largely follow a similar path to that in [33] and [34].

A factorised steady-state signifies that the steady-state probability $P(\{n_i\})$ of finding the system in a configuration $\{n_i\} = n_1, n_2, \ldots, n_L$ is given by a product of scalar factors $f(n_i)$. Thus

$$P(\{n_i\}) = Z_{L,N}^{-1} \prod_{i=1}^{L} f(n_i) \delta \left(\sum_{i=1}^{L} n_i - N \right) , \tag{2.40}$$

where $Z_{L,N}$ is a normalisation factor such that the sum of the probabilities for all configurations containing N particles is one. Using the δ-function to ensure

particle numbers are conserved we find

$$Z_{L,N} = \sum_{\{n_i=0\}}^{\infty} \prod_{i=1}^{L} f(n_i) \delta \left(\sum_{i=1}^{L} n_i - N \right) . \tag{2.41}$$

For the ZRP, as defined above, we can prove that the steady-state probability satisfies (2.40) by balancing the probability current due to hops into a particular configuration with that out of the same configuration;

$$0 = \sum_{i=1}^{L} \left[u(n_{i-1}+1) P(\dots, n_{i-1}+1, n_i - 1, \dots) - u(n_i) P(\dots, n_i, \dots) \right] \theta[n_i - 1] , \tag{2.42}$$

where $\theta[n]$ is the normal Heaviside function

$$\theta[n] = \begin{cases} 0 \ \text{ for } \ n < 0 , \\ 1 \ \text{ for } \ n \geq 0 . \end{cases} \tag{2.43}$$

Here the Heaviside function ensures that only sites which are occupied prior to a hop out of them (second term), or after a hop into them (first term), are considered. Substituting (2.40) into (2.42) and equating each term in the sum whilst cancelling common factors gives

$$\begin{aligned} & u(n_{i-1}+1) f(n_{i-1}+1) f(n_i - 1) = u(n_i) f(n_{i-1}) f(n_i) \\ \Rightarrow \quad & u(n_{i-1}+1) \frac{f(n_{i-1}+1)}{f(n_{i-1})} = u(n_i) \frac{f(n_i)}{f(n_i - 1)} = \text{constant } \forall \ i . \end{aligned} \tag{2.44}$$

The constant can, without loss of generality, be set to 1 giving

$$f(n_i) = \frac{f(n_i - 1)}{u(n_i)} \tag{2.45}$$

which, taking $f(0) = 1$, can be iterated to give

$$f(n) = \prod_{i=1}^{n} u(i)^{-1} \ \text{ for } \ n > 0 . \tag{2.46}$$

Thus the equations (2.40), (2.41) and (2.46) fully describe the steady-state of the ZRP. Since the steady-state behaviour is determined by the form of $f(n)$ any form

could be chosen and the hop rates then inferred through (2.45). As a result any model with a factorised steady-state, integer site variables and a conservation law can be analysed through an equivalent ZRP which in turn may be solved exactly. Even for models where a mapping to ZRP cannot be done exactly a factorised steady-state can be useful as a coarse grained approach which allows a ZRP analysis of e.g. condensation transitions.

As we shall see in section 4.2.1 this result was further generalised [36, 114] to models where instead of an integer number of particles on each site we consider a continuous mass where an arbitrary amount may move from one site to another.

ZRP and the condensation transition

As in the case of Bose-Einstein condensation the key to understanding the condensation transition is through the partition function. In the ZRP the analogue to the canonical partition function of a thermodynamic system is the normalisation factor $Z_{L,N}$ defined, for our homogeneous system, in (2.41). The following calculation largely follows the procedure in [34].

Using the integral representation of the Kronecker delta we can write the normalisation as

$$Z_{L,N} = \oint_{|z|\leq\beta} \frac{\mathrm{d}z}{2\pi i} \frac{[F(z)]^L}{z^{(N+1)}} \quad \text{for} \quad F(z) = \sum_{n=0}^{\infty} z^n f(n) \,, \tag{2.47}$$

where β is the radius of convergence of $F(z)$ [14]. We now note that $z \leq \beta$ so as not to enclose the singularity at $z = \beta$. For large L, N the normalisation is dominated by the saddle point of the integral at which the value of z is the fugacity. The equation for the saddle point is

$$\frac{\partial}{\partial z} \frac{[F(z)]^L}{z^{(N+1)}} \bigg|_{z=z^*} = 0 \tag{2.48}$$

which, for $N \gg 1$, after dropping the z^* notation, simplifies to

$$\rho = \frac{N}{L} = \frac{zF'(z)}{F(z)} \,. \tag{2.49}$$

[14] Note that this is *not* the same β as that defined in section 2.3.1.

As an aside we note that this is equivalent to transforming our canonical partition function (2.41) into a grand canonical partition function through $\mathcal{Z}_L(z) = \sum_{n=0}^{\infty} z^n Z_{L,n} = [F(z)]^L$. The particle number, and thus the density, is then fixed by choosing the fugacity such that $N = \langle n \rangle = z\frac{\partial \ln \mathcal{Z}_L(z)}{\partial z}$, where $\langle n \rangle$ denotes the (average) total particle number in the grand canonical ensemble.

Now recall that for $F(z)$, as defined in (2.47), to converge z must be restricted to $z \leq \beta$. However since (2.49) is an increasing function of z this means that there exists a maximal value of the density for which a solution to (2.49) exists. The maximal density ρ_c is defined through

$$\rho_c = \frac{\beta F'(\beta)}{F(\beta)} \, . \tag{2.50}$$

If ρ_c is infinite then there exists a corresponding z for any density. If however ρ_c is finite then for $\rho > \rho_c$ equation (2.49) can no longer be satisfied. This corresponds to a spontaneous symmetry breaking whereby one of the sites is selected to hold a finite fraction, $N(\rho - \rho_c)$, of the particles. That is, as the density is increased the system undergoes a condensation transition. The loss of homogeneity is what makes (2.49) no longer be valid. Again we can draw the parallel to the case of Bose-Einstein condensation where we find that the equation for the total number of particles (2.35) appears to not be satisfied since it does not take the condensate into account.

To find the condensation condition in terms of hop rates we consider when the ratio in (2.49) is finite. Combining this with the definition of $F(z)$ in (2.47) gives

$$\frac{zF'(z)}{F(z)} = \frac{\sum_{n=0}^{\infty} n z^n f(n)}{\sum_{n=0}^{\infty} z^n f(n)} \, . \tag{2.51}$$

For an $f(n)$ which goes like $f(n) \sim n^{-|\alpha|}$ and does not alternate in sign we observe that condensation, i.e. a finite ratio (2.51), is controlled by whether $zF'(z)$ converges for some value of z. This is shown by writing $zF'(z) = \sum_{n=0}^{\infty} a_n$, $F(z) = \sum_{n=0}^{\infty} b_n$ and using the *direct comparison test* [94] which states that: since $|a_n| \geq |b_n| \ \forall n > 1$ if follows that if $F(z)$ diverges then $zF'(z)$ also fails to (absolutely) converge. Thus either both diverge, in which case the ratio diverges since $a_n/b_n = \mathcal{O}(n)$, or $F(z)$ converges and the convergence of $zF'(z)$ therefore determines whether the ratio is finite.

The ratio of successive terms in the $zF'(z)$ series is given by

$$\frac{(n-1)f(n-1)}{nzf(n)} = \frac{u(n)}{z}\left(1-\frac{1}{n}\right) \tag{2.52}$$

where we use (2.45) to relate $f(n)$ to the hop rates $u(n)$. *Bertrand's Test* [113] tells us that such a series converges if the above ratio decays more slowly than $(1+1/n)$. For condensation to occur we therefore require convergence at $z=\beta$ and thus that the hop rate decays more slowly than

$$u(n) = \beta\left(1+\frac{2}{n}\right) + \mathcal{O}\left(\frac{1}{n^2}\right) \text{ for } n \gg 1 \,. \tag{2.53}$$

Thus using the generalised form for the ZRP hop rate

$$u(n) = \left(1+\frac{b}{n^\sigma}\right) \,, \tag{2.54}$$

we find that, for a large enough density, condensation is possible if $0<\sigma<1$ and $b>0$ or if $\sigma=1$ and $b>2$ [89]. In addition condensation also occurs for any density in the trivial case where $\beta=0$.

In [64] this result was coupled to the previously mentioned mapping of the ZRP to a simple exclusion process, Fig. 2.4. This resulted in the formulation of a criterion for phase separation in one-dimensional driven systems. Phase separation occurs if the current out of a domain of size n either decays to zero with domain size or decays to a non-zero value J_∞ more slowly than $J_\infty(1+2/n)$. The phase separation takes the form of the emergence of one large domain occupying a finite fraction of the total system size. The importance of this criterion becomes obvious once we consider the inherent difficulties in determining whether condensation has occurred using numerical methods such as simulations of finite sized systems.

2.4 Monte Carlo simulations and the Next Reaction Method

Although exact analytical solutions are the preferred way of understanding a system such solutions may not always be accessible. When this is the case one of

the available options is to simulate the system on a computer instead. However computer simulations can be a powerful tool even before we start looking for analytical solutions. By using simulations to survey a system for interesting or *a priori* unexpected phenomena they may also serve the purpose of guiding the analysis of the system. Furthermore simulation results serve as a benchmark for determining the validity of approximations used in analytical solutions.

In this work I perform Monte Carlo (MC) type simulations wherein the configuration space of a model is explored in a stochastic manner. The stochasticity relies on a sequence of generated random numbers[15]. Thus if a simulation is repeated with a second sequence of random numbers it will yield a result which agrees with that of the first one only to within some statistical error. As such we find that the quality of the statistics a simulation can yield is governed by the limits to computer memory (size of accessible configuration space) and computational time (how well configuration space may be explored). Since MC type simulations are a tool used in each of the three main components of this work I have dedicated this section to a discussion on how these two resources were managed. In particular we will look at how the efficiency of a simulation may be improved by using the Next Reaction Method. For a more general look at MC simulations in statistical physics the reader is referred to e.g. [74].

All the performed simulations follow a generic layout which may be described by the algorithm:

1. **Initialise** the system. Sets up the system by implementing any initial conditions and initialising all variables.

2. **Choose** an event. This is the MC step where random numbers are generated and used to determine which event to perform. The timestep associated with the event is also calculated.

3. **Update.** The system time is increased by the calculated timestep and the chosen event is attempted.

4. **Iterate.** Return to step 2.

At the most basic level we consider the set of all possible events ε which change the state of the system. An event $E \in \varepsilon$ is chosen at random during the

[15]Since truly random numbers cannot be generated by a computer one instead has to use a pseudo-random number generator. Throughout this work I use the Mersenne Twister [82, 83].

the second step. A second uniformly distributed random number $x \in (0, 1]$ is drawn. If this is smaller than the probability $P_t(E, \Delta t)$ that the event E occurs during the time $t \to t + \Delta t$, then the update is performed. It is obvious that such an approach may be improved by eliminating the possibility of a chosen event being rejected. This is achieved by weighting the probability of an event being chosen by the probability that this update would occur during the timestep. This further suppresses any events which carry a zero probability of occurring.

Now consider the rates r_E at which each of the N possible events occur. Defining the cumulative rate function $R_i = \sum_{j=1}^{i} r_j$, and R_N as the total rate, we find that the selected event is the ith one for which $R_{i-1} < xR_N \leq R_i$. Since the considered events are Markovian the timestep is now continuously distributed and sampled from an exponential distribution with mean $1/R_N$. In practice this requires generating a second uniformly distributed random number, $x' \in (0, 1]$, which gives the timestep through $\Delta t = -\ln(x')/R_N$. However, since the time increments of any realisation are independent random variables we know from the central limit theorem (see e.g. [94]) that their sum will be Gaussian distributed about the sum of their means. As such the mean of each distribution can instead be used as the timestep, such that $\Delta t = R_N^{-1}$. This is how the simulations in the DACP chapter (chapter 3) are performed. I will refer to this as the Gillespie approach since it is effectively how the Gillespie algorithm [42][16] works.

After each iteration any events which were affected by the update must have their rates recalculated. As a result the Gillespie approach requires that the cumulative rate function be recalculated at every iteration. For a system where the majority of events remain unaffected by a given update this is an inefficient use of computational resources. To address this issue the Next Reaction Method was introduced [41]. In this method each event $E \in \varepsilon$ has an associated time $t(E)$ at which it occurs. The system is updated by advancing the time t to the time of the next event and then performing the associated event. After the update any events whose rates were affected by the update are assigned new event times. Since each update is a Poissonian process the time $t(E)$ assigned to an event is the current system time t plus a waiting time $t_w(E)$ which is sampled from an exponential distribution with mean $1/r_E$.

If the subset $m(\epsilon) \subset \varepsilon$ of events whose rates *may* be affected by the selected

[16] This is the same as BKL algorithm [18] (the '*N-fold way*').

event ϵ is small and known then an additional improvement may be possible. In this case assigning new event times to all events in $m(\epsilon)$ can prove computationally favourable to calculating which of the events $a(\epsilon) \subset m(\epsilon)$ actually *had* their rates affected. The simulations in chapters 4 and 5 rely on this implementation of the Next Reaction Method. This is an alternative to the technique described in [41] where the event times for $a(\epsilon)$ are transformed rather than re-assigned.

Thus the algorithm I use for the Next Reaction Method can be specified as follows.

1. Initialise the system:
   (a) enumerate all possible events E;
   (b) calculate the associated rates r_E for all E;
   (c) for each E generate an event time $t(E)$ from an exponential distribution with mean r_E^{-1};
   (d) store the event times in an ordered list H (more on this below).
2. Let ϵ be the event whose event time $t(\epsilon)$ is the smallest in H.
3. Let the system time t be $t(\epsilon)$.
4. Perform the event.
5. For each event $e \in m(\epsilon)$ which may have been affected by the performing ϵ (including ϵ itself):
   (a) update the rate r_e;
   (b) generate a new random number τ from an exponential distribution with mean r_e^{-1} and set $t(e) = t + \tau$;
   (c) replace the old value $t(e)$ in H with the new value.
6. Return to step 2.

This algorithm assumes that all possible events are known from the start. Disallowed events will therefore start by having an associated time, $t(E) = \infty$. If the possible events are not known at the start then the definition of $m(\epsilon)$ is extended to also include any new events.

A final remark regarding the Next Reaction Method is that when performing time averaging of some observable $A(\mathcal{C})$ which depends on the microscopic configuration $\mathcal{C}$ it is important to weight this average by the time $T(\mathcal{C})$ spent in each configuration. Thus

$$\langle A \rangle = \frac{\sum_{\mathcal{C}} A(\mathcal{C}) T(\mathcal{C})}{\sum_{\mathcal{C}} T(\mathcal{C})} \,. \tag{2.55}$$

The efforts described above ensure that the number of generated random numbers is reduced and that there are no rejected updates. In addition to this we can further improve the simulation by ensuring that the ordering of events by their associated times is done in an efficient manner.

We therefore store these in a binary tree structure, i.e. one where each node is less than or equal to that of both of its children, see Fig. 2.5. As such the smallest value is always found at the root of the tree. In my case I use a red-black tree, also known as a B-tree [13], which is the binary tree structure found to give the most consistent performance [53]. This ensures that basic operations such as finding, adding or removing a particular element scale as $\mathcal{O}(\ln N)$ in time. By comparison a simple sequential search would scale as $\mathcal{O}(N)$ [68].

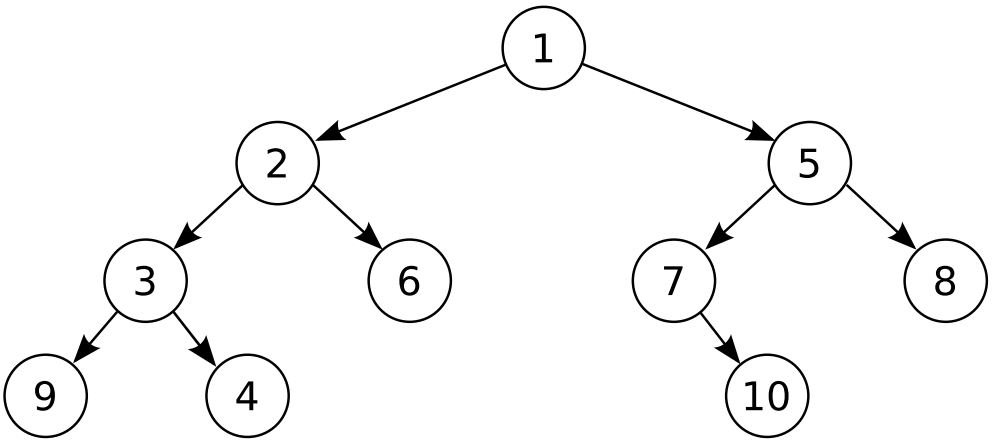

Figure 2.5: An illustration of a binary tree. Each node is greater than its children. Note that the children are not ordered.

Chapter 3

The Driven Asymmetric Contact Process

In chapter 2 we saw that the contact process exhibits a non-equilibrium phase transition from an inactive (absorbing) state to an active state. The continuous phase transition from an inactive to active phase falls into the Directed Percolation (DP) universality class. In the mean-field description the spreading of activity through the system is illustrated by the Fisher-KPP equation. This non-linear partial differential equation exhibits travelling wave solutions in which the active phase invades the inactive region at a well-defined velocity. In this chapter I will consider the driven asymmetric contact process, a variation of the contact process with the two features of an active boundary and asymmetric dynamics. The addition of an active boundary, which serves to drive the system, modifies the nature of the phase transition. In particular the DP transition now has a discontinuous aspect in the sense that the velocity of the wavefront which carries the activity from the boundary jumps discontinuously at the critical point. To understand this discontinuity I consider a mean-field description of the system in the form of a Fisher-KPP equation with an advective term.

3.1 Motivation

In section 2.1.3 the non-equilibrium contact process was introduced and shown to undergo a phase transition from an absorbing state, where the system ends up in an inactive configuration, to an active, fluctuating state. This phase transition

is continuous and known to fall into the Directed Percolation (DP) universality class (section 2.1.1) which is thought to pertain for any such microscopic model exhibiting an absorbing state phase transition, in the absence of any additional symmetries or conservation laws.

The nature of the transition may be modified by the introduction of an active boundary into the system that ensures that the activity in the system never dies out [22, 39, 15, 54]. These studies have mainly focused on surface critical behaviour and the emergence of new surface critical exponents. In the counterpart to the inactive phase the activity is confined to the boundary region whereas in the counterpart to the active phase the activity spreads from the boundary through the system. The spreading of activity through the system from the boundary is conveniently illustrated in the mean-field description of the DP universality class which has the same form as the Fisher-KPP equation (section 2.2.1). This non-linear partial differential equation exhibits travelling wave solutions in which the active phase invades inactive regions with a well-defined velocity for the domain wall that separates the two regions.

A variation of the contact process, the driven asymmetric contact process, with the two features of an active boundary and advection away from the boundary was introduced in [15] where the steady-state properties were also determined. The asymmetric contact process had been previously studied in the absence of boundaries and found to yield a phase transition in the DP universality class, as expected [98, 105, 96]. The addition of an active boundary, which serves to drive the system, modifies the nature of the transition as described above [15]. In the work presented here we discover that the DP transition now has a discontinuous aspect in the sense that the velocity of the wavefront which carries the activity from the boundary jumps discontinuously at the critical point. Thus, intriguingly, the continuous DP transition is accompanied by a velocity discontinuity in the presence of an active boundary and advection.

To understand the observed transition, I consider a phenomenological mean-field description of the system in the form of a Fisher-KPP equation which includes the effects of asymmetry in the form of an advective term. I show that the solution can be thought of as a Fisher wave moving within an envelope given by the stationary density profile. Thus, in the subcritical regime the system exhibits attenuated waves with non-zero velocity but whose amplitude decays to

zero away from the boundary. In the supercritical regime, on the other hand, the stationary profile has a non-zero limit far from the boundary, thus the Fisher wave propagates into the bulk with a constant amplitude and non-zero velocity. This is the mechanism for the observed discontinuity of the velocity.

3.1.1 Fisher-KPP with an advective term

If there is a directional force on a Fisher-KPP system, such as we encounter here, an advective term proportional to the gradient needs to be added to the Fisher-KPP equation (2.16). Thus giving

$$\frac{\partial \rho}{\partial t} = D\frac{\partial^2 \rho}{\partial x^2} + \alpha\rho(1-\rho) + v\frac{\partial \rho}{\partial x} \,, \tag{3.1}$$

where v is the velocity of the advective term. It can easily be shown[1] that through a change of coordinates to a reference frame co-moving with the advective term, the normal Fisher-KPP equation can be recovered. Therefore the only effect of the advective term is to shift the linear spreading velocity from v^* to $v^* + v$.

There has been recent interest in the addition of an advection term to the Fisher-KPP equation in the presence of a boundary since the Galilean transformation no longer serves to remove the advection term. When the advection is directed *towards* the boundary there is a competition between the advective velocity and the Fisher wave velocity, leading to a phase transition [10, 29, 102] from a phase with activity localised near the boundary to one where the Fisher wave invades the whole system. The addition of noise into this system leads to a more complicated scenario where, in the case of a reflecting boundary studied in [11], the low activity phase could either be localised near the boundary or be the absorbing state. However, the discontinuous transition observed in that work where the bulk density jumps at the transition, is distinct from that studied in this chapter.

3.2 Microscopic model

The driven asymmetric contact process (hereafter, DACP) is a stochastic model defined on a one-dimensional lattice. A microscopic configuration is specified by

[1] E.g. p.55 of [109].

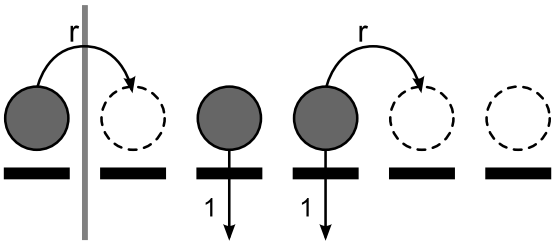

Figure 3.1: The Driven Asymmetric Contact Process. In this model, the first site is kept active. Active sites can activate inactive sites to the right of them at rate r or become inactive with rate 1.

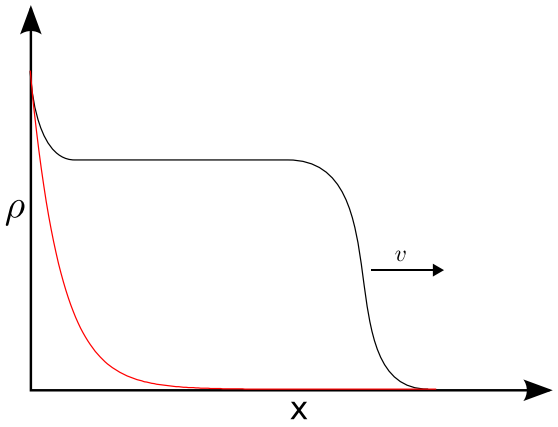

Figure 3.2: A sketch of the density profile of the two states. In the subcritical state (red) the density decays exponentially whilst in the supercritical it propagates at a constant bulk density.

the set of occupation numbers $\{\tau_i(t)\}$ where $\tau_i(t) = 0\,(1)$ indicates that site i is inactive (active) at time t. The leftmost site of the system is kept permanently active, $\tau_0(t) = 1\ \forall t$, making the process driven. Active sites can activate inactive sites directly to the right of them at rate r or become inactive with rate 1. See Fig. 3.1 for an illustration.

The driving from the left boundary eliminates the absorbing state associated with the basic contact process. However as the rate r goes through a critical value r_c there is still a continuous phase transition from a phase where the active sites can only spread a finite distance from the left boundary to a phase where they can spread to infinity. See Fig. 3.2 for an illustration of the density profile in the two states.

An interesting and attractive feature of the model is that the total asymmetry of the activation dynamics means that the state of site N_1 is independent from that of N_2 for $N_2 > N_1$. This implies that any calculation or simulation performed on a finite system of N sites gives the *exact* behaviour for the first N sites of an infinite system. In other words, the introduction of a right boundary does not introduce any finite-size effects.

To put the DACP in its context I will here summarise previous work on asymmetric contact processes. Three mathematical papers [98, 105, 96] have looked at how introducing asymmetry into the contact process (without a boundary drive) leads to the emergence of a second order parameter, the probability that the origin is active as $t \to \infty$, in addition to the probability that the process remains active indefinitely. At total symmetry the two order parameters coincide and at total asymmetry the second disappears. An approximate analytical and numerical study of the totally asymmetric contact process (without a boundary drive) [107] found a continuous transition at the critical rate $r_c = 3.306(4)$ with the critical exponent $\beta = 0.2760(1)$ which is in agreement with the value for the DP order parameter exponent in one spatial dimension. In addition a two-dimensional generalisation of the DACP was constructed [15] and used to study wetting and interface phenomena [16]. I mention this last one only for completeness since it is the only other work directly related to the DACP.

3.3 Numerical evidence for a discontinuous velocity transition

We begin the study of the DACP by presenting numerical data that suggests the velocity of the wave emanating from the left boundary is discontinuous at the phase transition point.

3.3.1 Simulation details

I performed direct Monte Carlo simulations (section 2.4) of the microscopic DACP dynamics specified in section 3.2 above. Each run is initialised with the lattice unoccupied, apart from the 0th site which is kept permanently active. During

the simulation a list of active sites is maintained. In each elementary update, one of the n active sites is chosen from this list at random. With probability $\frac{r}{r+1}$, its right neighbour is activated (if already active then nothing happens); otherwise the chosen active site becomes inactive.

As the aim is to measure a velocity, it is important to keep track of the length of time associated with each update. Since an update is attempted on any of the n active sites the total attempt rate is $\lambda = n(1+r)$. The size of the associated time increment was approximated by the mean, $1/\lambda$, of the exponential distribution. The approximation of using the mean, rather than sampling the distribution, is computationally favourable and it was verified that it made no difference to the results. Thus the time taken for each update is $\Delta t = \frac{1}{n(1+r)}$, where n is the total number of active sites *before* the update takes place.

The front velocity of a single run was defined as the position of the rightmost active site at the end of the run, divided by the time taken for the run to end. This definition was chosen since it is unambiguous in the microscopic model. The simulations were run until a pre-specified amount of time had elapsed: the lattice expanded as needed to accommodate all active sites. To reduce the noise in the data the simulation was repeated for 500 runs for each value of r and the quantities of interested averaged over this ensemble of runs.

3.3.2 Results

The first interesting result pertains to the asymptotic front velocity. The simulation was run for several different simulation times as shown in Fig. 3.3. The definition of the front velocity implicitly assumes that an asymptotically constant velocity is reached on a timescale short compared to that at which the simulation ends. We anticipate that this may not be the case for values of r near the critical value r_c, since relaxation times diverge here. Therefore measurements of the velocity near r_c are subject to finite-time corrections. As can be seen from Fig. 3.3, increased run time shows a sharpening of the velocity as a function of r near r_c, suggestive of a discontinuous transition in the infinite-time limit.

The density profile in the two different phases was also studied. The position and shape of the front can be investigated by looking at the density profile for a single activation rate at different times. Choosing two values of r close to, and on either side of, the critical rate we observe two very different scenarios. For the

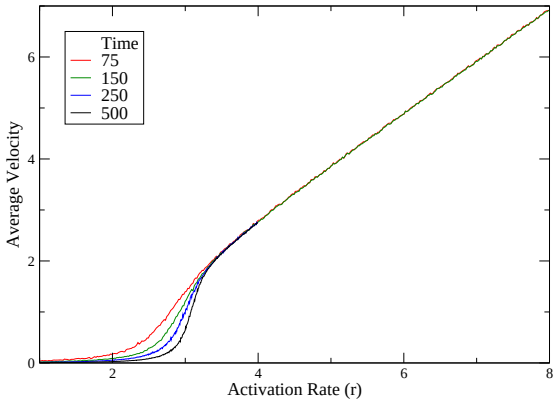

Figure 3.3: A plot of the front velocity versus activation rate for different run times. The two shorter runs spanned activation rates in the interval $r \in [1, 8]$ and the longer two $r \in [1, 4]$, in both cases the intervals were subdivided into 500 equally spaced values of r for which the simulation was run. Note that as the simulation time is increased a discontinuity appears to develop.

supercritical case (Fig. 3.4a) there is a wave of constant bulk density invading the empty lattice. The front simply propagates away from the boundary at a constant velocity.

For the subcritical case (Fig. 3.4b) we observe an attenuated wave: the front propagates away from the boundary whilst at the same time decaying away. However the decaying density seems to follow an envelope of sorts. As a guide to the eye this envelope has been added to the graph. We will return to the idea of this envelope again in section 3.6.

It is perhaps surprising at a first glance that the *continuous* DP transition should be accompanied by a *discontinuity* in the front velocity. In the remainder of this chapter, I elucidate the mechanism behind this discontinuity.

3.4 A real discontinuity?

Although Fig. 3.3 suggests that there is a discontinuity in the front velocity we observe that finite-time effects mean the velocity will always appear to be continuous for any finite simulation. In this section I first consider an alternative simulation in which the discontinuity is more prominent. Secondly I consider an alternative source of the discontinuity and show that this, by itself, does not

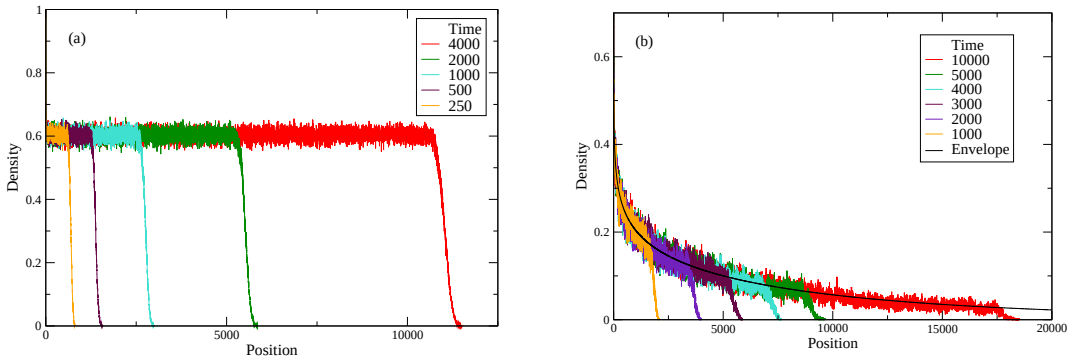

Figure 3.4: (a) Density versus position in the supercritical regime ($r = 4.0$) at different times. A wave of constant bulk density invades the empty lattice as time progresses. (b) Corresponding data for the subcritical regime ($r = 3.275$). The wave is attenuated by an envelope fitted empirically by the solid line.

explain the discontinuity. Finally I introduce test models to understand what the requirements are for a discontinuous front velocity.

3.4.1 Using a different time measure

From the definition of the timestep in section 3.3.1 we find that time in the simulation runs slower the more sites are active, i.e. at larger activation rates. A slower time here means that there are more updates performed per unit time. Thus for a simulation running for some fixed time (over a range of rates) a substantial amount of the actual runtime will be spent in the supercritical regime. However from Fig. 3.3 we find that the velocity determination in the supercritical regime is largely unaffected by the increase in simulation time.

Since the supercritical regime is costly runtime-wise this suggests running the simulation for a fixed number of updates, for each rate, instead. This would be a more efficient use of the runtime since more computational power would then be spent on the subcritical region where it will improve the velocity determination. The result from a simulation with a *fixed number of updates* would therefore give an effective image of what the velocity profile would look like had the original simulation been run for a significantly longer time.

The resulting plot, Fig. 3.5, shows the discontinuity more clearly. However, it is important to note that such a plot is only useful for visualisation purposes. Any data analysis must use data from the fixed time simulation rather than the

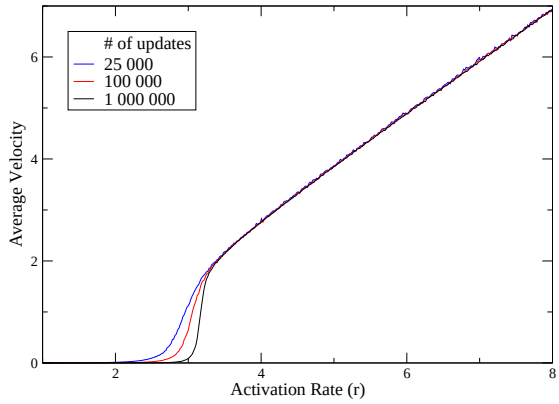

Figure 3.5: A plot of the velocity versus activation rate for a fixed number of updates at each rate.

fixed updates simulation. For completeness we note that the two measurements of time, updates (u) and simulation time (t), are related through

$$t = \frac{1}{1+r} \sum_{j=0}^{u-1} \frac{1}{n_j} \tag{3.2}$$

where $n_j = \sum_{i=0}^{\infty} \tau_i(j)$ is the number of active sites after j updates.

3.4.2 Front broadening

In the simulation the front velocity is defined as being the velocity of the rightmost particle rather then that of the centre of the front. There is therefore a possibility that some sort of front broadening could cause the discontinuity in the velocity of the rightmost particle. Were this the case then no such discontinuity would be present in the velocity of the centre of the front.

The issue is resolved by studying under which conditions such a discontinuity might emerge from a broadening front. The front may be described by

$$\rho(x,t) = f\left(\frac{x - vt}{\sigma}\right) , \tag{3.3}$$

where v is the velocity of the centre of the front and $\sigma = \sigma(t) \sim t^{\gamma}$ is the width of the front. For the front width not to become comparable to the system size $\gamma < 1$. Following the rightmost particle is equivalent to following the point, x^*,

at which the area under the remainder of the tail is equal to 1. i.e.

$$\begin{aligned} \int_{x^*}^{\infty} f\left(\frac{x-vt}{\sigma}\right)\mathrm{d}x = 1 \quad &\Rightarrow \\ \int_{\frac{x^*-vt}{\sigma}}^{\infty} f(u)\mathrm{d}u = \frac{1}{\sigma}\ . \end{aligned} \tag{3.4}$$

The normal expectation is for the tail of the front to exhibit an exponential density profile, $f(u) \sim e^{-ku}$. Inserting this into (3.4) and rearranging gives

$$\frac{x^*}{t} = v + \frac{\sigma}{kt}\ln\left(\frac{\sigma}{k}\right) \sim v + \frac{\gamma}{kt^{1-\gamma}}\ln\left(\frac{t}{k^{1/\gamma}}\right) \xrightarrow[t\to\infty]{} v\ , \tag{3.5}$$

i.e. the velocity of the rightmost particle, x^*/t, tends to the velocity of the centre of the front as time tends to infinity.

The only point where a differently shaped tail might be expected is at criticality. Here properties are generically characterised by power laws thus the tail may be described by $f(u) \sim u^{-\nu}$. Using this expression in (3.4) and rearranging gives

$$x^* = \begin{cases} vt + \sigma^{\frac{\nu}{\nu-1}}(\nu-1)^{\frac{-1}{\nu-1}} & \text{for } \nu > 1\ , \\ \infty & \text{for } 0 < \nu \leq 1\ . \end{cases} \tag{3.6}$$

Without knowing more about the exponents one cannot say whether this will result in a front tail velocity which is larger then that of the centre. However, if this happens it is due to the behaviour of the system at criticality, i.e. the discontinuity is still a result of the phase transition. Thus front broadening might be the mechanism through which the discontinuity arises but the discontinuity would still very much be a real feature of the system.

With these issues satisfactorily resolved and the discontinuity shown to be a real feature of the system we move on to explaining its origins.

3.4.3 Investigating other models

To better understand the origins of the discontinuous velocity in the DACP several other models were developed and probed for similar results. Care was taken to design the simulation in the same way as for the DACP model so as to eliminate

the possibility that the velocity discontinuity was an effect of the simulation design. The strategy was to build an increasingly complex model from a simple one to see at which point the discontinuous behaviour emerged.

Thus the basis for the first such model was one random walker on a 1D lattice with a reflective boundary at the origin. The walker (the rightmost walker in later models) plays the part of the front in the DACP. As in the DACP system we observe a phase transition from a phase where the walker can only move a finite distance away from the boundary to a phase where it can move to infinity. The transition is characterized by the average velocity of the (rightmost) walker going from zero, when restricted to being close to the wall, to a finite value as it moves off to infinity. By adjusting the left-right bias of the walker the different phases of the system could be probed. As expected the phase transition for a one walker system is continuous in the velocity (RW1 in Fig. 3.6a).

In the second model additional random walkers were introduced by allowing the birth and death of walkers *to the left* of the original (and therefore rightmost) walker. This ensures that, on average, the density of walkers in the active region (i.e. to the left of the rightmost walker) remains constant. Varying the ratio of the birth to death rates thus allows the system to be sampled at different densities. To prevent walkers from passing each other we apply an exclusion condition whereby only one walker is allowed per site at any given time. Thus the net effect of allowing the birth of new walkers is to apply a constant pressure on the rightmost particle driving it further right. For this model too the velocity of the rightmost particle was continuous across the phase transition (RW2).

To make the models closer to that of the DACP the rightmost walker is now also allowed to die. This introduces an absorbing state, which is not present in the DACP. To prevent this two separate mechanisms were tried. In the first approach death is only allowed until one walker remains (RW3). In the subtly different second approach (RW4) the birth of a walker is always allowed at the first site (directly to the right of the boundary). Both of these mechanisms resulted in a continuous velocity across the transition though. A sample of the velocity profiles for the random walker models can be seen in Fig. 3.6a.

Since none of the random walker models displayed the sought for discontinuity a different approach was tried for the last model. Here we start at the DACP and simplify it by making the hop rates symmetric. In this, contradictorily named,

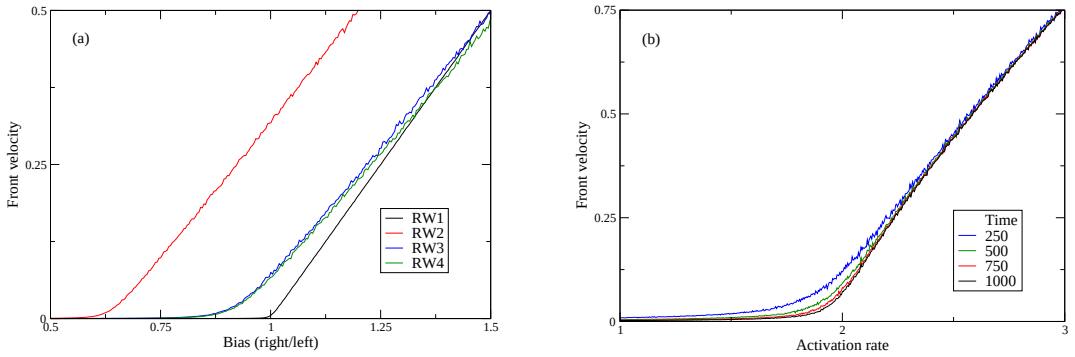

Figure 3.6: (a) Front velocity versus bias (to the right) for the four different random walker models. For models 2–4 the birth and death rates are both 0.1. (b) Front velocity versus activation rate for the symmetric DACP at different run times.

symmetric DACP model we still observe a phase transition but once again the velocity remained continuous, Fig. 3.6b. Thus the results from all of these models indicate that the requirement for a velocity discontinuity is quite subtle.

3.5 Directed Percolation scaling picture

Despite the absence of an absorbing state in the DACP, I show in this section that the behaviour of the DACP described in the previous section can in fact be interpreted within the universal scaling picture associated with the Directed Percolation phase transition.

3.5.1 Steady-state density profile

It should be noted that the work in this subsection was largely done by Blythe in [15]. It has been summarised here so as to assist the reader by collecting the relevant material in one place.

Now consider the steady-state density profile of the system $\rho_i = \lim_{t\to\infty}\langle\tau_i\rangle$. A suitable order parameter for the system is the steady-state density as $i \to \infty$, which we denote by $\overline{\rho}$. In the supercritical phase, close to criticality, the order parameter is expected to scale as $\overline{\rho} \sim \Delta^{\beta}$, where $\Delta = |r - r_c|$ is the distance from criticality and β is the order parameter exponent which is expected to be equal to the value for DP in one spatial dimension. We can also define a characteristic length scale ξ as the steady-state density decay length in the subcritical phase

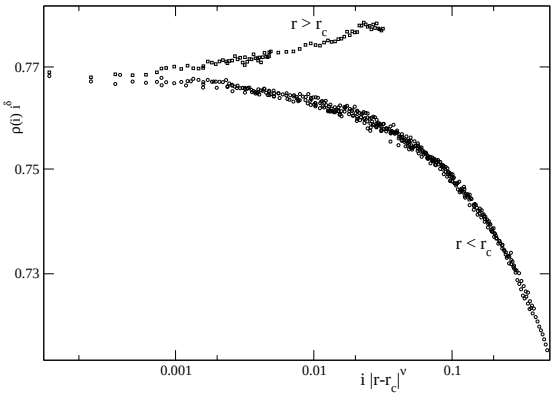

Figure 3.7: Collapse of the steady-state density profile ρ_i (this image uses the convention $\rho(i)$ instead) for a range of activation rates r onto two master curves, one for the supercritical regime (upper curve) and one for the subcritical regime (lower curve). The collapse was obtained by varying the free parameters r_c, δ and ν. Figure reproduced from [15].

where $\rho_i \sim \mathrm{e}^{-i/\xi}$. Then, since the length scale diverges at criticality we expect it to scale as $\xi \sim \Delta^{-\nu}$ near criticality where ν is a correlation length exponent. At criticality we expect the profile to decay as a power law with exponent δ.

Near criticality we further expect the scaling form $\rho_i \simeq i^{-\delta} g(i/\xi)$ with $g(u)$ a scaling function obeying $\lim_{\xi\to\infty} g(i/\xi) = g(0) =$ constant such that at criticality $\rho_i \sim i^{-\delta}$. However since the steady-state density approaches a non-zero constant as $x \to \infty$ in the supercritical phase it follows that $\lim_{u\to\infty} g(u) \sim u^{\delta}$. Thus $\lim_{i\to\infty} \rho_i \sim i^{-\delta} u^{\delta} = \xi^{-\delta} \sim \Delta^{\delta\nu}$. But we also know that $\lim_{i\to\infty} \rho_i = \overline{\rho} \sim \Delta^{\beta}$. Thus it follows that $\delta = \frac{\beta}{\nu}$.

In [15], the critical point r_c and exponents δ and ν were obtained by plotting $\rho_i i^{\delta}$ against $u = i/\xi = i\,|r - r_c|^{\nu}$ for different values of r, and varying r_c, δ and ν until the best data collapse (as judged by eye) was obtained. The resulting collapse, obtained for $r_c = 3.3055(5)$, $\delta = 0.1640(5)$ and $\nu = 1.7(2)$, is reproduced from [15] in Fig. 3.7.

These measurements are compared with the established values of the DP exponents in table 3.1. Good agreement is observed with the DP values that apply in one spatial dimension (1D) as long as we identify the exponent ν with the DP *temporal* correlation exponent $\nu_{\parallel}$, as opposed to the distinct, and independent, spatial exponent $\nu_{\perp}$: this point will be discussed in more detail later. For future reference, the exponents obtained within a mean-field approximation have also

been included in table 3.1. For an in-depth study of DP exponents and scaling the reader is referred to [55]. Here the focus is more on the dynamic behaviour of the DACP and the behaviour of the active front as it moves out from the left boundary.

	DP (MF) [55]	DP (1D) [61]	DACP [15]
δ	1	0.159464(6)	0.1640(5)
$\nu_\parallel$	1	1.733847(6)	1.7(2)
$\nu_\perp$	1/2	1.096854(4)	

Table 3.1: Critical exponents for Directed Percolation (DP) in a mean-field approximation (MF) and one spatial dimension (1D), and for the Driven Asymmetric Contact Process (DACP) of the present work.

Solution of spatially discretized mean-field equation

First consider an exact equation for the rate of change of density at site i in the DACP. This reads

$$\frac{\mathrm{d}}{\mathrm{d}t}\langle\tau_i(t)\rangle = r\langle\tau_{i-1}(t)\left[1-\tau_i(t)\right]\rangle - \langle\tau_i(t)\rangle \ , \tag{3.7}$$

where the first term comes from site $i-1$ activating site i at rate r if the former is active and the latter inactive, and the second term from the decay of site i at unit rate when it is active. The mean-field approximation is to write $\langle\tau_i(t)\tau_j(t)\rangle = \rho_i(t)\rho_j(t)$, where $\rho_i(t) = \langle\tau_i\rangle$. The mean-field equation governing the density in the DACP process is then

$$\begin{aligned} &\dot{\rho}_i = r\rho_{i-1}(1-\rho_i) - \rho_i \quad \forall i \geq 1 \\ &\rho_0 = 1 \quad \forall t \end{aligned} \tag{3.8}$$

The steady-state solution ($\dot{\rho}_i = 0$) is

$$\rho_i = \frac{(1-r)r^i}{1-r^{i+1}} \tag{3.9}$$

which yields the large i behaviour

$$\begin{aligned} \rho_i &\simeq (1-r)r^i && \text{for} \quad r<1\ , \\ \rho_i &= \frac{1}{i+1} && \text{for} \quad r=1\ , \\ \rho_i &\simeq \frac{(r-1)}{r}\left(1+r^{-(i+1)}\right) && \text{for} \quad r>1\ . \end{aligned} \tag{3.10}$$

Thus this mean-field theory is consistent with the profiles decaying with a decay length which diverges as $1/|\ln r| \sim \Delta^{-1}$ and the order parameter emerging as $\overline{\rho} \sim \Delta$ where $\Delta = r - r_c$ with $r_c = 1$. Also at criticality we have a power law decay of the profile with exponent $\delta = 1$. All these exponents are consistent with the mean-field DP exponents given in table 3.1.

3.5.2 Advection dynamics: the shearing of DACP into DP

The easiest way to understand the effect of asymmetry (or advection) in the contact process is to directly compare a space-time plot of the DACP dynamics with its contact process counterpart and its description in terms of DP scaling exponents—see Fig. 3.8. From these plots we identify two characteristic angles. In the DACP, Fig. 3.8a, the activity emanates from the wall with an axis that is an angle θ to the vertical. This axis corresponds to the time direction in the basic contact process, Fig. 3.8b. The leading edge of the activity emerges at an angle ϕ to the DP time axis. We thus picture the DACP as a spatial shearing of DP by the shear element $\tan\theta$. One consequence of this shearing is that the spatial correlation length measured in the steady-state density profile of the DACP is a linear combination of the temporal and spatial correlations lengths in DP, such that $\xi'_\perp = \xi_\perp + \xi_\parallel \tan\theta$ and $\xi'_\parallel = \xi_\parallel$, with primed variables pertaining to the DACP. Hence, we expect the DACP correlation length to diverge with the faster-growing DP correlation length as $r \to r_c$, and therefore that ν should be identified with the larger of the DP exponents (i.e., $\nu_\parallel$, as above).

We now turn to the dynamics. Above the critical point in DP, an activity wave travels at a velocity $v_{\rm DP} = \tan\phi$. If, near criticality, there is a single characteristic length and time scale, this velocity must be given by their ratio. That is

$$v_{\rm DP} = \tan\phi = \frac{\xi_\perp}{\xi_\parallel} \sim \Delta^\chi \quad \text{with} \quad \chi = \nu_\parallel - \nu_\perp\ . \tag{3.11}$$

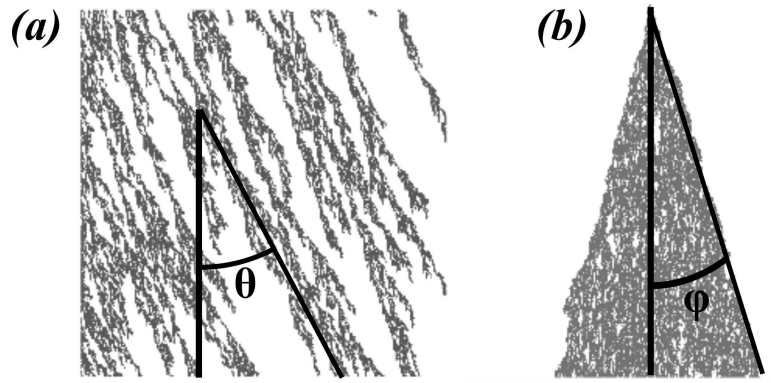

Figure 3.8: Space time plots of (a) the DACP and (b) DP. In DP, a cone of activity spreads at an angle ϕ to the time (vertical) axis; to obtain the DACP, this cone is sheared by a further angle θ due to the advection. Note that the activation rates have been chosen to allow easy identification of the two angles in these figures: the distance from the critical point is different in the two cases, and hence there is no significance of the density of the DP clusters being greater than that for the DACP.

Since $\nu_\parallel > \nu_\perp$, this velocity vanishes as $r \to r_c$ from above. Below criticality, activity does not spread out indefinitely, and so the wave velocity is zero when $r < r_c$. Thus, the wave velocity is continuous across the transition in the absence of advection.

We obtain the supercritical wave velocity for the DACP, $v_{\rm sup}$, by applying the shear $\tan\theta$. That is,

$$v_{\rm sup} = \frac{\xi'_\perp}{\xi'_\parallel} = \frac{\sin\phi + \tan\theta\cos\phi}{\cos\phi} = \tan\phi + \tan\theta = v_{\rm DP} + s \sim s + A\Delta^\chi \qquad (3.12)$$

where we have introduced the *advection* $s = \tan\theta$. Note that there may be subleading corrections coming from corrections to scaling in the relation (3.11). The actual value of s is a non-trivial emergent property of the stochastic DACP dynamics. However, a key point is that it can take a non-zero value in the subcritical regime which yields the *intrinsic* velocity $v_{\rm sub}$: activity still propagates at rate $v_{\rm sub} = s$ from the active boundary, despite the fact that it dies out after some finite time. Thus, the *apparent* (i.e. the observed) wave velocity, measured far from the origin, may jump discontinuously from zero to some non-zero value $v_c = s(r_c)$ at the critical point. This is in contrast to the DP wave velocity which goes to zero at criticality, as shown above. The leading-order behaviour

of the supercritical wave velocity in the DACP is then $v_{\rm sup} \sim v_c + A\Delta^{\chi}$ where $\chi = \nu_{\parallel} - \nu_{\perp}$. It should be remarked that this expression provides a means to measure the smaller correlation length exponent, $\nu_{\perp}$, which cannot be accessed from the steady-state density profile alone.

3.6 Mean-field theory

Having proposed a mechanism for the discontinuous velocity transition observed in section 3.3.2, I now demonstrate explicitly that it is at work within the mean-field formulation of the DACP dynamics.

We know that for a DP model, such as the contact process, the continuous-space mean-field description is given by a Fisher-KPP equation (section 2.2.1). Beginning with the general form of the Fisher-KPP equation supplemented by an advection term to take into account the boundary drive present in the DACP:

$$\frac{\partial \rho}{\partial t} = \alpha\rho - \beta\rho^2 - r'\frac{\partial \rho}{\partial x} + D\frac{\partial^2 \rho}{\partial x^2} \; . \tag{3.13}$$

At this stage α, β, D and r' are phenomenological parameters. Note that this is a more general form of equation (3.1) with a steady states at $\rho = \alpha/\beta$ rather than 1. We will match the phenomenological parameters of (3.13) with the parameters of the microscopic model in section 3.7.1 below. Meanwhile we note that r' and D are expected to be smooth functions of the microscopic advection coefficient r and that $\alpha \propto r - r_c$.

We first establish the two distinct stationary regimes which are determined by the sign of α. Setting $\frac{\partial \rho}{\partial t} = 0$ in (3.13) we find that the stationary density $\rho^*(x)$ is given by

$$0 = \alpha\rho^* - \beta\rho^{*2} - r'\frac{\partial \rho^*}{\partial x} + D\frac{\partial^2 \rho^*}{\partial x^2} \; . \tag{3.14}$$

The solution takes the following forms for large x.

For $\alpha < 0$ ***(subcritical case)*** : a density profile which decays exponentially to zero and has the form for large x, $\rho^*_{\rm sub}(x) \simeq Ae^{-\lambda x}$

For $\alpha > 0$ ***(supercritical case)*** : a density profile which decays exponentially to a non-zero value and has the form for large x, $\rho^*_{\rm sup}(x) \simeq \overline{\rho} + Be^{-\lambda x}$ with $\overline{\rho} = \frac{\alpha}{\beta}$.

In both cases the decay constant may be written as

$$\lambda = \frac{-r' + (r'^2 + 4|\alpha|D)^{1/2}}{2D} \ . \tag{3.15}$$

For small $|\alpha|$, $\lambda = O(|\alpha|)$. Thus the characteristic lengthscale ξ diverges as $|\alpha|^{-1}$ at criticality. Following the arguments of section 3.5, ξ is expected to diverge with the DP exponent $\nu_\parallel$. From table 3.1, we indeed see that $\nu_\parallel = 1$ in the mean-field.

Based on the envelope observed in the simulation of the stochastic system (see section 3.3.2) we assume that the full time-dependent density can be described by $\rho(x,t) = \rho^*(x)f(x,t)$ where $\rho^*(x)$ is the stationary solution to (3.14). Equation (3.13) then becomes

$$\rho^* \dot{f} = \alpha\rho^* f - \beta {\rho^*}^2 f^2 - r'(\rho^{*\prime} f + \rho^* f') + D(\rho^{*\prime\prime} f + 2\rho^{*\prime} f' + \rho^* f'') \ . \tag{3.16}$$

Dividing through by ρ^* and using the definition of ρ^*, (3.14), to eliminate α we obtain a modified Fisher-KPP equation for the wave $f(x,t)$ that sits inside the envelope:

$$\frac{\partial f}{\partial t} = \beta\rho^* f(1-f) - s\frac{\partial f}{\partial x} + D\frac{\partial^2 f}{\partial x^2} \ . \tag{3.17}$$

In this equation, the advective velocity of the modified wave, s, is given by

$$s = r' - \frac{2D\rho^{*\prime}}{\rho^*} \ . \tag{3.18}$$

Note that this advective velocity, s, is generally increased over the bare quantity r' as a consequence of the envelope. The coefficient, $\beta\rho^*(x)$ of the non linear growth term $f(1-f)$ is generally x dependent, but in the supercritical phase it decreases to a constant value for large x thus recovering the Fisher-KPP equation far from the boundary. On the other hand, in the subcritical regime the non-linear term decreases to zero far from the boundary.

First we consider the supercritical phase. Far from the boundary (3.17) becomes, using $\rho^* \to \alpha/\beta$ and $s \to r'$

$$\frac{\partial f}{\partial t} = \alpha f(1-f) - r'\frac{\partial f}{\partial x} + D\frac{\partial^2 f}{\partial x^2} \tag{3.19}$$

which is the usual Fisher wave equation with advective coefficient r'. Following

the usual approach (see section 2.2.1), one assumes a travelling wave form $f(x,t) = f(x - vt) = f(z)$ and linearises for large z where f is small. The solution is of the form $f = e^{-\mu z}$ with

$$\mu = \frac{(v - r') \pm \sqrt{(v - r')^2 - 4D\alpha}}{2D} \,. \tag{3.20}$$

Since $\mu \in \mathbb{R}_+$ we require $(v - r')^2 \geq 4D\alpha \Rightarrow v \geq r' + \sqrt{4D\alpha} = v_{\min}$. We now assume (as for the normal Fisher wave starting from an initial sharp front) that $v = v_{\min}$. Thus

$$v_{\sup} = r' + \sqrt{4D\alpha} \,. \tag{3.21}$$

Of course (3.21) could simply be obtained by adding the advective velocity r' to the usual Fisher wave velocity in the absence of advection, $(4\alpha D)^{1/2}$.

In the subcritical phase, the modified wave described by (3.17) has a velocity given by a distinct expression. Here, for large x, (3.17) becomes

$$\dot{f} = A\beta e^{-\lambda x} f(1 - f) - sf' + Df'' \tag{3.22}$$

where

$$s = r' + 2D\lambda = (r'^2 + 4\,|\alpha|\,D)^{1/2} \,. \tag{3.23}$$

Note that the advective velocity of the attenuated wave is increased over the value r'.

The spatial dependence of the coefficient of the non-linear term makes the analysis of equation (3.22) non-trivial. Here we content ourselves with a heuristic picture. Initially the presence of the non-linear term will mean that a non-linear travelling wave emanates from the boundary. However as the front moves away from the boundary the non-linear term becomes less important and we expect the front to broaden and the velocity to decrease. Finally as the front of the wave moves further away and $x \gg 1/\lambda$ the equation for f reduces to a diffusion equation with advection

$$\dot{f} = -sf' + Df'' \,. \tag{3.24}$$

The wavefront thus broadens diffusively over time. Therefore, at late times, the modified density profile f will be approximately that given by a diffusion equation.

This diffusive front moves with velocity

$$v_{\rm sub} = s = (r'^2 + 4|\alpha|D)^{1/2} \ , \tag{3.25}$$

and the profile itself takes the form

$$f(x,t) \simeq \frac{1}{2}\,\mathrm{erfc}\left[\frac{x-st}{2\sqrt{Dt}}\right] \ . \tag{3.26}$$

Thus the width of the front is ultimately $\sqrt{Dt}$. Details are provided in the appendix A.1.

To summarise, the analysis of the phenomenological Fisher-KPP equation (3.13) shows that there are two possible regimes, according to the sign of α. When α is negative, the density decays to zero as it moves away from the origin; when positive, it propagates away from the origin with a constant bulk density at a constant velocity. The dynamics can be couched in terms of a modified wave, $f(x-vt)$, travelling within the envelope of the steady-state density profile, $\rho^*(x)$. This wave is governed by the modified Fisher-KPP equation, (3.17), and has a velocity in these two states of $v_{\rm sub} = \sqrt{r'^2 - 4D\alpha}$ and $v_{\rm sup} = r' + \sqrt{4D\alpha}$. Note that v is continuous at the transition $\alpha = 0$ although its derivative is not.

In the subcritical regime, this velocity coincides with the advective velocity s introduced in section 3.5 in terms of the angle of shear from DP to the DACP. As noted previously, one effect of the envelope is to force the apparent velocity (i.e., that observed in simulations) to decay to zero: activity can probe only a finite distance from the origin as time $t \to \infty$. Above the critical point, the observed velocity is $v_{\rm sup}$ and so, across the transition, this observed velocity exhibits a discontinuity. We note from the form of $v_{\rm sup}$, the velocity grows from its critical value as $v - v_c \sim \alpha^\chi$ where $\chi = 1/2$. This value of χ agrees with the prediction $\chi = \nu_\parallel - \nu_\perp$ from the mean-field theory for DP (see table 3.1).

3.7 Modified travelling wave in the stochastic DACP

We now revisit the simulations of the DACP in the light of what we have learnt from the mean-field theory. We first express the phenomenological

parameters appearing in the Fisher-KPP equation, (3.13), in terms of the stochastic activation rate r. We then examine more closely the numerical evidence for the picture of a modified wave travelling within the stationary density profile, and in particular, the prediction for the growth of the wave velocity just above criticality, i.e., $v - v_c \sim \alpha^\chi$ where $\chi = \nu_\parallel - \nu_\perp$ given by the appropriate DP exponents.

3.7.1 Identification of the mean-field phenomenological parameters

We first revisit the mean-field theory of section 3.6 and compare this to the mean-field DACP dynamics found in section 3.5.1. From (3.8) we see that the mean-field equation is

$$\begin{aligned} \dot{\rho}_i &= r\rho_{i-1}(1-\rho_i) - \rho_i \quad \forall i \geq 1 \\ \rho_0 &= 1 \quad \forall t \end{aligned} \tag{3.27}$$

One may make a heuristic identification of the phenomenological parameters in (3.13) by moving over to continuous space and expanding to second order spatial derivatives, we find, $\alpha = r - r_c$, $\beta = r$, $r' = r(1-\rho)$ and $D = \frac{r'}{2}$, where $r_c = 1$. This suggests a density dependence in r' and D: however, as shall now be explained, this is not expected to affect the wavefront behaviour.

In the subcritical regime the density profile tends to zero far from the boundary therefore $r' \to r$ and $D \to r/2$. Thus

$$v_{\text{sub}} = \sqrt{r^2 - 2r\alpha} = \sqrt{r_c^2 - \alpha^2} \simeq r_c - \frac{\alpha^2}{2r_c} + \dots \tag{3.28}$$

In the supercritical regime, on the other hand, ρ will tend to zero at the tip of the wavefront but be non-zero behind the Fisher wavefront. Thus at the tip $r' = r$ and the supercritical Fisher wave velocity becomes

$$v_{\text{sup}} = r + \sqrt{2r\alpha} \simeq r_c + \sqrt{2r_c\alpha}\,. \tag{3.29}$$

Therefore the derivative of the modified wave velocity is discontinuous at the phase transition. It is also interesting to note that with the identification of α and β, behind the wavefront in the supercritical regime we have $r' = r(1-\alpha/\beta) = r_c$

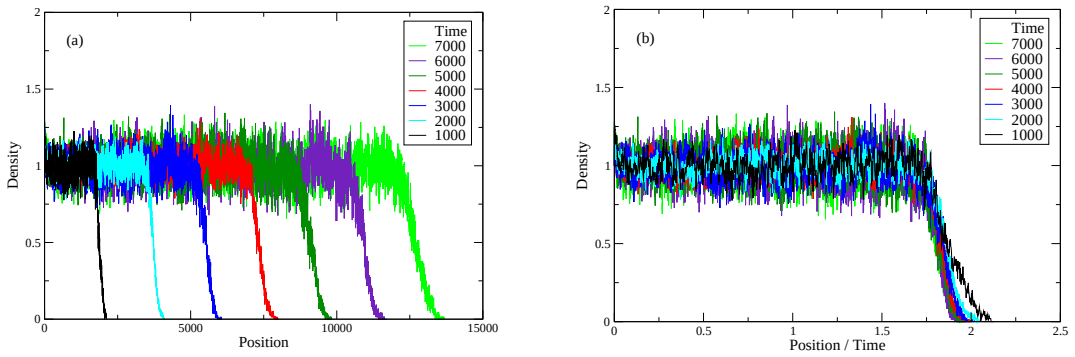

Figure 3.9: (a) The density versus position with the envelope divided out ($r = 3.3$). (b) The density versus position/time. The collapse shows that the velocity remains constant.

and the effective advection is fixed at the critical value.

3.7.2 Stochastic modified wave dynamics

We now return to the stochastic simulations of the DACP to investigate the picture of a modified wave travelling within a density envelope. In Fig. 3.4b, the density profile in the subcritical phase is shown at different time points along with an envelope of the form $\rho^*(x) = \exp(-A_0 x - A_1 x^{A_2})$, with the fitting parameters A_i all positive. As we get closer to criticality A_2 decreases, indicating an approach to the scaling form $e^{-x/\xi} x^{-\delta}$.

To obtain the modified wave $f(x-vt)$, we divide the numerical density profiles by this envelope equation. The result of this procedure is shown in Fig. 3.9a, which clearly shows a wave with constant bulk density invading an empty lattice. The constancy of the wave velocity can be checked by dividing the x coordinate by time (Fig. 3.9b). We do not, however, see strong evidence for the diffusive broadening of the wavefront predicted by (3.24). This could be because this equation applies only where the stationary density is small, a region that is hard to access numerically.

A key component of the scaling picture (section 3.5), seen explicitly within the mean-field dynamics (section 3.6), is the continuity of the intrinsic wave velocity across the transition. After unfolding the envelope (as in Fig. 3.9) one can obtain this velocity over a range of activation rates r. In Fig. 3.10, this velocity is compared with the apparent velocity before unfolding the velocity (i.e., the data of Fig. 3.3). The two velocities are clearly distinct in the subcritical regime

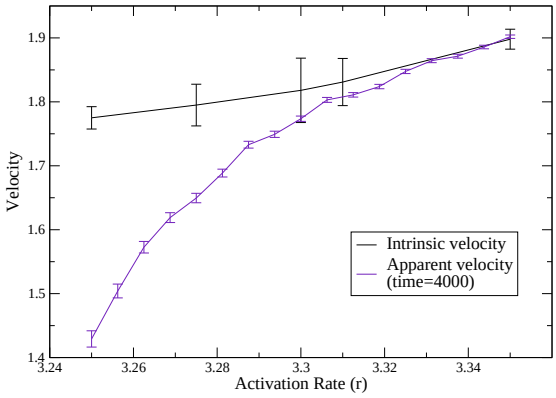

Figure 3.10: The intrinsic velocity: Velocity versus activation rate. A distinct difference between the apparent and intrinsic velocities is observed. Note that the apparent velocities only seems continuous due to finite-time effects.

($r < r_c \simeq 3.3$). Since the envelope decays exponentially in the subcritical phase, it is difficult to probe the late-time travelling-wave dynamics, and so the error bars on the modified wave velocity are necessarily large. However, the data suggest that the intrinsic velocity changes more slowly just below the critical point than above, in qualitative agreement with the mean-field predictions of equations (3.28), (3.29).

Finally, we attempt to access the exponent $\chi = \nu_{\parallel} - \nu_{\perp}$ by fitting the observed wave velocity in the supercritical regime to the form $v_{\rm sup} \sim v_c + A(r - r_c)^{\chi}$ suggested by the scaling picture of section 3.5 and confirmed within the mean-field regime by travelling wave analysis of section 3.6. It turns out that an estimate of χ is rather sensitive to the values of v_c and r_c used in a straight-line fit to $\ln(v - v_c)$ plotted as a function of $\ln(r - r_c)$. Taking $r_c = 3.3055$, we find the best fit (as quantified by the sum of square residuals) when $v_c \simeq 1.795$. The corresponding plot is shown in Fig. 3.11 along with a line of gradient $\chi = 0.637$, which is the appropriate choice for DP in one dimension. We see that the simulation data have a gradient that is consistently higher than the predicted value. It may be that corrections to the leading-order behaviour remain significant in the region we have been able to access numerically. We remark that reasonable straight lines are obtained for values of v_c in the range 1.70 to 1.84, yielding estimates of χ between 0.6 and 0.8 suggesting that the numerical data are consistent with the scaling prediction for χ.

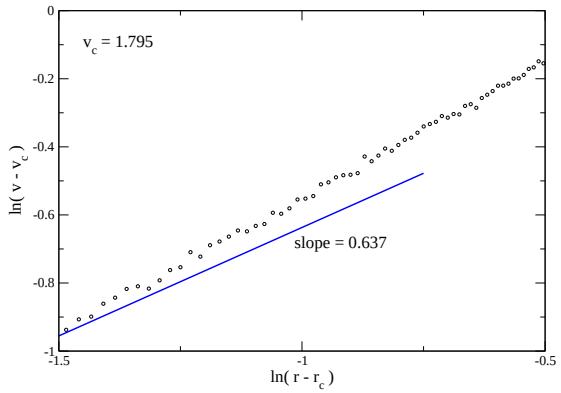

Figure 3.11: Velocity exponent χ measured in the stochastic simulations. Shown is $\ln(v - v_c)$ against $\ln(r - r_c)$ with $v_c = 1.795$ to obtain a straight line in the regime $r \to r_c$. The solid line has the gradient $\chi \simeq 0.637$ appropriate for Directed Percolation in one dimension.

3.8 Conclusion

In this chapter I have studied a variation of the contact process which includes an active boundary, which drives the system, and advection away from that boundary. As expected the system exhibits a phase transition from a state with activity localised near the boundary to a state where a wave of activity emanates away from the boundary. We identify the DP critical exponents β and $\nu_\parallel$ by considering the behaviour of the density far from the boundary and the spatial decay length over which the density decays to that value. On the other hand, the velocity of the activity wave emanating from the boundary exhibits some perhaps unexpected behaviour: in the subcritical phase the apparent velocity is zero whereas in the supercritical phase the velocity jumps discontinuously to a non-zero value. I have explained this phenomenon by studying a mean-field theory in which I show that an intrinsic velocity for a wave emanating from the boundary, described by (3.17), exists both below and above the transition. However in the subcritical regime the spatially decaying envelope for this wave means that the apparent velocity observed in the simulations is zero. This picture appears to hold well in simulations of the stochastic system.

The study raises several interesting questions. At the mean-field level it would be interesting to put the analysis of the modified Fisher equation (3.13), in particular the subcritical case, on a more rigorous footing.

The noisy version of the Fisher-KPP equation is known to describe contact processes [86]. It would of course be of great interest to further understand travelling wave solutions of the noisy version of the Fisher-KPP equation, in particular the velocity and width of the front.

It would also be of interest to investigate how common the feature of an envelope quenched velocity profile is. In section 3.4 we have already seen that a symmetric version of the DACP does not exhibit a velocity discontinuity. Similarly different Random Walker models also fail to reproduce this behaviour. By identifying what components, or which interplay of them, of the DACP are necessary for this feature it should be possible to identify other models displaying the same behaviour.

Chapter 4

A Zero-Range Process with Large Chipping

One of the fundamental models of condensation is the Zero-Range Process (ZRP), see section 2.3.2, which serves as a microscopic description for non-equilibrium condensation. The ZRP model that is normally considered is one where a single particle is allowed to hop from one site to another with rate $u(k) = 1 + b/k^{\alpha}$ where k is the occupancy of the departure site and both α and b are positive parameters. Such a system is known to undergo a condensation transition for $\alpha < 1$ or $\alpha = 1$, $b > 2$ [89] as the density is increased above the critical value $\rho_c = 1/(b-2)$ [50]. For a large but finitely sized system the condensate, once formed, remains static and only infrequently goes through a process by which it rapidly disappears and re-emerges at another site [44]. In this chapter I will investigate a modified ZRP where instead the majority of the particles at a site hop (chip) to the neighbouring site. With a large chipping mass one would expect possibly very different dynamics where a condensate, if formed, would propagate around the system. I will investigate the dynamics of this system and whether, as is the case for ordinary ZRP, it still yields a factorisable steady-state.

4.1 Motivation

The popularity of the ZRP means that the condensation transition has been widely studied. The dynamics of the condensation process was studied in [43, 50] and the effects of using an asymmetric hop rate were considered in [50]. The

dynamics of the condensate, once formed, were investigated in [44]. From these studies it is known that a one-dimensional ZRP where single particles hop between neighbouring sites undergoes a continuous condensation transition independently of the hop bias.

Starting from a disordered state the condensate evolves by a coarsening process whereby the number of populated sites decays as $N/t^{1/z}$ where N is the total number of particles in the system and z is the (non-stationary) dynamical exponent defined in section 2.1.1. Thus after a time of order N^z the system contains a finite number of proto-condensates which die-off until finally only one condensate is present. As the proto-condensates grow they also become increasingly long lived. The typical time taken for a proto-condensate to lose all of its n particles is found to scale[1] as $t(n) \propto n^z$ [50]. The time taken for all of the proto-condensates bar one to die-off is again of order N^z. Once the condensate is formed it remains stationary with the exception of rare events in which it dissolves and then quickly reforms at a random site. These events occur at a characteristic time scale of N^Z [44], where Z is the stationary dynamical exponent. Both exponents z and Z depend on the dimensionality of the problem and on the symmetry of the hop rates. The dynamical exponents for a one-dimensional ZRP with $\alpha = 1$ are given in table 4.1. We note that for the system to condense we require $b > 2$. Further we note that the mean-field values are the same as those for totally asymmetric hop dynamics. Thus the dynamics of this process is affected by a left-right bias in the hop rate even though the steady-state is not.

Geometry	z	Z
MF, 1DA	2	b
1DS	3	$b+1$

Table 4.1: A comparison of dynamical exponents for the ZRP in a mean-field approximation (MF) and in one spatial dimension with totally asymmetric (1DA) or symmetric (1DS) hop rates [44].

In this chapter I am interested in investigating a ZRP-like system exhibiting a propagating condensate. The suggested model is therefore one where instead

[1] This scaling behaviour only holds while there are still multiple proto-condensates. At the latest it ends when the third largest proto-condensate has disappeared.

of single particles leaving a site for a neighbouring one we now have the majority of particles leaving the site at the same time. So as to keep the model mirroring the usual ZRP as closely as possible we specifically consider a model where all but one of the particles leaves at each hopping event. Since hopping for systems with continuous mass is usually referred to as 'chipping' we refer to this model by the more general: Zero-Range Process with large chipping (or the Chipping model for short).

It is worth mentioning two other models which exhibit propagating condensates. The Conserved-Mass Aggregation Model (CMAM)[2] [78, 92] is a mass transport model with a condensation transition. In this model the particles on a site may either chip, in either direction, ($\{m_i, m_{i\pm1}\} \to \{m_i - 1, m_{i\pm1} + 1\}$) or diffuse and aggregate ($\{m_i, m_{i\pm1}\} \to \{0, m_{i\pm1} + m_i\}$). The system undergoes a transition from a state where the mass distribution decays exponentially to one where the mass distribution decays as a power law but with a delta function at $m = \infty$ i.e., a state where there is co-existence between a condensate made up by a finite fraction of the total mass and smaller finite clusters whose mass distribution has power-law tails. An asymmetric version of this model was introduced in [79] and has since been used as a traffic model with passing [58]. The asymmetric version exhibits a propagating condensate albeit one which is different from that which is investigated here.

A recent study [112] looked at the Misanthrope process [24], a variation of the ZRP where the hop rates depended on the occupation of both departure and arrival site such that a particle hops from site i to site $i+1$ with rate $u(m_i, m_{i+1})$. This study investigated hop rates which for large occupancies on *both* sites scale as $u(m, n) \sim (mn)^\gamma$ for $\gamma > 0$. In this case a condensate propagating through the system is observed. However in this system the dynamics were found to speed up over time resulting in 'explosive' condensation. Although based on the ZRP this system is therefore significantly different from the model studied in this chapter where we seek a condensate which propagates with a finite velocity.

[2]Sometimes also referred to as the Chipping model (CM).

4.2 Microscopic model

The Zero-Range Process with large chipping [hereafter the Chipping model] is a stochastic model defined on a one-dimensional periodic lattice, with L sites, occupied by N particles. A microscopic configuration, $\{n_i(t)\}$, specifies the number of particles at each site at a given time. The dynamics are limited to two mutually exclusive moves. If the population of a site is $n_i > 1$ then $n_i - 1$ of the particles can hop (chip) to the site directly to the right with rate $u(n_i)$. If the population of the site is $n_i = 1$ then that particle hops to the next site to the right with rate $u(1)$. Neither case is affected by the population at the target site. See Fig. 4.1 for an illustration.

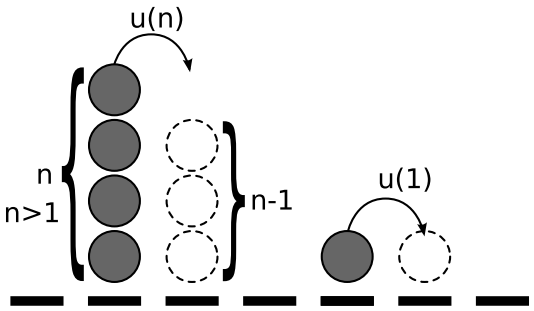

Figure 4.1: The Chipping model. For a site with $n > 1$ particles all but one of the particles can hop to the right with rate $u(n)$. In the case where there is only a single particle on the site it can hop to the right with rate $u(1)$.

The rate at which the hopping occurs is given by

$$u(k) = u_\infty \left(1 + \frac{b}{k^\alpha}\right) , \tag{4.1}$$

where k is the number of particles on the site *before* the hop is performed. The time-scale for the hopping process is governed by u_∞ which is set to 0.25 throughout this chapter. It is worth stressing that $u(n)$ and $u(1)$ have the same form, it is only whether one particle remains at the departure site or not which differs.

The separate move for single particle sites is needed to avoid a model where the solution is, trivially, an absorbing state. Without this move a state where each site contains either one stationary particle or no particles is always reached for $\rho = N/L \leq 1$. For $\rho > 1$ once a particle has been deposited on each site the

remaining particles form one condensate which moves across the lattice. Since there is no process by which the condensate can break apart, this too would be an absorbing state.

4.2.1 Comparison to the standard ZRP

In section 2.3.2 we saw how the ZRP was shown to have a factorisable steady-state. That is, the probability of finding a periodic system with N particles and L sites in the steady-state configuration $\{n_i\}$ is given by

$$P(\{n_i\}) = Z_{L,N}^{-1} \prod_{i=1}^{L} f(n_i) \delta \left(\sum_{i=1}^{L} n_i - N \right) \quad \text{with} \quad f(n) = \prod_{i=1}^{n} u(i)^{-1} \, . \tag{4.2}$$

This proved an important feature of the ZRP since it allowed it to be solved exactly.

The result was generalised in [36, 114] to models where, instead of an integer number of particles on each site, we consider a continuous mass where an arbitrary amount may move from one site to another. Given a site of continuous mass n a chipping mass μ is drawn from a distribution $\varphi(\mu|n)$. The chipping mass is transferred to a neighbouring site. This is then repeated for every site at each time-step. With this choice of discrete-time dynamics the probability of observing the configuration $\{n_i\}$ evolves as

$$P_{t+1}(\{n_i\}) = \prod_{i=1}^{L} \int_0^{\infty} \mathrm{d}n_i' \int_0^{n_i'} \mathrm{d}\mu_i \, \varphi(\mu_i|n_i') \prod_{j=1}^{L} \delta(n_j - n_j' + \mu_j - \mu_{j-1}) P_t(\{n_i'\}) \, . \tag{4.3}$$

The right hand side of this equation is integrating over all allowed configurations before the update, i.e. where a mass μ_l was moved from site l to site $l+1$ at the update and site l had a mass $n_l' = n_l + \mu_l - \mu_{l-1}$ before. It was shown in [36] that for the steady-state to factorise, i.e.

$$P(\{n_i\}) = \lim_{t \to \infty} P_t(\{n_i\}) = Z_{L,N}^{-1} \prod_i f(n_i) \, , \tag{4.4}$$

a necessary and sufficient condition is that the chipping distribution takes the

form

$$\varphi(\mu|n) = \frac{v(\mu)w(n-\mu)}{[v*w](n)} \ , \tag{4.5}$$

where v and w are non-negative functions and $*$ is the convolution operation. The $f(n)$ factors are then given by

$$f(n) = [v*w](n) = \int_0^n v(\mu)w(n-\mu)\mathrm{d}\mu \ . \tag{4.6}$$

This is further extended to a system with random sequential dynamics with a continuous time-step by letting the probability of an event be proportional to the time-step $\mathrm{d}t$ such that to leading order in $\mathrm{d}t$ at most one event occurs per time-step. Thus as $\mathrm{d}t \to 0$ we get

$$v(\mu) = \delta(\mu) + x(\mu)\mathrm{d}t \ , \tag{4.7}$$

where x is also an arbitrary function. Substituting this into (4.5) the condition thus reduces to the hop rates distribution function $\gamma(\mu|n)$ taking the form

$$\gamma(\mu|n) = \frac{\mathrm{d}}{\mathrm{d}t}\varphi(\mu|n) = \frac{x(\mu)w(n-\mu)}{w(n)} \ \text{ for } \ \mu > 0 \ , \tag{4.8}$$

where we now have $f(n) = w(n)$ [36].

The continuous time factorisation condition (4.8) can now be used to compare the steady-state of the Chipping model with that of the ZRP. For a system with discrete mass the hop rate distribution function can be calculated by

$$\gamma(\mu|n) = \sum_{m=1}^{\infty}\sum_{l=1}^{m}\phi_{l,m}\delta_{\mu,l}\delta_{n,m} \tag{4.9}$$

where $\phi_{l,m}$ is the rate at which mass l chips from a mass m and where $\delta_{k,l}$ is the Kronecker delta defined through

$$\delta_{k,l} = \begin{cases} 0 \ \text{ for } \ k \neq l \ , \\ 1 \ \text{ for } \ k = l \ . \end{cases} \tag{4.10}$$

For the standard ZRP where single particles hop between sites, the hop rate

distribution function takes the form

$$\begin{aligned}\gamma(\mu|n) &= \sum_{m=1}^{\infty} \phi_{1,m}\delta_{\mu,1}\delta_{n,m} \\ &= u(n)\delta_{\mu,1} \quad \forall n, \mu \geq 1 \ .\end{aligned} \tag{4.11}$$

As expected this can clearly be written in the form of (4.8). Looking at the Chipping model we observe that $\gamma(\mu|n)$ takes the form

$$\begin{aligned}\gamma(\mu|n) &= \phi_{1,1}\delta_{\mu,1}\delta_{n,1} + \sum_{m=2}^{\infty} \phi_{m-1,m}\delta_{\mu,m-1}\delta_{n,m} \\ &= u(1)\delta_{\mu,1}\delta_{n,1} + u(n)\delta_{\mu,n-1} \quad \forall n, \mu \geq 1 \ .\end{aligned} \tag{4.12}$$

Since this form involves a sum it does not satisfy the factorisation condition. Thus the fairly minor modification to the ZRP process is sufficient to give a non-factorised steady-state.

Although the Chipping model may initially appear to be symmetrically related to the standard ZRP the dynamics of single particle sites breaks this symmetry. This becomes apparent if we consider a non-stochastic realisation of the models and change to a frame of reference which moves at the speed associated with the rate $u(1)$. For illustrative purposes we consider $u(k) =$ constant, see Fig. 4.2. Here we observe that the Chipping model, in the co-moving reference frame, maps directly to the standard ZRP model, with the exception of the dynamics of the single particle site. Similarly the standard ZRP in the co-moving reference frame can be compared to the Chipping model.

4.3 Initial results

The first results for the system came from performing Monte Carlo simulations, using the Next Reaction Method (section 2.4), of the microscopic Chipping dynamics specified in section 4.2 above. The lattice was initialised as randomly populated and was then allowed to evolve until a steady-state was reached. To determine the probability of observing a microstate (once the steady-state is reached) the lifetime of each microstate is recorded each time it is observed. The probability is then given by the sum of the lifetimes for that microstate normalised

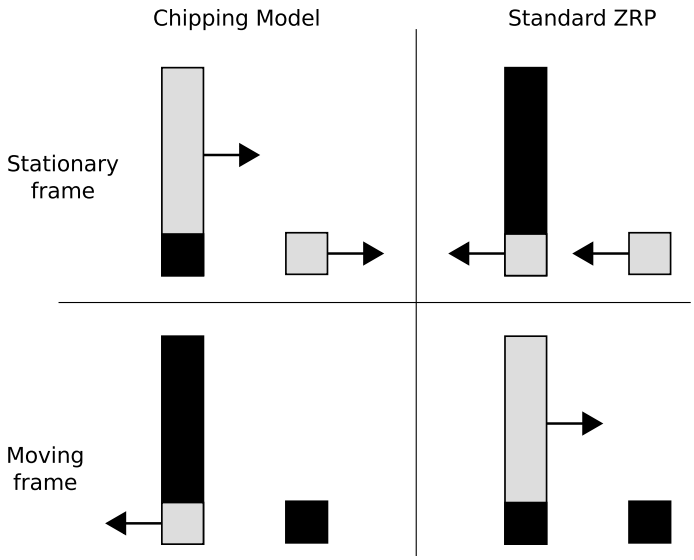

Figure 4.2: A comparison of the Chipping model (left) and the standard ZRP (right) with constant hop rates. The models are depicted in a stationary reference frame (top) and in one which moves with the hopping particles (bottom). Grey indicates the part of a pile which moves and black that which remains. The smaller pile illustrates a site with a single particle. Note that this illustration is only strictly valid in a non-stochastic realisation where rates correspond directly to velocities.

by the sum of the lifetimes for all microstates.

The system was initially investigated for hop rates given by (4.1) with $\alpha = 1$ since this is the value for which the standard ZRP is known to undergo a condensation transition for $b > 2$. Since the primary interest is in the effects of varying b (and later α) the density was taken to be constant throughout the simulations. By choosing $N/L = \rho = 0.7$ the density was assumed to be sufficiently large to allow condensation to occur where possible, we will return to this assumption in section 4.4.1.

The first observation from the simulations is that there exist two steady-states depending on the value of b. One in which multiple small clusters propagate through the system and one in which there is a single large condensate moving through the system followed by a short tail of small clusters (see Fig. 4.3 for an illustration).

The tail stems from how the condensate propagates. When the condensate moves it, temporarily, leaves one particle behind. Since this may occur multiple

times before the first particle rejoins the condensate a tail of particles develops. Thus we see that such a tail is a natural feature of any condensate in this system. The tail clearly illustrates why this model no longer exhibits a factorised steady-state.

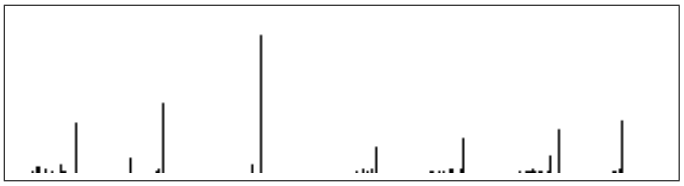

Figure 4.3: A screenshot of the Chipping model showing proto-condensates propagating (to the right) and followed by their tails.

The condensate was further investigated by plotting $P(k)$, the probability of observing a site with a certain occupancy, against the fractional occupancy k/L, Fig. 4.4a. By studying various system sizes, at the same density ρ, a collapse was obtained which shows that the condensate scales with system size. Furthermore since the condensation 'bump' is observed very close to ρ we can deduce that (effectively) all particles are in the condensate with the background density being zero. It should further be noted that the tail structure (low occupancy sites) does not scale with system size, rather it appears to be completely independent of system size.

To investigate how this condensate changed as a function of b a cumulative particle density measure was introduced. This measure is defined as

$$C(k) = \frac{1}{N} \sum_{k'=k}^{N} k' P(k') \ , \tag{4.13}$$

i.e. the fraction of all particles which can be found at occupancies larger than k. Plotting $C(k)$ against k, Fig. 4.4b, shows that the condensate appears at some critical value b_{crit}. Above this value the condensate appears to grow continuously.

The $\alpha = 1$ results show that there exists a condensation transition in b, Fig. 4.4, for the Chipping model just as it does in standard ZRP. This transition is known to be absent in standard ZRP for other values of α. For $\alpha > 1$ condensation cannot occur and for $\alpha < 1$ it occurs independently of the value of b. However investigating the Chipping model for other values of α we find that this transition is still present, Fig. 4.5.

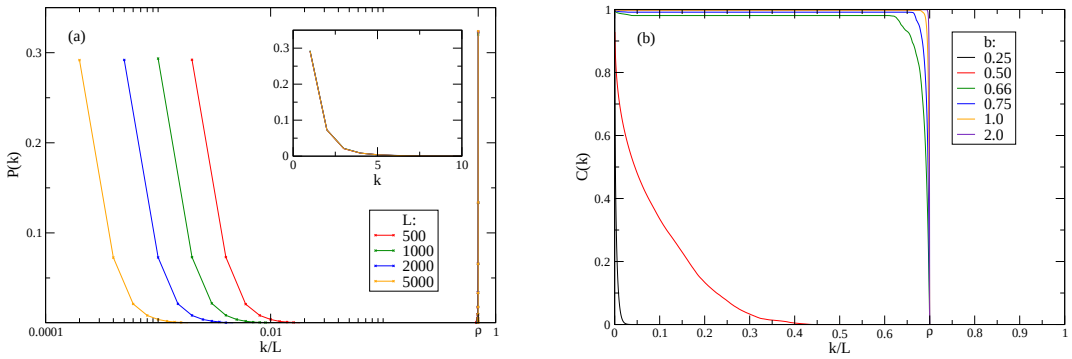

Figure 4.4: Condensation in the Chipping model for $\alpha = 1$.
(a) The probability of observing an given occupancy for various system sizes, here $b = 2$. Shows how the condensate scales with system size whereas the tail (inset) does not. Further note that the condensate occurs at $\rho = N/L$, thus all particles (bar those in the tail) can be found in the condensate. Note that the data points for the condensate all lie on top of each other, as do the data points in the inset.
(b) The cumulative particle density for various values of b, here $L = 2000$. Shows how the condensation appears at some critical value $b_{crit} \in (0.5, 0.66)$. Note that the growth of the condensate appears to be continuous.

These discoveries indicate that, unlike ZRP, it is not (primarily) the functional form of the hop rates which determine if condensation is possible. With functional form I here mean the value of α since the constant term in the hop rate is needed to maintain a non-zero hop rate in the limit of large occupancies. For the chipping model the results suggest that condensation is determined by the value of b in such a way that b_{crit} is a function of α. This suggests that it is the b/k^{α} term, which we shall refer to as the 'amplitude', of the rate which is critical to whether condensation may occur or not. To better understand the system we will now investigate a slightly different instance of the Chipping model.

4.4 A recurrence approach

In this section we investigate a slight modification to the Chipping model as defined in section 4.2. The dynamics are the same as before but instead of having periodic boundary conditions the dynamics now occur on a (semi)infinite lattice. The system starts evolving from a condensed state where all particles are found on a single site at the leftmost end of the lattice. Although this may

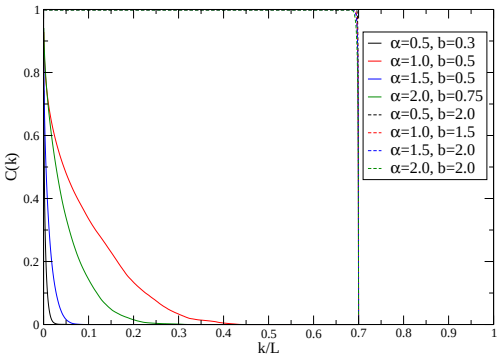

Figure 4.5: The cumulative particle density for various values of α, each for two values of b. This clearly illustrates that for different values of α we observe a transition from an uncondensed state (solid line) to a condensate (dashed line) as b is increased. Here shown for $L = 2000$ and $\rho = 0.7$. Note that the dashed lines all lie on top of each other.

initially seem like a somewhat unusual, zero density, limit we will find that it allows a way of studying the b and α dependence in condensation without the added complication of density.

The property of interest is the probability of recurrence, P_r, i.e. the probability that the condensate will reform at any later point in time. The probability of recurrence is commonly studied in Markov Chain situations from which it is known that if $P_r < 1$ then the condensate is merely a transient feature. The reasoning for this is that once the system is fully condensed it is indistinguishable, up to a translation, from the initial condensed state from which it evolved. Thus a series of repeated measurements, for which condensation is observed, can be viewed as one long simulation of a system which condenses, breaks up and then re-condenses. By contrast if condensation does not occur in one measurement then this describes a critical event from which the system does not recover and after which condensation is never observed again.

In practice any simulations must be limited to a finite-sized lattice. Thus we assign a point ($L_{\max}$) on the lattice and if this is reached by a particle then we say the condensate will not reform. A statistically significant number of 'no recurrence' events are therefore needed in order to establish that a condensate is in fact transient. However since most condensation events are observed soon after initialisation of the simulation[3] we can still afford, computationally speaking,

[3]In my simulations 95%+ of all condensation events are observed before the leading front advances more than five sites from the origin.

large lattices. Here we will only consider the $L_{\max} = 10^4$. Increasing the lattice size beyond this was found to only have a negligible effect on the results.

The second parameter, and possible second source of finite size effects, to consider is the system size (i.e. number of particles, N). For sufficiently large systems ($N \sim 1000$ particles) the results are largely unaffected by further increases in system sizes. It should be noted however that the smaller the value of α the more sensitive the results remained to particle numbers.

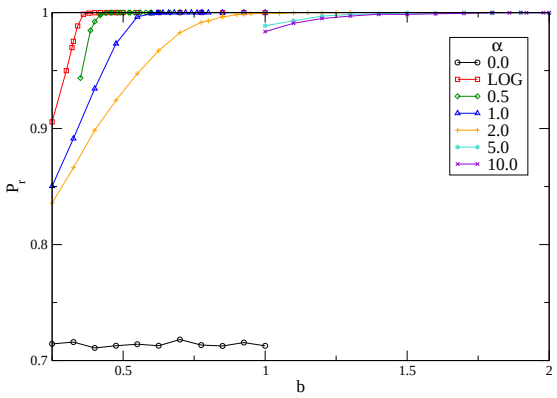

Figure 4.6: Probability of recurrence, P_r, against b for several values of α. For all non-zero α, including the logarithmic approach, $P_r = 1$ is observed for some value of b.

The result of the recurrence simulation, Fig. 4.6, shows that for all considered values of α there exists a critical value, b_{crit}, above which recurrence is always observed. This is in stark contrast to the ZRP where condensation is only possible for $\alpha \leq 1$. We now observe results which suggest condensation occurs for any $\alpha > 0$. This further reinforces the notion that it is the amplitude, b/k^α, rather then the functional form of $u(k)$ which controls condensation in the Chipping model.

In Fig. 4.6 we have also included data for a system which uses the alternative hop rate

$$u_{\log}(k) = u_\infty \left(1 + \frac{b}{\ln(k+1)}\right) . \tag{4.14}$$

This allows us to consider the usual hop rate for an infinitesimally small α (for sufficiently large k). Interestingly we see that even this gives us a critical b value above which condensation occurs whereas $\alpha = 0$ does not. Estimating b_{crit} from these simulations allow us to plot a rough phase diagram, Fig. 4.7. We note that

larger values of α meet the $P_r = 1$ line at a shallower angle making it difficult to determine the exact value of b_{crit}. The smaller values of α on the other hand are more sensitive to the system and lattice size.

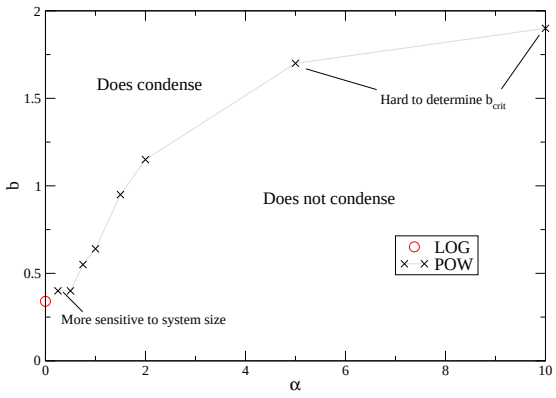

Figure 4.7: A rough phase diagram for the Chipping model as obtained from the recurrence approach.

In a similar manner the recurrence probability (or rather occurrence probability) can also be measured in the original system, i.e. with all particles randomly distributed initially and with periodic boundary conditions[4]. Again we find that there exists a b_{crit} for each positive value of α above which $P_r = 1$. The difference is that the transition is now a rapid change from a 0 to 1 probability of recurrence, which supports the previous interpretation that $P_r < 1$ is indicative of a system which does not condense.

However these measurements were highly sensitive to other parameters, especially density, meaning the specific b_{crit} values found above could not be recovered. In addition any large scale measurements were so slow as to be computationally prohibitive. Thus we shall merely use this as confirmation of the validity of the recurrence approach.

Armed with the results of the recurrence approach we now seek to explain the mechanism by which this model can undergo condensation for any value of α. Before this however, a short aside on the role of density.

[4]Note that periodic boundary conditions are necessary for observing condensation in an initially randomly distributed system.

4.4.1 Low-density condensation and asymmetric hop rates

The recurrence approach also shows us that the condensation transition is present even in the low-density limit. This is unlike usual condensation scenarios, such as for the ordinary ZRP, where a minimum density is required for condensation to be possible. However we only know that this is possible for a nucleated system, i.e. one started from a condensed state.

Simulations of the normal Chipping model, as described in section 4.3, have further indicated that condensation is still present for densities $\rho \in [0.1, 0.9]$, Fig. 4.8a. To fully verify low-density condensation in the Chipping model would require investigating even lower density periodic lattices, initialised with randomly distributed particles. This is however prohibitively expensive, computation-wise, since a very large lattice is required in order to reduce the density whilst maintaining enough particles for a condensate to be clearly identifiable.

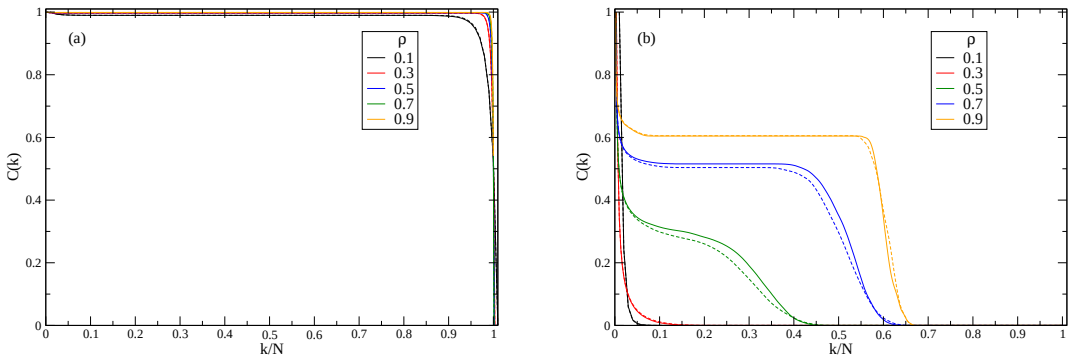

Figure 4.8: A plot of the cumulative particle density against fractional occupancy, for various densities. All plots are for $\alpha = 1$ and $b = 2$ and include values for two separate initial conditions (solid and dashed lines) to illustrate finite-time effects. (a) For the normal Chipping model with totally asymmetric hopping. (b) For a Chipping model with symmetric hopping.

Further simulations were performed of a realisation of the Chipping model with symmetric hop rates. Whereas we still observe condensation for values of $\alpha > 1$ there are a few important differences to the normal asymmetric Chipping model. The most obvious difference is that without the asymmetry the condensate will no longer propagate along the lattice, instead it performs a random walk on the lattice. We observed in Fig. 4.4 that in the condensed phase of the Chipping model virtually all particles are found in the condensate. In contrast

the symmetric case displays a non-zero background density of particles in the condensed phase. We also find that as the particle density is decreased the proportion of particles found in the condensate decreases further, Fig. 4.8b. Finally below some minimum density we observe that the condensate disappears completely.

Thus it would appear that the low-density condensation—at least in a nucleated system—is a feature of the Chipping model directly connected to the hop rate asymmetry.

4.5 A Smoluchowski mean-field approach

A natural first approach to understanding our results is through a mean-field approximation. Here we shall use one which is based on the Smoluchowski coagulation equation whereby the spatial distribution of the sites may be neglected.

The Smoluchowski coagulation equation was introduced in 1916 [103] as a mathematical model for a large system of particles which coagulate pairwise over time. Since the rate at which coagulation occurs is normally taken to be dependent on the mass of the particles this model further assumes that any spatial fluctuations of the mass density are negligible. In higher dimensions this can be realised by having the particles perform a random, independent, walk at timescales much shorter than that of coagulation. The end result is a system where any particle can coagulate with any other particle. For such a system Smoluchowski wrote down the following infinite system of differential equations for the evolution of the number densities $n_t(k)$ of particles of discrete mass k:

$$\dot{n_k}(t) = \frac{1}{2}\sum_{l=1}^{k-1} K(l, k-l) n_l(t) n_{k-l}(t) - n_k(t) \sum_{l=1}^{\infty} K(k, l) n_l(t) \; . \tag{4.15}$$

The first sum describes the gain due to smaller particles coagulating into a particle of mass k whereas the second sum describes the loss due to particles of mass k coagulating with other particles to make larger particles. $K(k, l)$ is the coagulation kernel which describes the rate at which particles of mass k coagulate with particles of mass l. Due to the double counting resulting from the first sum considering both particles involved in the coagulation a factor of a half

is introduced before this sum.

For the Chipping model we consider the evolution of densities of sites with discrete occupancy instead. When constructing the mean-field equation we need, in addition to the two terms above, to describe the effect of cluster decay (decoagulation) as well as the special behaviour of single particle sites. The first term of (4.16) therefore represents sites of different occupancies combining to make a cluster of occupancy k. The second term is the contribution from sites of occupancy k combining with any other sites to form one with a larger occupancy. The third (fourth) term represent a site of occupancy $k+1$ (k) decaying into a site of occupancy k ($k-1$) and a site with a single particle. The last term covers the fact that any decay will produce sites with single particles. Thus, dropping the explicit time dependence, the Smoluchowski mean-field approach for the Chipping model becomes

$$\begin{aligned}\dot{n_k} = &+ \sum_{l=1}^{k-1} \left[\frac{1}{2}\left(1+\delta_{l,k-l}\right) n_l n_{k-l}\right] \frac{f(k-l,l)}{U} - \sum_{l=1}^{\infty} \left[\left(1+\delta_{l,k}\right) n_l n_k\right] \frac{f(k,l)}{U} \\ &+ n_{k+1}\frac{u(k+1)}{U} - n_k \frac{u(k)}{U} \\ &+ \delta_{k,1} \sum_{l=1}^{\infty} n_l \frac{u(l)}{U} \ ,\end{aligned} \tag{4.16}$$

with

$$u(k) = \left(1 + \frac{b}{k^{\alpha}}\right) \ , \quad f(k,l) = \frac{u(k)+u(l)}{2} \ , \quad U = \sum_{k=1}^{N} n_k u(k) \ , \tag{4.17}$$

where the U term is used to normalise the available rates. Here we have assumed that the coagulation kernel $f(k,l)$ is simply proportional to the average hop rate out of the two sites.

In the two first terms special attention is paid to the case when sites of the same occupancy merge. For the first term this means that there is no longer any double counting, thus we cancel the factor of a half. When a site of occupancy k merges with another site of the same occupancy two sites of occupancy k are lost, thus we introduce a factor of two for the second term. For an infinite system these corrections make little difference, which is why they are not present in (4.15).

To solve the equations numerically we need to consider a system with a finite

number of particles. The primary effect of this is that particular attention is required for the number densities for coagulation between sites of the same occupancy. Thus the finite size equation for the system becomes:

$$\begin{aligned}\dot{n_k} = &+ \sum_{l=1}^{k-1} \left[\frac{1}{2} \left(1 - \delta_{l,k-l}\right) n_l n_{k-l} + \delta_{l,k-l} \theta[n_l - 1] n_l (n_{k-l} - 1) \right] \frac{f(k-l,l)}{U} \\ &- \sum_{l=1}^{N} \left[\left(1 - \delta_{l,k}\right) n_l n_k + 2\delta_{l,k} \theta[n_k - 1] n_l (n_k - 1) \right] \frac{f(k,l)}{U} \\ &+ \left(1 - \delta_{k,N}\right) n_{k+1} \frac{u(k+1)}{U} \\ &- n_k \frac{u(k)}{U} \\ &+ \delta_{k,1} \sum_{l=1}^{N} n_l \frac{u(l)}{U} \ ,\end{aligned} \tag{4.18}$$

where $\theta[n]$ is the normal Heaviside function as defined in (2.43).

Equation (4.18) can be solved numerically using the *midpoint method*[5] [91] whereby

$$n_k(t + \mathrm{d}t) = n_k(t) + \dot{n_k}\left(t + \mathrm{d}t/2\right) \mathrm{d}t \ \text{ with } \ \dot{n_k}(t) = \dot{n_k}\left(n_k(t)\right) \ . \tag{4.19}$$

Solutions for this equation are shown in Fig. 4.9a for a range of α at a fixed value of $b = 0.25$. In Fig. 4.9b a cumulative measure, similar to that in (4.13), is introduced to show how the transition sharpens as the system size is increased. To illustrate the finite-time effects the values are shown for two separate initial conditions.

These calculations show that the mean-field version of our system gives condensation for any value of α, including $\alpha = 0$, independently of b. Thus we find that the spatial structure of our model is critical to the existence of a condensation transition.

To understand this effect we consider how a particle which has been left behind by the condensate may 'catch-up' with the condensate again. In the 1D system the particle has to travel the distance separating it and the condensate. The longer time this takes the larger is the chance that the condensate moves, thus

[5] Also known as the *second-order Runge-Kutta* or *modified Euler* method.

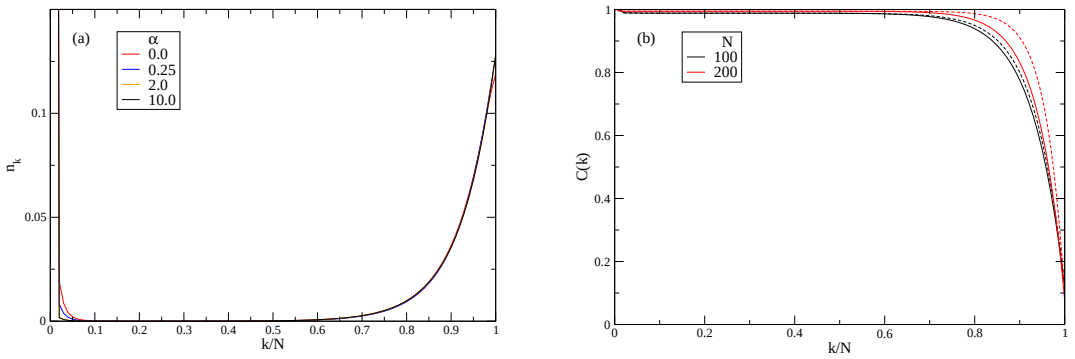

Figure 4.9: A Smoluchowski mean-field approach, showing condensation occurring independently of the value of α. All plots are for $b = 0.25$. (a) The number density against fractional cluster size at different α. (b) The cumulative mass density at $\alpha = 0.0$ for two systems of different sizes ($N = 100$, 200), showing how the transition sharpens as system size is increased. The plot includes values for two separate initial conditions (solid and dashed lines) to illustrate finite-time effects.

losing a second particle. By contrast in the mean-field picture any particle which falls behind is only ever one hop away from rejoining the condensate. This image readily translates to a situation with a proto-condensate some distance away from the main condensate. In the MF picture the proto-condensate may transfer the bulk of its constituents (all bar one particle) to the main condensate in a single hop. Meanwhile in the 1D system the proto-condensate would have to traverse the separating distance, during which it risks breaking up.

4.6 Observations and discussion about the underlying mechanism

In section 4.3 we observed that the existence of a b_{crit} for any positive value of α means that the amplitude of $u(k)$, rather than its functional form, determines if condensation can occur. We now examine this statement more closely by considering the rate function at criticality, $u_{crit}(k) = u_\infty(1 + b_{crit}(\alpha)/k^\alpha)$. Using the values for b_{crit} obtained from the recurrence approach (Fig. 4.7) we may now plot the rate function at criticality against occupancy, Fig. 4.10. It should be noted that the plots are limited by the accuracy at which b_{crit} could be determined. This has a particular impact on the extremal values of α.

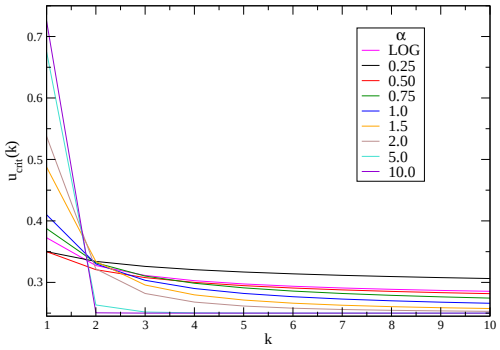

Figure 4.10: The rate function at criticality, $u_{crit}(k)$, against occupancy for various values of α. The plot suggests that there is an intersection at k =1.5–2.5 which is critical for determining condensation.

The plot shows that there is a roughly common intersection at an occupancy of $k \sim 2$. We interpret this as an indication that it is the rate of the $k = 2$ occupancy which determines if the system condenses. Thus assuming $u(k)$ is a decreasing function in k it would appear that condensation only occurs if $u(2) \geq u_{crit}(2)$. This is markedly different from normal ZRP where $u(k)$ is required to decay sufficiently slow for condensation to be observed.

We may now combine this with the observation from section 4.5 that the spatial structure is a key element for the condensation transition. The spatial structure involving low occupancy sites is in fact the tail which we observed following any condensate or proto-condensate. This is further supported by the observation (Fig. 4.4a) that the tail is independent of system size, meaning it is always the same occupancies governing its behaviour. Bringing all of these things together allows us to sketch the underlying mechanism by which condensation occurs or not.

Thus my hypothesis is that the mechanism by which a condensate, or proto-condensate, breaks apart may be described as follows. As the condensate moves forward a single particle is left behind and the condensate speeds up, albeit by a negligible amount for a large condensate. Most of the time this move is followed by the single, much faster, particle rejoining the condensate. However due to the stochastic nature of the system there is a finite probability that the condensate will move again before this happens. If so then there are now two sites behind the condensate each occupied by a single particle, each equally likely to move. If the rearmost of these moves then the rate at which a particle leaves the site which

now contains two particles is significantly reduced thus increasing the probability that the condensate has time to move again before one or both of these particles rejoin it.

Each particle which is left behind by the condensate slows the tail down further. If enough particles make up this tail then proto-condensates, with their own tails, will start to appear within it. These will largely behave like the main condensate with the one difference that their relative gain in speed from decreasing in size (by leaving a particle behind) will be larger. This process can be readily observed in the videos for the recurrence simulations.

Thus we come to understand that it is the probability that the initial tail rejoins the condensate which governs whether the system supports condensation or not. This probability is primarily governed by the hop rates of the low occupancy states.

4.7 Conclusion

In this chapter I have investigated a zero-range process with large chipping, the Chipping model. This is a ZRP model with hopping events occurring at rate $u_\infty(1+b/k^\alpha)$ where k is the occupancy of the departure site. Where the chipping model differs from the basic ZRP is in the definition of a hopping event. In the Chipping model all but one of the particles at the departure site leave for the target site in a single hopping event. The exception to this rule is that the departure site is completely vacated if it only contains a single particle at the time of the event. We find that this exception to the rule prevents the Chipping model from being mapped to the ZRP.

Simulations show that as b is varied the Chipping model undergoes a condensation transition from a state in which multiple small clusters propagate through the system to a state where a single large condensate moves through the system followed by a short tail of low occupancy sites. This tail illustrates why the Chipping model, unlike the ZRP, does not exhibit a factorised steady-state.

We find that the transition is present at a finite $b_{crit}(\alpha)$ for *any* value of $\alpha > 0$. This is distinctly different from the ZRP which only undergoes a condensation transition when $\alpha < 1$ or for the case when $\alpha = 1$ and $b > 2$. This indicates that it is not the functional form, but rather the amplitude, of the hop rate which

regulates condensation in our model.

We construct a recurrence realisation of the model in which the survival probability of an introduced condensate is measured in the zero-density limit. By identifying the survival probability as equivalent to the probability of condensation the $b_{crit}(\alpha)$ values are measured and a rough phase diagram is constructed. Using these measurements the hop rates at criticality are calculated. When plotted against the occupancy these rates suggest that it is the hop rates of the low occupancy sites which control whether condensation is observed. Again we observe that this differs from the basic ZRP. In our model condensation requires the decay of $u(k)$ with k to be sufficiently slow for the smallest values of k. By contrast the ZRP requires the decay to be slow for *all* values of k.

Introducing a Smoluchowski mean-field approach shows that the spatial structure of the model is key to the existence of a condensation transition. We identify the spatial feature involving low occupancy sites as the tail which follows the condensate. This suggests that it is the dynamics of said tail which controls condensation in the Chipping model.

I therefore suggest the following hypothesis for the underlying condensation mechanics. A condensate, or proto-condensate, breaks up if a tail forming behind it fails to rejoin the condensate sufficiently fast. The longer the tail spends behind the condensate the larger it grows and the more it slows down. Based on the above observations I suggest that it is the average speed, and thus the hop rate, of the low occupancy sites—in particular $k = 2$—which governs whether, on average, the tail will rejoin the condensate. Thus we require the decay of the hop rates with occupancy to be sufficiently slow *for the lowest occupancies* in order to observe condensation.

There are several areas of research related to the Chipping model which would be of interest to pursue. Foremost of these would be to devise a test by which the hypothesis regarding the condensation mechanism could be confirmed. One suggestion would be a piecewise hop rate with two decaying parts separated by a drastic drop at some k^*. By adjusting this k^* it might be possible to determine if it is only the rates of $k \leq 2$ which are relevant for condensation. Any such endeavour would most likely also require larger simulations so as to more accurately determine b_{crit} as a function of α.

During my investigation of the Chipping model I primarily worked in the high

density regime. It would therefore be of interest to investigate how the critical density is related to b and α. In particular it would be interesting to confirm whether there is condensation even in the zero-density regime as suggested by the recurrence approach. If we can show that zero-density condensation is present even in the non-nucleated system then this would illustrate yet another difference to the ZRP where a minimum density is required for condensation. Since the version of the Chipping model with symmetric hop rates does require a minimum density to condensate this would also be of interest for further understanding the importance of asymmetric dynamics.

An observation is that during the recurrence realisation of the Chipping model we observed a sharp front which propagates away from the origin when we are in the condensed regime. This is reminiscent of the active front we observed in the DACP. Additionally the probability of activity an infinite distance away from the origin in the DACP is very similar to the recurrence probability, the probability of observing a fully condensed system at infinity, of the Chipping model. Although the mechanics of the fronts are very different it might therefore be of interest to compare their dynamics.

Chapter 5

The Host-Solute-Vacancy model

As we saw in section 2.3 real-space condensation is a phenomenon whereby a finite fraction of a system's mass is concentrated within a microscopic volume. The basic mechanism underpinning real-space condensation is the arrival of mass into the condensed region more quickly that it can depart. The classical way for this to occur is by having the rate $u(k)$ at which a particle can leave a domain of size k be a sufficiently slowly decreasing function of k, as we saw for zero-range process (section 2.3.2). Alternatively if the condensate itself propagates then the rate $u(k)$ for low occupancies becomes important, as we saw for the Chipping model in the previous chapter. In this chapter we will encounter a third way in which condensation may occur by having the rates scale with system size such that the rates u are a function of k/N.

In this chapter I discuss a two-species driven-diffusive system which exhibits interesting condensation phenomena. In addition to undergoing an apparently discontinuous condensation transition the system also manifests structure within the condensate. We further observe that condensation appears to occur even in the low-density limit. As numerical studies of condensation are fraught with difficulties I introduce some new approaches for understanding the condensate. By a coarse-grained mapping to a zero-range process I find an effective hop rate which scales with system size. Upon examination of this hop rate we find that it displays a downwards step in the effective hop rate. This is consistent with the analysis of a zero-range process which, for hop rates with a step, displays a discontinuous condensation transition. This result however appears to conflict with our observation of low-density condensation.

5.1 Motivation

The model I study in this chapter is inspired by the phenomenon of electromigration in binary alloys, and in particular the two-dimensional model introduced by Dekker *et al.* [27]. The basic idea is that as an electric current is passed through a metallic crystal, atoms occasionally hop into vacant (defect) sites as a consequence of the applied driving force. This causes diffusion of the vacancies towards one end of the system, in turn leading to a breakdown of the structure once vacancies accumulate. It had been noted that this phenomenon was less pronounced in alloys [27]. Dekker *et al.* explained this observation in terms of a binding between vacancies and the solute atoms combined with a stronger driving force on the solute atoms. Vacancies that are bound to solute atoms are then dragged through the crystal opposite to their usual direction of motion, and at a rate faster than that of the host atoms. A reversal of the vacancy flux necessarily implies a corresponding reversal of the flux of both host and solute atoms. Hence this behaviour has been described as *reverse mass transport*. Here we attempt to study this phenomena by considering a reduction of the model described in [27] to a one-dimensional two-species driven-diffusive system, the Host-Solute-Vacancy model (HSV).

We observe that the HSV model undergoes a condensation transition into a phase where the condensate exhibits structure in that it appears to vary continuously between a 'solid' and a 'stripy' composition. To better understand the condensate we attempt a direct study of its properties through Monte Carlo simulation. In part this is achieved by introducing the *window scanner method*, a parameter-free approach for identifying the coexistence of high- and low-density regions. Through the direct methods we observe that not only does the condensation transition appear to be discontinuous but it also appears as though condensation is possible independently of the density of the condensing particles. This is in stark contrast to e.g. the ZRP where the transition is continuous and the density must be sufficiently large for condensation to be possible.

We therefore follow this by an indirect study of the condensation phenomena whereby an effective hop-rate function $u(k)$ is determined. By comparison with the condensation transition in ZRP, section 2.3.2, we find that the effective $u(k)$ decays *more quickly* than is normally allowed for condensation. Instead, as the system size N is increased, we find that the emergent $u(k)$ exhibits the scaling

form $u(k) = f(k/N)$. This then maintains the differential between the hop rates from domains of different sizes that is needed for condensation. As such condensation in the HSV model arises via a subtly different route to that observed in superficially similar models.

5.2 Microscopic model

In order to make contact with more fundamental non-equilibrium statistical mechanical studies of driven diffusive systems, and exclusion processes in particular, I study a reduction of the two-dimensional model of [27] to a single dimension. Each site of a periodic lattice of N sites may be occupied by one of two particle species, a *host* $(h, \circ)$ or *solute* atom $(s, \bullet)$, or it may be vacant $(v, \cdot)$. Both species are subject to driving forces, f_h and f_s respectively, in the same preferred direction and a hard-core exclusion constraint is imposed.

The hard-core exclusion constraint means hosts and solutes cannot pass each other on the lattice. We observe however that in two (or more) dimensions it is possible for a vacancy and a host particle, both in contact with the same solute particle, to exchange places without the solute-vacancy bond being broken. This process is shown in Fig. 5.1. To mimic this effect in 1D, and to allow the dynamics to be fully ergodic, a third type of move is added. Thus the basic dynamics are

$$\circ\cdot \underset{f_h^{-1}}{\overset{f_h}{\rightleftharpoons}} \cdot \circ \qquad \bullet\cdot \underset{f_s^{-1}}{\overset{f_s}{\rightleftharpoons}} \cdot \bullet \qquad \circ\bullet\cdot \underset{r/f_h^2}{\overset{f_h^2/r}{\rightleftharpoons}} \cdot \bullet\circ \tag{5.1}$$

As per the suggestion in [27] a binding energy between vacancy-solute pairs is also introduced. To reflect this all transition rates are multiplied by a factor $g^{\delta n_{sv}/2}$ where δn_{sv} is the change in the number of solute-vacancy pairs as a result of the transition. This corresponds to an interaction energy $\epsilon = \ln g$ per solute-vacancy pair (see section 5.4.3 below for elaboration on this point).

The rate of the third move in (5.1), hereafter the 2D-move, is purely phenomenological: since the host moves by two sites one expects the overall rate to be proportional to $f_h^{\pm 2}$. Throughout the rest of this work the constant of proportionality is taken to be $r = 1$.

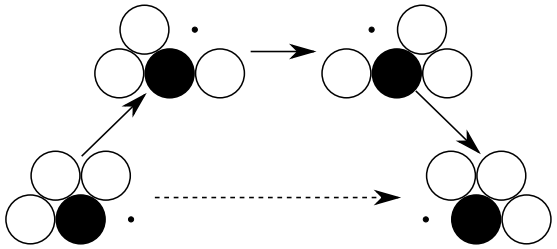

Figure 5.1: The 2D-move (solid arrows) and the introduced 1D equivalent (dashed arrow).

5.2.1 Relationship to other two-species models

By now, a wide variety of one-dimensional exclusion processes have been discussed in the literature, so it is worth setting out in broad terms how the HSV model, introduced here, relates to some prominent examples. Much more comprehensive surveys of these models can be found for example in [99, 34, 17].

In the absence of one of the two particle species (say the solutes) and the binding energy, the HSV model reduces to the asymmetric simple exclusion process (ASEP) on a ring. This model has the property that in the steady-state, all microscopic configurations are equally likely. More interesting steady-states arise in models that have open boundaries or additional particle species. It is the latter case we focus on here.

One important class of models has two particle species referred to as first- and second-class particles (denoted 1 and 2 respectively). These undergo the dynamics

$$10 \xrightarrow{1} 01 \qquad 20 \xrightarrow{\alpha} 02 \qquad 12 \xrightarrow{\beta} 21 \; . \tag{5.2}$$

When $\alpha = \beta = 1$, second-class particles behave as vacancies from the perspective of first-class particles, but as first-class particles from the perspective of vacancies. Hence second-class particles do not affect the dynamics of first-class particles and can be used as a tool to track density fluctuations and locate shock fronts, for example [2]. If $\alpha, \beta \neq 1$, second-class particles[1] do affect the first-class particles, and can induce transitions between phases with qualitatively distinct density profiles [80]. These phase transitions are related to those seen in the ASEP with open boundaries [100, 28].

A second important class of models, and one that is closely related to the

[1]Second-class particles are frequently referred to as defect particles in the case $\beta \neq 1$.

first, is obtained by viewing the three distinct lattice states 0, 1 and 2 as particles with negative, positive and neutral charge respectively[2]. One can then consider an external electric field biasing the charged particles in opposite directions, as first suggested in [97]. A key representative of this class is the AHR model [3, 4] which admits the three moves of (5.2) in addition to the reverse of the first. More precisely, the allowed updates are

$$+- \underset{q}{\overset{1}{\rightleftharpoons}} -+ \qquad 0- \xrightarrow{1} -0 \qquad +0 \xrightarrow{1} 0+ \ . \tag{5.3}$$

The system is found to become fully ordered for $q > 1$ and homogeneous for $q < 1$. Initial numerical investigations suggested a third mixed phase for $q_c < q < 1$. However, this was later argued via an exact solution [93, 95] to be a finite-size effect that persisted to anomalously large system sizes ($\sim 10^{70}$), the true thermodynamic regime being inaccessible by any simulation.

A complementary approach to understanding the mixed phase that leads to similar conclusions was followed in [64]. There, blocks of charged particles separated by vacancies (neutral particles) are regarded as a domain, and the rate at which a particle leaves a domain is estimated to yield an effective description of the dynamics in terms of a zero-range process (ZRP, see section 2.3.2). It was shown that over a certain range of q, the correlation length (typical domain size) grows to a large but finite value as a consequence of being close to (but not at) the condensation transition point in the ZRP. The reason for the anomalously large correlation lengths was attributed to the suppression of small domains [66]. The technique of reducing the dynamics to that of a ZRP has since been used to determine the presence or otherwise of condensation in a range of models [64, 35], and we shall use it for the HSV model in section 5.6.

The differences between the AHR model (or the ASEP with second-class particles) and the HSV model defined by (5.1) are (i) the dynamics exhibits partial asymmetry in all the transitions, not just the first of (5.3); (ii) an energetic interaction between solute-vacancy pairs; and (iii) the additional requirement for a vacancy to be present for a host and solute particle to exchange places.

In [35, 73], extensions of the AHR model to include energetic interactions

[2] In [3, 4] and subsequent works, the neutral particles are referred to as vacancies.

between charged particles were studied. Thus changing the first move in (5.3) to

$$+- \underset{q(1-\Delta H)}{\overset{1-\Delta H}{\rightleftharpoons}} -+ \quad \text{for} \quad H = \pm\frac{\epsilon}{4}\sum_i s_i s_{i+1} \tag{5.4}$$

with $0 \leq \epsilon < 1$ and $s = +1, -1$ or 0 for a positive, negative or neutral charge respectively. Again, by reduction to a ZRP, it has been argued that condensation occurs only at sufficiently large density and when the interaction is sufficiently strong and ferromagnetic (i.e., like charges attract) [35]. If the interaction is antiferromagnetic, an interaction strength that decreases with domain size is required for condensation to occur [73]. It should be noted that, unlike the case here, the binding energy in the HSV model is multiplicative with respect to the rates.

In the following we will argue that, for certain choices of model parameters, the HSV model condenses despite having an antiferromagnetic interaction that is independent of domain size. In addition we argue that the condensation is present even for small densities. This is in contrast to 'normal' condensation, such as in AHR, where condensation can only occur above a critical density. The foregoing discussion suggests that host-solute exchange being possible only in the presence of a vacancy is potentially responsible for this condensation, despite this being an apparently minor perturbation on the dynamics. Moreover, as we will show, the mechanism for condensation differs to that seen in [35, 73].

Although less similar overall there are a few more models worth mentioning in this context as they share certain aspects with the HSV model.

The two-lane model [70] introduces a different mechanism by which oppositely charged particles can move past each other. The model consists of two parallel one-dimensional periodic lattices with hop rates $\Gamma_\parallel$ within each lattice and $\Gamma_\perp$ between lattices. Thus the system reduces to two unconnected one dimensional lattices in the limit $\Gamma_\perp/\Gamma_\parallel \to 0$. The rules for the two-lane model are

$$\begin{array}{ccc} +0 \underset{0}{\overset{\Gamma_\parallel}{\rightleftharpoons}} 0+ & 0- \underset{0}{\overset{\Gamma_\parallel}{\rightleftharpoons}} -0 & +- \underset{0}{\overset{\gamma\Gamma_\parallel}{\rightleftharpoons}} -+ \\ 0 \overset{\Gamma_\perp}{\leftrightarrows} + & 0 \overset{\Gamma_\perp}{\leftrightarrows} - & - \overset{\gamma\Gamma_\perp}{\leftrightarrows} + \\ + \quad 0 & - \quad 0 & + \quad - \end{array} \tag{5.5}$$

with $\gamma < 1$. We observe that for $\gamma = 0$ oppositely charged particles may only pass each other via a neutral particle in the parallel lattice. This mechanism is

similar to the 2D-move in the HSV model in that it introduces a kinetic constraint whereby the neutral particle must be present for the $+-$ move to be possible. We note that although this model at first appear to show phase separation it was later shown [64] through a reduction to a ZRP to not phase separate in the thermodynamic limit.

Due to the binding energy we find that the hop rates in the HSV model effectively depend on the species of both the nearest and next nearest neighbour[3]. It is therefore worth considering the KLS model [67] which, although it is a one species exclusion process, is of interest since it considers hop rates which depends on the nearest and second nearest neighbour. Thus the rules for the model are

$$1011 \xrightarrow{\alpha_1} 1101 \qquad 1010 \xrightarrow{\alpha_2} 1100 \qquad 0010 \xrightarrow{\alpha_3} 0100 \qquad 0011 \xrightarrow{\alpha_4} 0101\,. \tag{5.6}$$

It is an interesting model since in the case where $\alpha_2 = e^{\beta}\alpha_4$ and $\alpha_2+\alpha_4 = \alpha_1+\alpha_3$ holds [72] then the steady-state can be written in a way which allows a mapping to the Misanthrope process. The Misanthrope process [24] is an extension of the ZRP whereby hop rates now depend on both departure and target site $u(n_l, n_{l+1})$. Depending on the choice of rates it, similarly to the ZRP, has a factorised steady-state.

5.3 Basic phenomenology of the HSV model

We begin our investigation of the HSV model by establishing its phenomenology in different parameter regimes. Our primary tool for this investigation is a continuous-time Monte Carlo simulation, as described in section 2.4. However the simulations used for the HSV model contained a few special features which I outline below before turning to the results.

5.3.1 Simulation details

In section 2.4 we saw that for a continuous-time Monte Carlo simulation employing the Next Reaction Method one keeps track of the set of all possible events, ε, that may change the state of the lattice. Based on the rate of each event E a time $t(E)$ at which the event will occur is then calculated. We note

[3]For the 2D-move we need to consider the third nearest neighbour as well.

from the dynamics (5.1) however that all moves involve a vacancy moving by one or two lattice sites in either direction. Therefore, it is straightforward to maintain a list of events, $\epsilon(v_i) \subset \varepsilon$, associated with each vacancy, v_i, based on the state of the neighbouring sites.

If any event in $\epsilon(v_i)$ occurs this requires a new time $t(E)$ to be calculated for each $E \in \epsilon(v_i)$. It is therefore more efficient to associate a time $t(v_i)$ with each vacancy, at which it will be involved in an event. This time is calculated based on the total rate of all associated events $\epsilon(v_i)$. Once $t(v_i)$ occurs an event in $\epsilon(v_i)$ is selected at random, weighted by the rate of each associated event, and performed. Further efficiency gains are obtained by making use of the fact that when a vacancy moves, only those events involving vacancies within two sites of the vacancy's initial or final position need to be updated. We further note that since the Next Reaction Method is a rejection-free algorithm it is of particular benefit when the number of possible events that can occur is relatively small (i.e., when the density of vacancies is low).

5.3.2 Preliminary results

There is in principle a large parameter space to investigate, comprising the driving forces f_h and f_s, the binding strength g, the two particle densities ρ_h and ρ_s, not to mention the system size N (which we here take to mean the total number of particles *including* vacancies). To reduce the parameter space, we first choose the density of solutes and vacancies to coincide: this was suggested by the idea that solutes and vacancies may form bound pairs. Thus $\rho_h = 1 - 2\rho_s$. Again, the original motivation for the model suggested that the density of vacancies (and hence solutes) should be small, so we took $\rho_s = 0.1$. In preliminary simulations, we found the phenomenology to be relatively insensitive to f_h, and that differences due to variation of the remaining parameters, f_s and g, tended to be most pronounced when f_h was close to unity. Thus we set $f_h = 1.1$, and will mostly describe the effect of varying f_s and g in the following.

Absence of reverse mass transport...

The first question of interest was whether the one-dimensional HSV model exhibits the reverse mass transport that was observed in its two-dimensional counterpart [27]. Given that the bias, on the host particles, is towards the right

we therefore looked for a net current of host particles towards the left in the steady-state. Measuring the fraction of all host particle moves that are to the right we say reverse mass transport has been observed if this fraction is less than 0.5. Note that there is a slight subtlety in that the 2D-move, see (5.1), needs to be weighted by a factor of two since it causes the host to be moved two sites. A range of values of f_s and g (and, indeed, f_h) were investigated but reverse mass transport was not observed in any region of the parameter space. However, we did find evidence for condensation and what appears to be three distinct steady-states. We shall return to the question of condensation shortly.

In Fig. 5.2 we observe the fraction of moves to the right as it evolves over time in the three representative regions of the parameter space. In addition to the total ratio for the moving hosts we also show the individual ratios for the component moves, i.e. the 2D-move and the 'host move'.

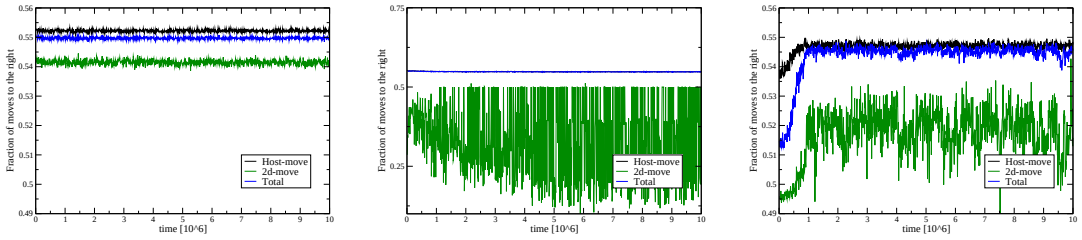

(a) $g = 2.0$, $f_s = 1.1$. (b) $g = 50.0$, $f_s = 20.0$. (c) $g = 200$, $f_s = 1.25$.

Figure 5.2: The fraction of rightward host particle moves over time in three systems of 1000 particles, $\rho_h = 0.8$ and $f_h = 1.1$, each in a different steady-state. Note that the line for the host-move and that for the total lie on top of each other in figure (b).

In the first state we observe that, on average, all moves are in the direction of the bias. In the second state there exists an element of reverse mass transport of host particles enabled by the 2D-move. For now we note that the 2D-move is so rare compared to the normal host-move that it has next to no effect on the overall host particle movement. Finally observing the third state we note that there is a transient element of reverse mass transport through the 2D-move. Again though this is too infrequent to lead to an overall, even transient, reverse mass transport.

Thus we conclude that we do not observe the, *a priori*, expected reverse mass transport. This either means that the 2D-move fails to capture some minor detail of the equivalent move in two dimensions or that reverse mass transport needs two or more dimensions to appear. We therefore shift our efforts to the observed

condensation transition instead.

. . . and presence of condensation

During the unfruitful search for reverse mass transport we found evidence for condensation into solute-rich regions at sufficiently large driving f_s and binding strength g. Closer inspection suggested the possibility of two different types of condensed region: one in which vacancies are not present in the solute-rich region, and one in which the solute particles and vacancies are intermingled. We refer to these structures as *solid* and *stripy* respectively.

More precisely, for systems with a small driving force ($f_s \lesssim 1.25$) and/or a small binding strength ($g \lesssim 2.0$) the system does not condense. As shown in Fig. 5.3a, we see a mixture of all three particle species, all three flowing freely through the system. At increased binding strength and driving force ($f_s \gtrsim 2.0$) the solutes make up a solid block, as shown in Fig. 5.3b. At intermediate driving ($1.25 \lesssim f_s \gtrsim 2.0$) one sees, above $g \gtrsim 25.0$, the stripy condensate shown in Fig. 5.3c. We remark that the superficially extreme value of $g = 200$ actually corresponds to a modest binding energy $\epsilon = \ln g \simeq 5.298\ldots$.

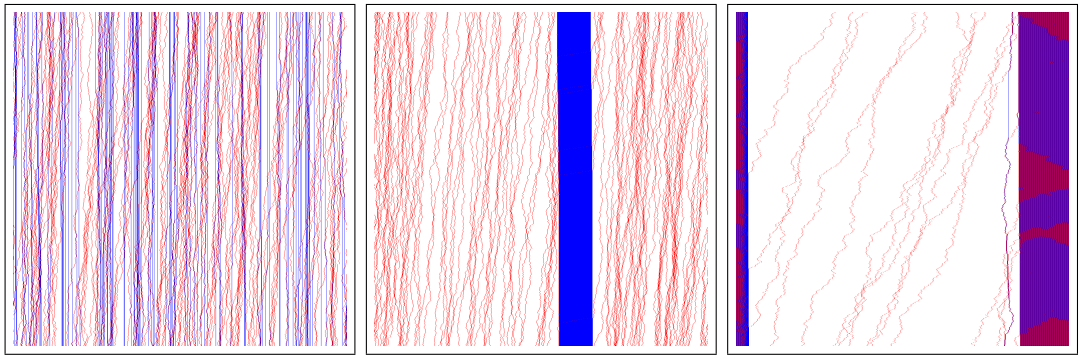

(a) $g = 2$, $f_s = 1.1$. (b) $g = 50$, $f_s = 20$. (c) $g = 200$, $f_s = 1.25$.

Figure 5.3: Three systems of 1000 particles with host density $\rho_h = 0.8$ at the end of a simulation, each at a different steady-state. Time increases as we move down the vertical axis. Red indicates vacancies, blue solutes and white host particles.

We now find that this behaviour explains the presence of a reverse mass transport component in Fig. 5.2b. The 2D-move is the only mechanism by which a host particle may move through the solid solute condensate. Thus, since the solutes experience a larger bias, this reverse transport component is in fact a

result of host particles being overtaken by a solid condensate of solutes.

The aim in the rest of this chapter is to establish whether the apparent condensation at large driving or binding is a true thermodynamic phase transition, and whether there is a sharp distinction between the solid and stripy condensates. We will look for direct evidence for a condensation transition by examining the behaviour of a range of macroscopic observables across the putative phase boundaries. We first consider the interaction energy of the system, which is proportional to the number of solute-vacancy pairs. This thus gives some measure of the 'stripiness' of the system, but does not necessarily distinguish between the cases where solutes are distributed across the entire system or condensed into a small region. The largest distance between two neighbouring solute particles, the gap size, gives a crude measure of condensation; more detailed information about the nature of a phase separation into two homogeneous domains is provided by a *window scanner method* that we introduce in section 5.5.2.

Before moving on to these measurements we will first consider the equilibrium case where we shall see that it is possible to compute the energy and the gap size exactly. This thus serves as a useful baseline to compare the driven system against.

5.4 Equilibrium analysis: The transfer-matrix method

A natural starting point for understanding the HSV model comes from looking at the equilibrium case when there is no driving, i.e. when $f_s = f_h = 1$. For this case it should be possible to find an exact solution using the transfer-matrix method. I will start this section by defining the transfer-matrix method and some of the techniques involved. Once this has been done we move on to the more involved task of applying it to the HSV model.

5.4.1 The transfer-matrix method

The transfer-matrix method (see e.g. [12] or [45]) is perhaps best known for being used by Onsager to find the exact solution of the 2D Ising model in 1944. It is a technique for solving equilibrium systems which have the property that they can

be broken down into a sequence of subsystems which only interact with adjacent subsystems. For a system of N such subsystems the grand canonical partition function becomes

$$\mathcal{Z}(N) = v_0 \left\{ \prod_{k=1}^{N} T_k \right\} v_{N+1} \ . \tag{5.7}$$

where v_0 and v_{N+1} are vectors associated with the ends of the sequence. T_k is the transfer-matrix which encodes the statistical weights of the different combination of states for subsystem $k-1$ being next to those for k. Thus the dimension of T_k is $p \times q$ where p (q) is the number of possible states of subsystem $k-1$ (k). For a cyclic system the expression simplifies further to

$$\mathcal{Z}(N) = \mathrm{tr} \left\{ \prod_{k=1}^{N} T_k \right\} \tag{5.8}$$

where the trace ensures that subsystems $k = 0, N$ are the same. For a homogeneous system the transfer-matrices are all the same, and thus square, and the partition function takes the simple form

$$\mathcal{Z}(N) = \mathrm{tr}\, T^N \ . \tag{5.9}$$

If T is known its eigenvalues $(\lambda_1, \lambda_2, \dots)$ and eigenvectors $(\vec{x_1}, \vec{x_2}, \dots)$ may be found. With these the matrix $P = (\vec{x_1}, \vec{x_2}, \dots)$ which diagonalises T may be constructed.

$$P^{-1} T P = \begin{pmatrix} \lambda_1 & 0 & \cdots \\ 0 & \lambda_2 & \cdots \\ \vdots & \vdots & \ddots \end{pmatrix} = W \tag{5.10}$$

where we assume that the eigenvalues are sorted by size s.t. $\lambda_1 \geq \lambda_2 \geq \dots$. Thus using the cyclic nature of the trace the partition function can be rewritten as

$$\mathcal{Z}(N) = \mathrm{tr}(W^N) = \lambda_1^N + \lambda_2^N + \cdots = \lambda_1^N \left(1 + \left(\frac{\lambda_2}{\lambda_1} \right)^N + \dots \right) \tag{5.11}$$

which for a non-degenerate largest eigenvalue simplifies further to

$$\mathcal{Z}(N) = \lambda_1^N + \mathcal{O}(1) \tag{5.12}$$

for large system sizes N.

The question about degeneracy is answered by appealing to the Perron-Frobenius theorem [90, 38] which states that if all the entries in T are positive then the largest eigenvalue is real and non-degenerate. We further note that if there is no eigenvalue degeneracy then by extension there can be no eigenvalue crossings and hence no phase transition in the system.

It should be noted that the Perron-Frobenius theorem additionally requires T to be finite dimensional. For a 1D system with a finite number of states this holds trivially. However in e.g. a 2D system we construct the transfer-matrix by having each row/column of T relate to a 1D chain of sites. As an example a periodic (toroidal) lattice with $n \times m$ sites, where each can be found in one of two states, can still be described by (5.9) such that $\mathcal{Z}(N) = \operatorname{tr} T^m$. The difference is that here T is a $2^n \times 2^n$ matrix [12, 45]. Thus in the thermodynamic limit where n (and m) $\to \infty$, T becomes infinite-dimensional and the Perron-Frobenius theorem no longer applies. This explains why—for systems with short-ranged interactions—equilibrium phase transitions are only possible in more than one dimension and then only in the thermodynamic limit.

Fugacity

Restrictions in the model due to e.g. conservation laws are encoded in the transfer-matrix through fugacity terms. Consider a homogeneous system where each subsystem can be in one of two states (a, b) and a conservation law requires that n_a of the N subsystems are in state a. For such a system the transfer-matrix becomes

$$T(z) = \begin{pmatrix} zw(a,a) & zw(a,b) \\ w(b,a) & w(b,b) \end{pmatrix} . \tag{5.13}$$

where $w(k-1,k)$ is the statistical weight and z is the fugacity variable associated with state a. Thus the partition function may be written in a second way

$$\begin{aligned} \mathcal{Z}(N,z) &= \operatorname{tr} T(z)^N \\ &= \sum_{n_a} z^{n_a} Z_N(n_a) . \end{aligned} \tag{5.14}$$

where $Z_N(n_a)$ is the canonical partition function for a system with exactly n_a of the N subsystems in state a. Note that n_b is indirectly defined through

$N = n_a + n_b$ which is why only one fugacity is needed.

At this point a solution with a known n_a may be sought in one of two ways. Either $\operatorname{tr} T^N$ is calculated explicitly and then expanded as a polynomial in z. $Z_N(n_a)$ is then given by the coefficients corresponding to the n_a-th power of z. This however requires calculating T^N explicitly which may not be possible for large N. An alternative approach is to seek an expression for z in terms of n_a instead. The average number of subsystems in state a in the grand canonical ensemble is found using the second expression in (5.14).

$$\begin{aligned} z\frac{\partial \ln \mathcal{Z}}{\partial z} &= \frac{z}{\mathcal{Z}} \sum_{n_a} n_a z^{n_a - 1} Z_N(n_a) \\ &= \frac{1}{\mathcal{Z}} \sum_{n_a} n_a z^{n_a} Z_N(n_a) = \langle n_a \rangle \ . \end{aligned} \tag{5.15}$$

This may then be inverted to give z as a function $z(\langle n_a \rangle, \mathcal{Z})$.

In the large system limit $N \to \infty$ we may instead consider the concentration of subsystems in the a state, $\rho_a = \lim_{N\to\infty} \langle n_a \rangle / N$. This may further be combined with the large system solution (5.12) for the partition function to give

$$\begin{aligned} \rho_a &= \lim_{N\to\infty} \frac{\langle n_a \rangle}{N} = \lim_{N\to\infty} \frac{z}{N} \frac{\partial \ln \mathcal{Z}}{\partial z} = \lim_{N\to\infty} \frac{z}{N} \frac{\partial}{\partial z} \ln\left(\lambda_1^N\right) \\ &= z\frac{\partial}{\partial z} \ln \lambda_1 \end{aligned} \tag{5.16}$$

where λ_1 is the largest of the eigenvalues. Thus if we know the concentration we can, in theory, invert (5.16) to find the fugacity coefficient $z = z(\rho_a, \lambda_1)$.

5.4.2 Transfer-matrix calculations applied to the HSV model

In the HSV model all interactions involve two nearest-neighbour sites. The subsystems can therefore clearly be identified with the homogeneous sites on the periodic lattice. The sites can be found in one of three states which we label h, s, v for occupied by host particles, solute particles or vacant respectively. The

transfer-matrix therefore becomes:

$$T = \begin{pmatrix} hh & hv & hs \\ vh & vv & vs \\ sh & sv & ss \end{pmatrix} = \begin{pmatrix} z & z & z \\ y & y & yg \\ 1 & g & 1 \end{pmatrix} , \tag{5.17}$$

Where z (y) is the fugacity variable which allows the number of host particles (vacancies) to be fixed and $g = \exp(-\beta\epsilon)$, with $\epsilon < 0$, is a measure of the binding energy (statistical weight) of a solute-vacancy pair.

However since the density of solutes and of vacancies are the same we find that for sufficiently large systems the exact transfer-matrix with two fugacity coefficients (5.17) can be replaced by one with only the fugacity coefficient related to the number of host particles, namely

$$T = \begin{pmatrix} hh & hv & hs \\ vh & vv & vs \\ sh & sv & ss \end{pmatrix} = \begin{pmatrix} z & z & z \\ 1 & 1 & g \\ 1 & g & 1 \end{pmatrix} . \tag{5.18}$$

The difference between the two forms for the transfer-matrix is that with two fugacities the number of particles of each species may be specified exactly (see below) whereas with only one fugacity only the number of host particles is exactly specified whereas the division of the remaining particles into solutes and vacancies will only be equal *on average*. As system size is increased we find that these fluctuations become negligible. Using only one fugacity allows us, as we shall see in the next section, to more easily get the fugacity z as a function $z(\rho_h, g)$. Small systems (less than $\sim$ 25 particles) can still be solved by explicitly expanding the two-fugacity partition function, using Maple, and identifying the correct coefficient as described in section 5.4.1.

Analysing (5.18) we find that the eigenvalues and eigenvectors of T are

$$\begin{aligned} \lambda_0 &= 1 - g , & \vec{x}_0 &= (0, -1, 1)^T , \\ \lambda_\pm &= \frac{z + g + 1 \pm \sqrt{B}}{2} , & \vec{x}_\pm &= \left(\frac{z - g - 1 \pm \sqrt{B}}{2}, 1, 1 \right)^T \end{aligned} \tag{5.19}$$

with $B = (z + g + 1)^2 + 4z(1 - g) = (g - z + 1)^2 + 8z$.

Since $g \geq 1$ and $z = \exp(\beta\mu) \geq 0$, where μ is the chemical potential, it

follows that $B > 0$ and thus that the largest eigenvalue is λ_+. To determine which eigenvalue has the largest magnitude however, we need to consider the case when $g \to \infty$. Rearranging the eigenvalues as

$$\begin{aligned} |\lambda_0| &= g - 1 \,, \\ |\lambda_\pm| &= \frac{z+g+1}{2} \left| 1 \pm \sqrt{1 + \frac{4z(1-g)}{(z+g+1)^2}} \right| \end{aligned} \tag{5.20}$$

shows that, for large g, $|\lambda_0|$ goes like g whereas $|\lambda_+|$ approaches g from above. The plot Fig. 5.4 verifies that $|\lambda_+|$ remains the larger eigenvalue. Thus we can safely relabel λ_+ as $\lambda_{\max}$ such that

$$\lambda_{\max} = \frac{z+g+1+\sqrt{B}}{2} \quad \text{with} \quad B = (z+g+1)^2 + 4z(1-g) \,. \tag{5.21}$$

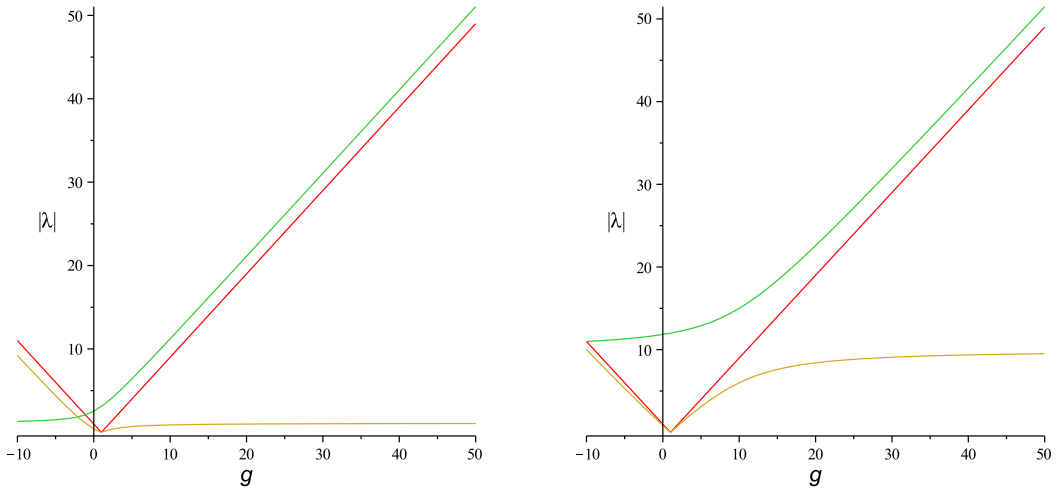

Figure 5.4: A plot of the magnitudes of the three eigenvalues against g. (a) For $z = 1.0$. (b) For $z = 10$. The colours labelling the eigenvalues are: red (λ_0), green (λ_+) and orange (λ_-).

Determining the fugacity coefficient

As described in the section on fugacities (section 5.4.1) the partition function can be decomposed into a sum which counts the number of particles of each species. This in turns allows us to relate the fugacity coefficient to the species densities. By remembering that z in the transfer-matrix (5.18) relates to the number of host

particles and identifying that g relates to the number of solute-vacancy bonds we can rewrite the partition function as

$$\mathcal{Z}(N) = \operatorname{tr} T^N = \sum_{n_h, n_{sv}} z^{n_h} g^{n_{sv}} \ . \tag{5.22}$$

This in turn allows us to use (5.16) to relate the partition function to the density of host particles, ρ_h, and the density of solute-vacancy bonds, ρ_{sv} through

$$\rho_h = z \left(\tfrac{\partial \ln \lambda_{\max}}{\partial z}\right)_g \ , \tag{5.23}$$

$$\rho_{sv} = g \left(\tfrac{\partial \ln \lambda_{\max}}{\partial g}\right)_z \ . \tag{5.24}$$

By inverting the expression for $\rho_h(z, g)$ an expression for the fugacity coefficient $z(\rho_h, g)$ can be obtained. Since we control the species densities, and g, this allows us to find an expression for $z(\rho_h, g)$ and thus $\lambda_{\max}$ for a given set of ρ_h and g. These can in turn be used to find the solution to systems which are too large for it to be plausible to calculate the partition function explicitly by multiplying N transfer-matrices together.

Inserting the expression for $\lambda_{\max}$, (5.21), into the equation for the density of host particles, (5.23), gives

$$\begin{aligned} \rho_h &= \frac{z}{\lambda_{\max}} \left(\frac{\partial \lambda_{\max}}{\partial z}\right)_g = \frac{z}{2\lambda_{\max}} \left(1 + \frac{1}{2\sqrt{B}} \frac{\partial B}{\partial z}\right) = \frac{z}{2\lambda_{\max}} \left(1 + \frac{z + 3 - g}{\sqrt{B}}\right) \\ &= \frac{z\left(\sqrt{B} + (z + g + 1) + 2(1 - g)\right)}{\sqrt{B}(g + z + 1 + \sqrt{B})} \ , \end{aligned} \tag{5.25}$$

with $B = (z + g + 1)^2 + 4z(1 - g)$. To invert this expression the $\sqrt{B}$ term is first isolated,

$$\sqrt{B} = \frac{z\left[(z + g + 1) + 2(1 - g)\right] - \rho B}{\rho(z + g + 1) - z} \ . \tag{5.26}$$

To improve legibility we will temporarily drop the h label from the ρ_h term. Squaring both sides and gathering the B terms then gives

$$\begin{aligned} B\left[\rho^2(z + g + 1)^2 + z^2 + 4z\rho(1 - g) - \rho^2 B\right] &= z^2\left[(z + g + 1) + 2(1 - g)\right]^2 \\ \Rightarrow \qquad zB\left[z + 4\rho(1 - g)(1 - \rho)\right] &= z^2\left[(z + g + 1) + 2(1 - g)\right]^2 \ , \end{aligned} \tag{5.27}$$

where the interior B term was expanded in the second line. From this we can identify that $z = 0$ is the first solution. This solution may be discarded since we observe, through the transition matrix (5.18), that it completely removes any host particles from the system. Considering only solutions which contain both particle species, $\rho \neq 1$ or 0, and with a non-zero binding energy, $g \neq 1$ we may expand the remaining B term and rearrange the expression further to get:

$$\begin{aligned}
& \rho(1-\rho)(1-g)\left[(z+g+1)^2+4z(1-g)\right] = 2z(1-g) \\
\underset{g\neq 1}{\Rightarrow} \quad & \rho(1-\rho)\left[z^2+2z\left(3-g-\frac{1}{\rho(1-\rho)}\right)+(g+1)^2\right] = 0 \\
\underset{\rho\neq 0,1}{\Rightarrow} \quad z &= \frac{1+\rho(1-\rho)(g-3) \pm \sqrt{\left[1+\rho(1-\rho)(g-3)\right]^2-\rho^2(1-\rho)^2(g+1)^2}}{\rho(1-\rho)} \\
\Rightarrow \quad z(\rho,g) &= \frac{1+\rho(1-\rho)(g-3) \pm (1-2\rho)\sqrt{1+2\rho(1-\rho)(g-1)}}{\rho(1-\rho)} \,.
\end{aligned} \tag{5.28}$$

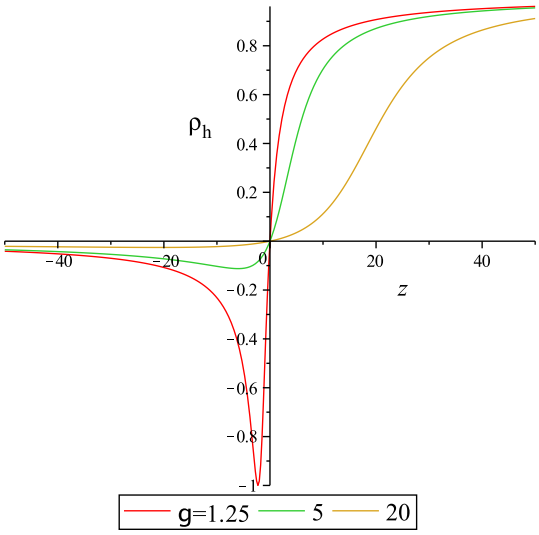

Figure 5.5: A plot of host density ρ_h against fugacity z for three different values of binding energy g. This shows that there is a unique solution in the physical regime $0 \leq \rho_h \leq 1$.

Plotting the density as a function of z (5.25) we observe, Fig. 5.5, that in the physical regime of interest $\rho_h \in (0, 1)$ there exists a unique solution. Substituting each of the two remaining solutions for the fugacity back into the expression for ρ_h (5.25) we test for self-consistency by plotting ρ against ρ_h for some arbitrary

$g > 0$. Thus we find that the solution with the negative square root is the one which correctly reflects the density behaviour. Thus the unique solution for the fugacity for $g > 0$ and $\rho_h \neq 1$ or 0 is

$$z(\rho_h, g) = \frac{1 + \rho_h(1-\rho_h)(g-3) - (1-2\rho_h)\sqrt{1 + 2\rho_h(1-\rho_h)(g-1)}}{\rho_h(1-\rho_h)} \,. \quad (5.29)$$

5.4.3 Interaction energy at equilibrium

Recall from the definition of the HSV model that the transition rates in (5.1) are multiplied by a factor $g^{\delta n_{sv}}$ where δn_{sv} is the change in the number of solute-vacancy pairs due to the transition. In the absence of a driving force, i.e. $f_h = f_s = 1$, the dynamics satisfy detailed balance with respect to the stationary distribution

$$P(\mathcal{C}) \propto g^{n_{sv}(\mathcal{C})} \,. \quad (5.30)$$

We can thus identify the interaction energy of a configuration $\mathcal{C}$ as

$$E(\mathcal{C}) = -n_{sv}(\mathcal{C}) \ln g \,, \quad (5.31)$$

by comparison with the Boltzmann distribution (taking inverse temperature $\beta = 1$). Thus expressing (5.31) in terms of density we find that the average energy per site is

$$\frac{E}{N} = -\ln g \cdot \rho_{sv}(g, z[\rho_h, g]) \,. \quad (5.32)$$

From (5.24) we know that we can get ρ_{sv}, the density of solute-vacancy bonds, through

$$\rho_{sv} = g\left(\frac{\partial \ln \lambda_{\max}}{\partial g}\right)_z = \frac{g\left(\sqrt{B} + g - z + 1\right)}{\sqrt{B}\left(z + g + 1 + \sqrt{B}\right)} \quad (5.33)$$

where, as before, $B = (z+g+1)^2 + 4z(1-g)$ and the z subscript on the partial derivative is there to remind us to keep the fugacity coefficient constant (i.e. disregard its g dependence) during the differentiation. Combining the two expressions above thus allows the average energy at equilibrium, shown as the solid line in Fig. 5.7, to be calculated.

At this point it is worth making the observation that there is a lower limit to E/N determined by the physical upper limit to ρ_{sv}. The maximum bond

configuration occurs when the solute and vacancy particles are arranged so that they alternate along the lattice. It therefore follows that $n_{sv} \leq 2n_s - 1$ where n_s is the number of solute particles. Thus we find that $\rho_{sv} < 2\rho_s = 1 - \rho_h$.

5.4.4 Gap size at equilibrium

As mentioned in section 5.3.2 a crude but easily accessible measure of condensation is to find the gap size, the largest distance between two consecutive solute particles. By the Perron-Frobenius theorem and the expression for the transfer-matrix (5.18) we already know that the equilibrium case will not display a condensation transition. Nevertheless explicitly finding the gap size for the equilibrium case is useful since it shows that there is some clustering even in the equilibrium. In the subsequent out-of-equilibrium calculations (section 5.5.2) we will be looking for further clustering introduced by the drive.

We find the gap size by considering the probability $P(n)$ that given a solute at site i the next solute is at site $i + n$. That is the probability that we find the lattice in the configuration

$$\overbrace{xs\underbrace{\tilde{x}\tilde{x}\ldots\tilde{x}\tilde{x}}_{n}sxx\ldots x}^{} \tag{5.34}$$

where s indicates the site is occupied by a solute, x that it may be occupied by any species (or a vacancy) and $\tilde{x}$ that it is not occupied by a solute. The first and last x have been connected to indicate that they denote the same site. The probability is then calculated by considering $\mathcal{Z} = \operatorname{tr} T^N$ which for the above configuration gives

$$\mathcal{Z}(n) = \operatorname{tr}\left[S_L \tilde{T}^{n-2} S_R T^{N-n-2}\right] \quad \text{for} \quad 2 \leq n < N-1 \tag{5.35}$$

where $\tilde{T}$ is the transfer-matrix for two $\tilde{x}$ and S_L (S_R) is the three site equivalent for $xs\tilde{x}$ ($\tilde{x}sx$). The expressions for $\mathcal{Z}(n)$ with $n \in \{1, 2, N-1, N\}$ are found in a similar fashion. The calculations for $P(n)$ are quite involved, we therefore content ourselves by simply stating the result here. The full calculations may be found in appendix B.1. From the calculations detailed there we find that the

probability of a gap of size n is

$$P(n) = \begin{cases} \dfrac{Aa(n)}{\lambda_{\max}^n} \dfrac{M_+ + M_- \left(\frac{\lambda_-}{\lambda_{\max}}\right)^{N-n-2} + M_0 \left(\frac{\lambda_0}{\lambda_{\max}}\right)^{N-n-2}}{M_+ + M_- \left(\frac{\lambda_-}{\lambda_{\max}}\right)^{N-2} + M_0 \left(\frac{\lambda_0}{\lambda_{\max}}\right)^{N-2}} & \text{for } n < n_{\max}, \quad (5.36) \\ \dfrac{Aa(n_{\max})\lambda_{\max}^{2-N}}{M_+ + M_- \left(\frac{\lambda_-}{\lambda_{\max}}\right)^{N-2} + M_0 \left(\frac{\lambda_0}{\lambda_{\max}}\right)^{N-2}} & \text{for } n = n_{\max}, \quad (5.37) \end{cases}$$

where $n_{\max} = N\left(\frac{1+\rho_h}{2}\right) + 1$ gives the maximum physical gap size for a given host density and lattice size. The λ's are the eigenvalues of T defined in (5.19), A is a normalisation factor defined through $\sum_{n=1}^{n_{\max}} P(n) = 1$ and the M's are the diagonal entries of the matrix in (B.17), namely

$$\begin{aligned} M_\pm =& \pm \frac{(z+g+1+\sqrt{B})(3z - zg + (g+1)^2 \pm (g+1)\sqrt{B})}{8\sqrt{B}} \\ M_0 =& \frac{(g-1)^2}{2} \, . \end{aligned} \tag{5.38}$$

Finally $a(n)$ is a function given by

$$a(n) = \begin{cases} (z+g)^2(z+1)^{n-3} & \text{for } \; n > 2 \, , \\ (z+g^2) & \text{for } \; n = 2 \, , \\ 1 & \text{for } \; n = 1 \, . \end{cases} \tag{5.39}$$

In the thermodynamic limit the probability simplifies significantly to

$$\lim_{N\to\infty} P(n) = Aa(n)\lambda_{\max}^{-n} \;\text{ for }\; n < n_{\max} \, . \tag{5.40}$$

Now we return to the gap size measure which we defined as the largest distance between any two consecutive solutes, $D_{\max}$. As we shall see later in this chapter this can easily be measured for any given instance of a finite system. We can relate this measure to the probability distribution $P(n)$ by letting $D_{\max}$ be the largest n for which $P(n) > 1/N$ where N is the system size. Note that the gap size measure is not the same as $P(n_{\max})$ which is the probability that the gap size takes on the largest physically allowed value of n. We shall return to the gap size measure in the context of out-of-equilibrium simulations in section 5.5.2. For

now we confirm that for a large system size ($N = 1000$) the calculated probability distribution $P(n)$ agrees with simulation results, Fig. 5.6. As expected we do not observe a condensate.

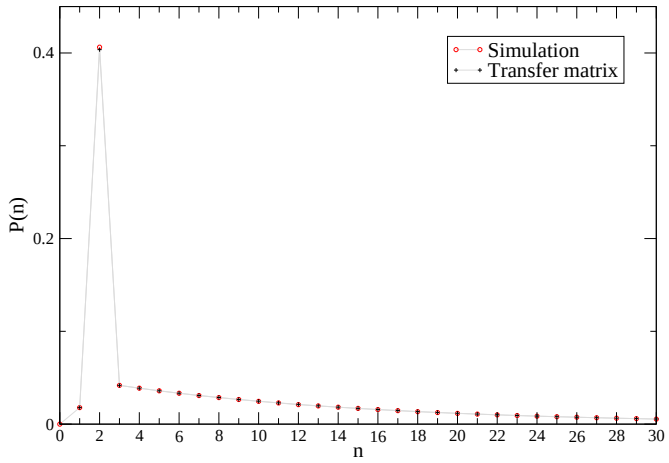

Figure 5.6: The probability distribution for the distance between solutes. The plot compares the values from a transfer-matrix calculation with those from simulation. Here shown for a system with 1000 sites at equilibrium with $g = 35$.

5.5 Out of equilibrium

The equilibrium case proved useful for finding exact results which may be used as a baseline for a general study of the HSV model. We return to the non-equilibrium case by reinstating the driving force $f_h = 1.1$. We can now use simulations to study the system for a range of g and f_s. We will start by looking at the interaction energy before moving on to the gap size and introducing the window scanner method.

5.5.1 Interaction energy

We recall from (5.31) that the interaction energy of a configuration $\mathcal{C}$ is

$$E(\mathcal{C}) = -n_{sv}(\mathcal{C}) \ln g \, . \tag{5.41}$$

Thus we can count the number of solute-vacancy pairs during a simulation to obtain the average energy in the steady-state, $\bar{E}$, as a function of the binding

strength g and for a range of f_s. These data are shown in Fig. 5.7. Since it is sometimes the case that the relaxation time can be rather large, we run two different initial conditions (spatially homogeneous, and a single solid block of solute particles) and check that the measured quantities are consistent with each other. We confirm that simulations recover the equilibrium result found in section 5.4.3 (solid line).

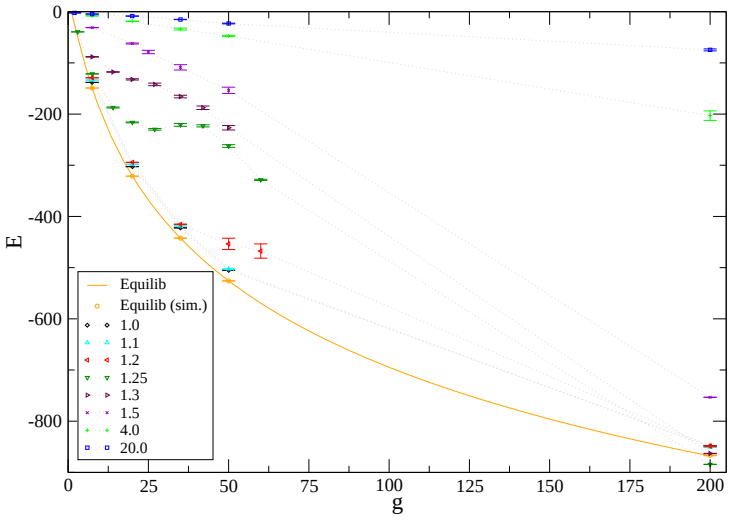

Figure 5.7: Energy against g for different values of f_s on a lattice with $N = 1000$, $\rho_h = 0.8$ and run for 10^7 time units.

The plot shows that when the driving force f_s is sufficiently large, the energy deviates strongly from the equilibrium curve, being much higher (closer to zero) at low binding strengths g. Thus in this regime, solute-vacancy pairs that may be present at equilibrium are broken apart by the application of a driving force. As the driving force is increased, a larger g is required for solute-vacancy pairs to reform. We observe that in the intermediate range of driving strengths $1.2 \lesssim f_s \lesssim 1.5$, there is a large increase in the number of solute-vacancy pairs as g is increased. In fact, there are cases where, at large g, the energy drops below its equilibrium value.

These measurements suggest a, possibly sudden, increase in stripiness at intermediate driving strengths at sufficiently large binding. Whether the stripes are confined to a condensed region, or distributed throughout the system cannot be discerned from an energy measure alone. However, our preliminary observations of the system suggest that the density of solute-vacancy pairs is high

in the fluid regime, and so we view a high energy (relative to the equilibrium case) as evidence for the presence of a solid region formed of solute particles alone.

5.5.2 Measures of condensation

In the context of the HSV model, condensation is manifested as a phase separation into a single dense region of solute particles whose size is extensive in the system size N. The situation is slightly complicated by the fact that vacancies may be present within the solute-rich region. We will introduce two different measures of condensation, the gap size and the window scanner method.

The gap size

A simple way to detect a solute-rich region, whether it contains vacancies or not, is to examine the maximum distance between any neighbouring pair of solute particles, $D_{\max}$. A large $D_{\max}$ implies that all the solute particles are confined within some small part of the lattice.

We show in Fig. 5.8a how $D_{\max}$ varies with f_s. It is immediately apparent that there is a sudden increase in $D_{\max}$ at $f_s \simeq 1.2$. The effect is most pronounced for large g, and disappears at around $g \simeq 2$. This corresponds to the parameter regime where we observe strong deviations from the equilibrium energy function in Fig. 5.7. This suggests there may be a transition into a condensed phase at $f_s \simeq 1.2$ at sufficiently large g. At very large g, and intermediate f_s, the decrease in the energy evident from Fig. 5.7 suggests a solute-rich region in which many vacancies are present.

The key question is whether the solute-rich region is a condensate, i.e., extensive in the system size N. It turns out that this question is not easily answered by inspection of $D_{\max}$. This quantity is extensive in N if *all* the solute particles remain confined in some region of the lattice. If a finite fraction of the solute particles form a condensate, $D_{\max}$ instead saturates at some finite value as $N \to \infty$, just as it does when no condensate is present. When we examine the behaviour of $D_{\max}$ in the thermodynamic limit (data not shown), we find that it does not scale linearly with N; however, this is insufficient to rule out the presence of a condensate.

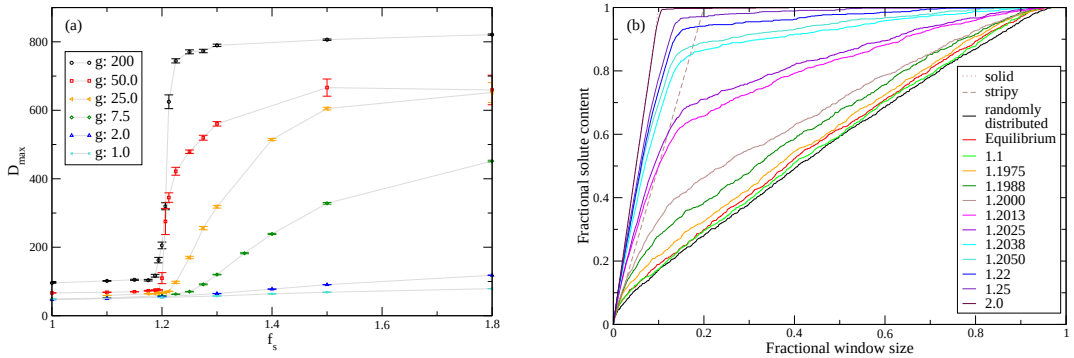

Figure 5.8: The two condensation measures, both for a system with $N = 1000$, $\rho_h = 0.8$ and averaged over 10 runs each for 10^7 time units. (a) Maximum gap size: $D_{\max}$ against f_s for six different values of g. (b) The window scanner method: Maximum fraction of the solutes found in a window against fractional window size. For a system at $g = 50$ started from the random initial condition.

The window scanner method

To better understand the structure in the steady-state of the HSV model, we devised a general approach for identifying coexisting high- and low-density regions that we dub the *window scanner method*. The idea of the window scanner is to construct a window of ℓ contiguous sites and put it on the lattice at the location that maximises the number of solute particles contained within it. This maximal number of solutes, m, is then plotted as a function of ℓ. If the system has phase separated into high- and low-density regions of solute particles with densities $\rho_{s,h}$ and $\rho_{s,\ell}$ respectively, then for ℓ up to the size ℓ_h of the high-density region $m \simeq \rho_{s,h}\ell$, and for $\ell > \ell_h$ we will have $m \simeq \rho_{s,h}\ell_h + \rho_{s,\ell}(\ell - \ell_h)$. In other words, one expects a piecewise linear function $m(\ell)$ with a dogleg at the size of the high-density region, and gradients corresponding to the densities of the different regions. An important property of the window-scanner method is that it does not invoke any *ad hoc* definition of what type of object is a candidate for the largest domain in the system. In contrast the naive approach of defining a condensate to be a consecutive sequence of at least x particles would make it appear that the condensation transition is discontinuous as the size of the condensate is continuously decreased below x. Similarly a single defect in the middle of a condensate smaller than $2x$ would make it appear as though there was no condensate present. These apparent effects are similar to the one we

observed for the DACP in chapter 3 where the decaying envelope made it appear as though the velocity was discontinuous.

The results from the window scanner for the case $g = 50$ are shown in Fig. 5.8b. The dogleg that indicates phase separation is clearly visible at larger driving strengths, with a largest domain size that is close to its maximum value of $\ell_h/N = \rho_s$. The increase in the gradient of $m(\ell)$ at small ℓ reflects increasing purity of the solute-rich region. At lower driving strengths, $m(\ell)$ is roughly linear, as in the case of a spatially homogeneous distribution of particles (shown for comparison). These data are suggestive of an onset of phase separation at $f_s \simeq 1.2$ (consistent with the sudden increase in $D_{\max}$), where the high-density phase comprises a mixture of different particle species, but becoming increasing solute-rich as the driving strength f_s is increased.

Unfortunately, the window scanner method did not help us resolve the question of whether the size of condensed region is proportional to system size in the thermodynamic limit. The basic difficulty is that the values of f_s and g at which phase separation appeared seemed to depend on system size, and so it was not clear to what extent doglegs for different system sizes were directly comparable. We found a closer examination of the *dynamics* of the process much more revealing in this regard, as will be explained in section 5.6 below.

5.5.3 Condensation in the zero-density limit

Traditionally condensation only occurs in a system when it is above some critical density. However as we observed for the Chipping model (section 4.4.1) this may not always be the case. We will therefore apply the gap size and the window scanner measures to investigate how the condensation transition of the HSV model is affected by changes in the solute (and thus vacancy) density. The solute density may be varied by either changing the number of solute particles (N_s) whilst keeping the number of host particles (N_h) constant or by changing N_h and keeping N_s constant, either case also resulting in a changed system size. For the gap size measure the first approach is the more appropriate since the gap size scales with the number of host particles. It was found that for densities down to $\rho_s = 0.026$ (below which no clean data could be acquired) the rapid increase in gap size at $f_s \sim 1.2$ was maintained, Fig. 5.9a. It should be noted however that the transition seems to shift to larger driving f_s for the lowest densities.

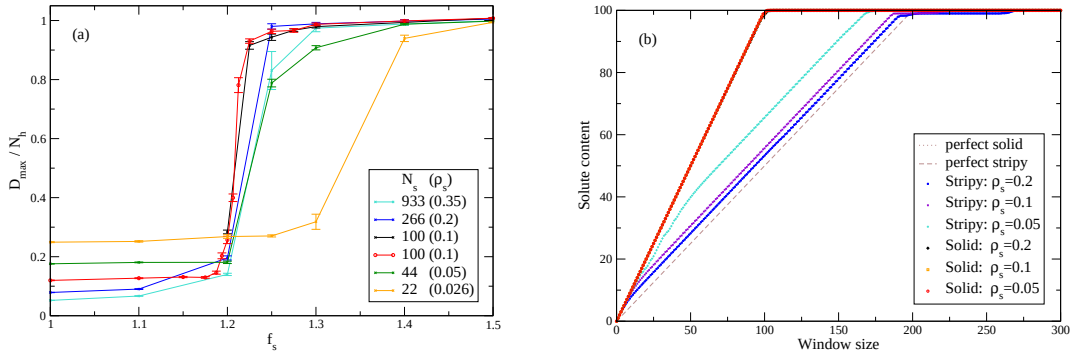

Figure 5.9: The condensation transition for varying densities. (a) Maximum gap size: $D_{\max}/N_h$ against f_s for six different values of N_s, all at $g = 200$ and $N_h = 800$. (b) Window scanner for the solid and the stripy phase at various densities. Solid at $f_s = 20.0$, stripy at $f_s = 1.25$, both for $g = 200$ with $N_s = 100$. Note that the 'perfect solid' line is largely covered by the data points for the solid phases.

For the window scanner measure varying N_h is the more appropriate approach. We use this measure to study the effect of a changing density for both a solid and a stripy condensate (both at $g = 200$ with $f_s = 20.0$ and 1.25 respectively). We observe that the solid condensate is completely unaffected by lowering the density, down to $\rho_s = 0.05$, whereas the stripy condensate appears to turn more solid as ρ_s is decreased (it still condenses though), see Fig. 5.9b. This is a strong indication that the HSV model either undergoes a condensation even in the zero-density limit or that the critical density above which condensation occurs is anomalously low.

5.5.4 Schematic phase diagram

To summarise, we have so far established that a solute-rich region forms when both the driving force f_s and interaction strength g are sufficiently large. At some fixed g, we find that when condensate first appears, it is stripy (i.e., contains vacancies); these vacancies are driven out as the driving force f_s is increased. This leads us to tentatively propose the schematic phase diagram for the system, shown in Fig. 5.10.

We emphasise that this phase diagram is speculative. What remains to be shown is whether the system condenses into a single solute-rich region, or whether the size of the solute-rich domains saturates at some finite value in the

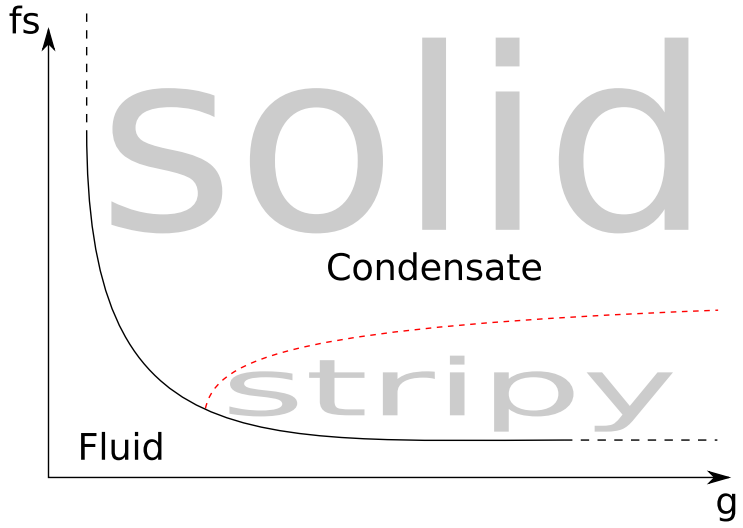

Figure 5.10: The three regimes into which the steady-states fall. Note that the dashed line between the Solid and Stripy regimes indicates that this is not a sharp boundary. Rather the stripy condensate will gradually turn solid and above the dashed line we no longer observe any remains of the stripy regime. The dashed lines on either end of the fluid-condensate boundary indicate that is not known whether, as f_s (or g) go to infinity the boundary gets arbitrarily close to the axis or whether it remains at a fixed value.

thermodynamic limit. It is further unclear whether the solid and stripy structures are distinct phases or just different points on a continuum. The location of the phase boundary as g or f_s approach infinity is also unclear: although numerical simulations for large g and f_s suggest that a non-zero binding energy (i.e., $g > 1$) and driving strength is required for condensation.

5.6 Effective description in terms of a zero-range process dynamics

We now attempt an indirect approach in order to sharpen the phase diagram and answer the question of whether the HSV model exhibits a condensation transition in the thermodynamic limit.

Constructing an *effective* description of the dynamics as a ZRP has proved a successful strategy for the analysis of condensation in more general driven-

diffusive systems, such as multi-species exclusion process [64, 66, 65, 35, 73]. A common situation is that simulations reveal the existence of large domains in finite systems, but it is unclear whether the domain is truly macroscopically large. A way to establish this is to determine an effective or empirical $u(k)$ for a domain of size k. As was shown earlier in this thesis (section 2.3.2) condensation in the thermodynamic limit then occurs, for a sufficiently high particle density, when the hop rate $u(k)$ decays with k to a constant value u_∞ more slowly than

$$u(k) = u_\infty \left(1 + \frac{2}{k}\right) \ . \tag{5.42}$$

Typically, these models feature energetic interactions between neighbouring particles, and an external drive that has a different strength and/or sign for different particle species. Periodic boundary conditions then admit a steady-state current of particles around the system as a consequence of the external drive. In many cases, simulations show the formation of large domains; however, empirical measurements of an effective $u(k)$ demonstrate that a truly macroscopic condensate is only present within more limited parameter regimes. Some model systems show rather extreme finite-size effects, in which the typical domain size saturates at $\sim 10^{70}$ lattice units [93] which, while inaccessibly large in both simulation and reality, is nevertheless a finite-size effect.

To exploit this condensation criterion in the context of a multi-species exclusion process, we map particles of one or more species in the exclusion process to particles in the ZRP, and the remaining particles (which may include vacancies) to *sites* in the ZRP[4]. Under this mapping, all the particles that sit between two sites are considered to occupy the site to the right. In [35], the AHR model with a ferromagnetic interaction (see section 5.2.1) was described in terms of a ZRP by mapping charged particles (the + and − species) to particles, and the neutral particles (0) to sites. In that work, effective rates $u(k)$ were measured by viewing a large system at any instant in time as comprising an *ensemble* of domains of different sizes, and then using the fraction of all domains of size k that decreased in size in one (discrete) timestep as an estimate of the transition rate $u(k)$. This estimate can be improved by averaging over multiple timesteps. By comparing this empirical function with (5.42), the AHR model was shown

[4]Note that this is a different mapping from that described in section 2.3.2 where particles in the exclusion process are mapped to sites in the ZRP.

to condense at sufficiently high densities when the ferromagnetic interaction was sufficiently strong [35].

Our aim is to apply a similar analysis to the HSV model. However, the approach of [35] cannot be used as it stands for a continuous-time process, because it relies on the existence of a well-defined discrete timestep. The first task therefore is to formulate an approach that can be applied to continuous-time processes.

5.6.1 Effective rates of a Poisson process under coarse-graining

The general problem we address is that of estimating the transition rates of a continuous-time stochastic process in which hops between configurations $\mathcal{C}$ and $\mathcal{C}'$ occur as a Poisson process from a specific realisation of the dynamics. Once a specific transition rate $\omega(\mathcal{C} \to \mathcal{C}')$ has been measured, one can then obtain transition rates for an effective process acting in a coarse-grained state space. We discuss these two steps in turn.

Measuring the rate of a Poisson process

Suppose we are presented with a realisation of a stochastic process in discrete space and continuous time beginning at time $t = 0$ and ending at time $t = \tau$. Three quantities that can be measured are: (i) $N_\tau(\mathcal{C})$, the total number of times configuration $\mathcal{C}$ is visited (i.e., either defined as the configuration being entered or exited); (ii) $N_\tau(\mathcal{C} \to \mathcal{C}')$, the total number of times a transition from configuration $\mathcal{C}$ to $\mathcal{C}'$ takes place; and (iii) $T_\tau(\mathcal{C})$ the total time spent configuration $\mathcal{C}$. Clearly these quantities will vary between realisations and the interval τ. However, in the limit $\tau \to \infty$ (and, assuming ergodicity), we have

$$\lim_{\tau\to\infty} \frac{N_\tau(\mathcal{C} \to \mathcal{C}')}{N_\tau(\mathcal{C})} = \frac{\omega(\mathcal{C} \to \mathcal{C}')}{r(\mathcal{C})} \tag{5.43}$$

for any trajectory through the configuration space. In this expression, $r(\mathcal{C})$ is the total rate at which configuration $\mathcal{C}$ is exited, i.e,

$$r(\mathcal{C}) = \sum_{\mathcal{C}'\neq\mathcal{C}} \omega(\mathcal{C} \to \mathcal{C}') \; . \tag{5.44}$$

The expression (5.43) comes about because the probability that the next transition out of configuration $\mathcal{C}$ is to the configuration $\mathcal{C}'$ is proportional to the corresponding transition rate.

Meanwhile, for large τ,

$$T_\tau(\mathcal{C}) \sim \frac{N_\tau(\mathcal{C})}{r(\mathcal{C})} \tag{5.45}$$

since the mean time spent in configuration $\mathcal{C}$ each time it is entered is $\frac{1}{r(\mathcal{C})}$. This is a simple consequence of the fact that the transition out of configuration $\mathcal{C}$ is a Poisson process with rate $r(\mathcal{C})$. Combining (5.43) and (5.45) we find that, formally,

$$\omega(\mathcal{C} \to \mathcal{C}') = \lim_{\tau\to\infty} \frac{N_\tau(\mathcal{C} \to \mathcal{C}')}{T_\tau(\mathcal{C})} \,. \tag{5.46}$$

We may therefore estimate the rate of *any* Poisson process $\omega(\mathcal{C} \to \mathcal{C}')$ by monitoring the number of times the transition is made and the total time spent in the starting configuration over a sufficiently long realisation of the stochastic dynamics.

Determining an effective dynamics by coarse-graining

We illustrate the idea of coarse-graining the dynamics to obtain an effective description with the explicit example of a reduction of a multi-species exclusion process to a ZRP. The first step is to decide what constitutes a domain of size k: for example, in the analysis of the ferromagnetic AHR model [35], this was taken to be a sequence of k charged particles (+ or − particles) between a pair of neutral particles (0). We now identify the set $\mathcal{A}_k$ of all ordered pairs of configurations $(\mathcal{C}, \mathcal{C}')$ such that the transition $\mathcal{C} \to \mathcal{C}'$ corresponds to a domain of size k shrinking to a domain of size $k-1$. The coarse-graining step is to assume that all such transitions can be represented as independent Poisson processes with common rate $u(k)$.

Thus, using (5.46), we have that for any $(\mathcal{C}, \mathcal{C}') \in \mathcal{A}_k$, $u(k)$ can be estimated from

$$u(k) \simeq \frac{N_\tau(\mathcal{C} \to \mathcal{C}')}{T_\tau(\mathcal{C})} \tag{5.47}$$

for sufficiently large τ. Then, by summing over all such pairs of configurations

we find

$$u(k) \sum_{(\mathcal{C},\mathcal{C}')\in\mathcal{A}_k} T_\tau(\mathcal{C}) \simeq \sum_{(\mathcal{C},\mathcal{C}')\in\mathcal{A}_k} N_\tau(\mathcal{C}\to\mathcal{C}') \; . \tag{5.48}$$

The sum on the right-hand side is simply the total number of times a domain of size k is observed to shrink to size $k-1$. After summing over the target configurations $\mathcal{C}'$, the sum on the left-hand side is then equal to the time spent in each configuration $\mathcal{C}$ multiplied by the number of domains of size k in $\mathcal{C}$. This is equivalent to the combined lifetime of *all* domains of size k that ever form in the time interval τ. Thus, we can express the estimate of $u(k)$ in words as

$$u(k) = \frac{\text{Number of observed transitions } k \to k-1}{\text{Combined lifetime of all domains of size } k \text{ ever formed}} \; . \tag{5.49}$$

As a check of this formula, we applied it first to a continuous-time zero-range process (simulated via the Next Reaction Method) to check that the measured $u(k)$ are numerically consistent with those used to define the transition rates. We further simulated the ferromagnetic AHR model in continuous time, Fig. 5.11, finding agreement with the results obtained using the distinct discrete-time approach of [35].

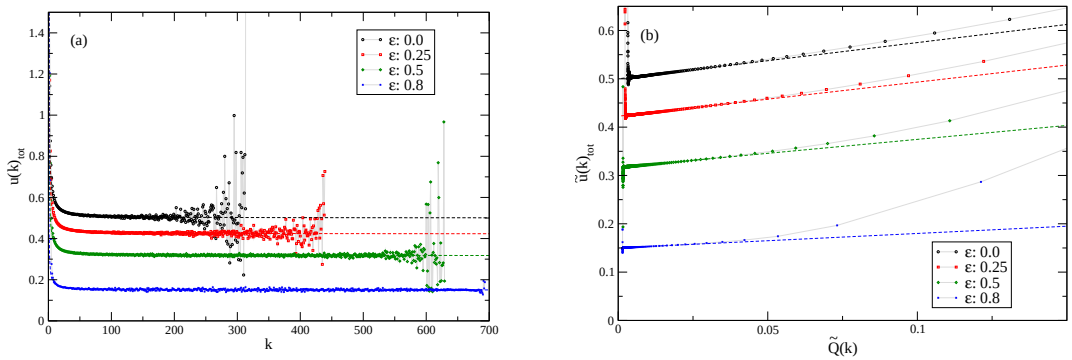

Figure 5.11: (a) Hop rate against occupation for the ferromagnetic AHR model at different binding energies ε. (b) The same but for the equivalent cumulative variables. In both cases the dashed lines indicates a rate of the form $u_\infty(1+b/k)$ using the parameters found in [35]. Here shown for a lattice with $L = 1000$ sites at a particle density $\rho = 0.35$ with an equal number particles of each species.

The test for condensation is then to compare the hop rates for large k against (5.42), a slower decay providing evidence for condensation. As is evident from Fig. 5.11a it is sometimes hard to discern the large-k behaviour of the empirical

$u(k)$. One may therefore, as in [35], transform to *cumulative* variables that make it easier to focus on the large-k tail and suppress the effects of noise in the tail to boot. To facilitate first define two intermediate variables

$$N_\tau(k) = \sum_{(\mathcal{C},\mathcal{C}')\in\mathcal{A}_k} T_\tau(\mathcal{C}) \quad , \quad F_\tau(k) = \sum_{(\mathcal{C},\mathcal{C}')\in\mathcal{A}_k} N_\tau(\mathcal{C}\to\mathcal{C}') \tag{5.50}$$

such that $u(k) = \lim_{\tau\to\infty} F_\tau(k)/N_\tau(k)$. The cumulative distributions are thus defined as

$$\tilde{N}(k) = \sum_{\ell=k}^{\infty} N(\ell) \quad , \quad \tilde{F}(k) = \sum_{\ell=k}^{\infty} F(\ell) \quad , \quad \tilde{Q}(k) = \tilde{N}(k)^{-1} \sum_{\ell=k}^{\infty} \frac{N(\ell)}{\ell} \ , \tag{5.51}$$

where the τ subscript has now been suppressed. Therefore the condensation criterion (5.42) becomes the linear function

$$\tilde{u}(\tilde{Q}) = \frac{\tilde{F}(k)}{\tilde{N}(k)} = u_\infty \left[1 + 2\tilde{Q}\right] \ . \tag{5.52}$$

Applying the cumulative approach to the ferromagnetic AHR model, Fig. 5.11b, we find very good agreement with the results obtained in [35].

Algorithmic approach using the Next Reaction Method

Since this approach has not appeared before I will here lay out the algorithm explicitly as it is applied to a general process simulated using the Next Reaction Method. We consider a one-dimensional periodic lattice occupied by particles which are allowed to hop to an unoccupied site directly to their right at some rate. Each site i has an assigned domain and an associated event time t_i. The event time gives the time at which a particle on the site will execute a hop, see section 2.4) for details. Thus if the site is unoccupied $t_i = \infty$. For each domain d a record of its current size k_d and the time elapsed since the size last changed τ_d is maintained. For every allowed domain size $k \leq N$ two further variables are maintained, $T(k)$ the cumulative lifetime and $F(k)$ the observed number of transitions $k \to k-1$. The algorithm thus goes as follows:

1. Initialise.

- Construct the lattice, calculating transition rates and event times for each site (as detailed in section 2.4).
- Label each domain by enumerating the unoccupied sites. All occupied sites in between are then assigned the same label as that of the first unoccupied site to their right. Thus the size of each domain equals the number of sites carrying the corresponding label, less one.

2. **Update.** For each update we keep a record of the size of both the origin and target domain before the update.
   - Add the time-since-update τ_d of each of these domains to the cumulative lifetime for that size.
   - Add one to $F(k)$ where k is the size of the originating domain.
   - Perform the event and update the domain labels and recalculate domain sizes.
   - Reset the time-since-update τ_d of the originating and target domains.
3. **Iterate.** Repeat step 2 for the desired time.
4. **Finalise.** For each domain add any non-zero time-since-updates τ_d to the appropriate cumulative lifetime $T(k_d)$. Thus, per (5.49), we have $u(k) = F(k)/T(k)$.

For a system with more then one allowed type of move one keeps track of the transitions $F_i(k)$ for each type thus giving a hop rate $u_i(k)$ for each. These may then be studied individually or by studying the total rate out of a domain of size k, $u_{tot}(k) = \sum_i u_i(k)$. It is this total rate which is shown in Fig. 5.11 above and in the results for the HSV model below.

5.6.2 Reduction to a ZRP for the HSV model

We now apply the procedure outlined above to reduce the HSV model to a zero-range process. We start by defining a domain as an uninterrupted sequence of solutes and vacancies. This means that we make no distinction between solid and stripy domains. Note that the 2D-move corresponds to changing the occupation of a site (i.e. the size of a domain) by two particles. Thus the definition for the

effective hop rates $u(k)$, obtained via equation (5.49), is modified so as to include both transitions $k \to k-1$ and $k \to k-2$. Empirical measurements of these effective hop rates $u(k)$ are shown in Fig. 5.12a for each of the solid, stripy and fluid regimes in addition to the equilibrium case.

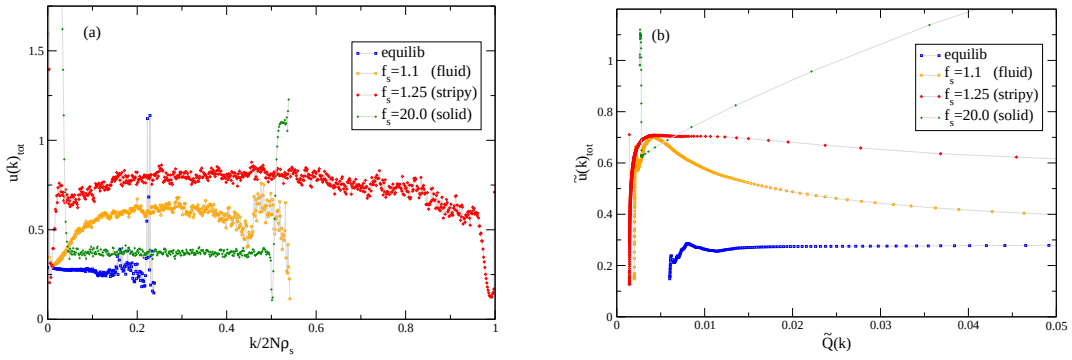

Figure 5.12: (a) Hop rate against occupancy for the HSV model for a system with $N = 1000$ sites and solute density $\rho_s = 0.35$, all at binding strength $g = 200.0$ but for different values of driving force f_s. (b) The same as (a) but for the equivalent cumulative variables. Both plots show all three phases in addition to the equilibrium case. The plotted rate is the total which includes hops in either direction and of either type.

In these simulations, an increased density of solutes and vacancies of $\rho_s = \rho_v = 0.35$ was used. The results are qualitatively the same as for lower densities (e.g. $\rho_s = \rho_v = 0.1$, as previously), but yield better statistics because more (and potentially larger) domains form when more particles are available.

Since it is hard to discern the large-k behaviour of the empirical $u(k)$ directly from Fig. 5.12a the equivalent cumulative variables are also investigated. Note that $\tilde{Q}(k) \to 0$ as $k \to \infty$, and so a linear approach of $\tilde{u}/u_\infty$ to the y-axis with a gradient $b > 2$ would suggest condensation. However, we do not find the expected linear behaviour (which we observed for ferromagnetic AHR in Fig. 5.11b) on applying this, as is evident from Fig. 5.12b. Instead we find that the hop rate decays more quickly than is normally allowed for condensation.

The key feature which we focus on is the dip followed by a spike in $u(k)$ at large k that is apparent from the solid and stripy condensates in Fig. 5.12a. In this figure, the domain size k has been normalised by the maximum possible size of a domain, $2N\rho_s$. Then, in the solid regime, for example, we see that the spike occurs at a normalised domain size of $\frac{1}{2}$, the maximum size of a domain that does not contain any vacancies. The spike would therefore seem to be a consequence

of the fact that, in a system of a finite size, there can only ever be a single domain larger than a certain size, which could lead to contributions to the hop rate $u(k)$ that go away in the thermodynamic limit.

In the intermediate-k regime, the functions $u(k)$ vary slowly before falling sharply as the spike is approached. It is not clear whether this sharp fall is also a finite-size effect. We therefore compare the hop rate as a function of *normalised* domain size at different system sizes N, looking to see which features (if any) appear retained over an extensive range of k in the thermodynamic limit. The data for the stripy phase are shown in Fig. 5.13. We see that the region over which there is a spike decreases as N increases (Fig. 5.13b), while the sharp fall in $u(k)$ before the onset of the spike follows some common master curve $f(k/N)$ for a range of different systems sizes N. We have also observed this scaling of the hop rates at other locations in the stripy phase, and at larger system sizes (although the noise in the latter is such that we do not show these data here).

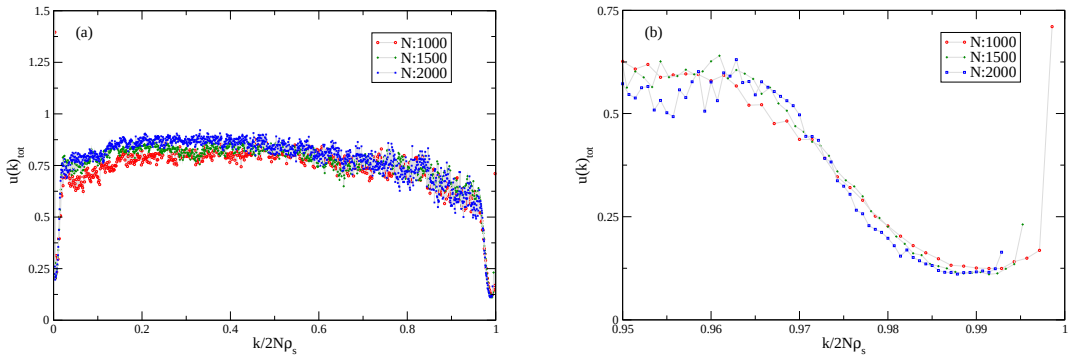

Figure 5.13: (a) Hop rates against the fractional occupancy, $k/2N\rho_s$, for systems of different sizes in the stripy phase ($g = 200.0$, $f_s = 1.25$). (b) A close-up on the tail of plot (a).

Before discussing the consequences of such a scaling form for the hop rates, we perform a corresponding analysis of the hop rates in the solid and fluid regimes. Again, we find that the hop rates are a function of k/N in the solid regime, albeit one where the spike also scales with the system size (Fig. 5.14a). By contrast we find that the hop rates do not scale with system size when in the fluid phase.

To understand why the spike is still present in the case of the solid condensate we recall that the domain is defined as an uninterrupted sequence of solutes *and vacancies*. Now observe that the spike occurs as the normalised domain size increases above $\frac{1}{2}$, that is at sizes where vacancies must also be included in the

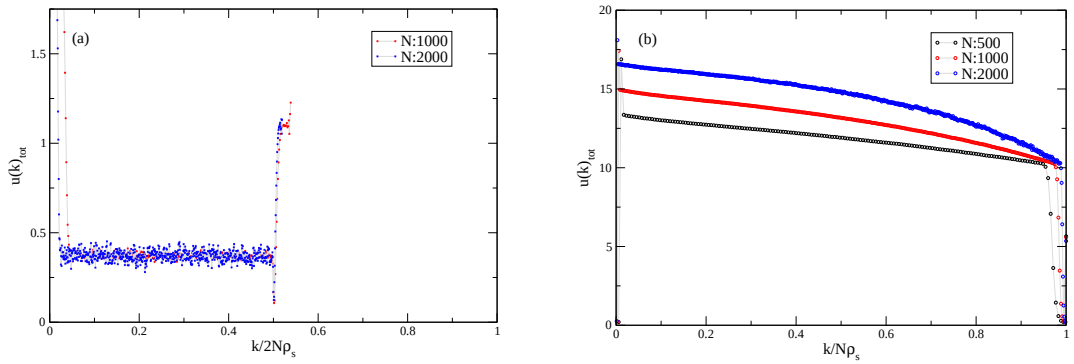

Figure 5.14: (a) Hop rates against the fractional occupancy for systems of different sizes in the solid phase ($g = 200.0$, $f_s = 20.0$). (b) Hop rates against fractional occupancy for systems of different sizes where a domain has been defined as solutes only.

condensate. We therefore consider a domain defined as an uninterrupted sequence of solutes only. The effective hop rates for this definition are shown in Fig. 5.14b, for different system sizes.

This shows us that there is a abrupt decline in the hop rates similar to that observed for the solute-vacancy domain in Fig. 5.13a for the stripy case. With the solute-only domain we do not observe the collapse of the hop rates to a function in k/N, as seen in Fig. 5.14a. It does however appear that the domain becomes fully saturated in the thermodynamic limit, i.e. the minima in the hop rate occurs at $k/N = \rho_s$. Thus the spike observed with a solute-vacancy domain is the result of vacancies 'contaminating' the solid condensate as they move through it.

It should be noted that for smaller values of f_s, but still in the solid condensate, the contaminating vacancies moves less rapidly through the condensate. As a result the crossover from the dip to the spike becomes blurred. Even for a solute-only definition of the domain the contamination drastically increases the noise levels, beyond usefulness, since each vacancy splits the domain into two parts.

Based on the above observations I therefore suggest that the solid phase is but a special instance of the stripy one. This is further supported by observing that the transition from stripy to solid, visually, takes the form of the stripy condensate gradually turning solid from the right hand side, see Fig. 5.15a. If we observe the effective hop rates Fig. 5.15b we see that going from stripy to solid shifts the dip to the left, towards that of the solid case. A collapse is still obtained for different system sizes (not shown).

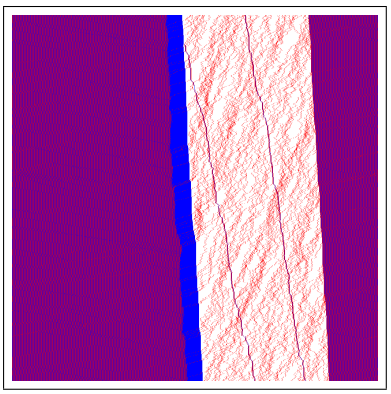

(a) $g = 200$, $f_s = 2.0$.

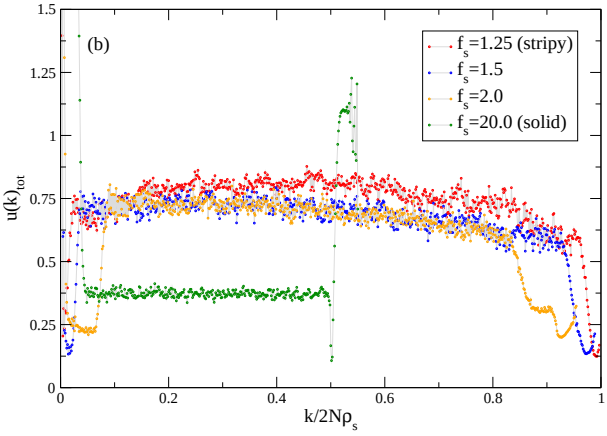

Figure 5.15: Illustrations of the stripy-solid in-between case, all for $\rho_s = 0.35$, $N = 1000$, $g = 200$. (a) A screenshot for the case $f_s = 2.0$. Note the solid regime invading the stripy one from the right. (b) Hop rates against fractional occupancy for several such in-between cases.

5.6.3 Consequences of a scaling form for the hop rates

Through the reduction of the HSV model to a ZRP we saw that the condensation mechanism is distinctly different from that of the ZRP. Firstly we observe that we do not get the expected form for the decay of the hop rate with occupancy, which would have given linear behaviour in Fig. 5.12b. Secondly we find that, in the condensed phase, the hop rate takes on the scaling form $u(k) = f(k/N)$. Thus we need a new mechanism for explaining the condensation behaviour.

Looking at the front of the hop rates in the solid and stripy phase we suggest that, for large k, the hop rates can be described by a step function whereby the rate takes a constant value c_0 at occupancies less than some cut-off value $k^*(N)$ and a different value $c_1 < c_0$ for occupancies above said value,

$$u(k) = \begin{cases} c_0 & \text{for } k \leq k^* \,, \\ c_1 & \text{for } k > k^* \,, \end{cases} \tag{5.53}$$

for $k \gg 1$. See Fig. 5.16 for an illustration. For the parameters $g = 200$, $f_s = 1.25$, shown in Fig. 5.12a, these values would be $c_0 \simeq 0.6$, $c_1 \simeq 0.11$ and $k^* \simeq 0.965(1 - \rho_h)N$.

The consequences of the hop rates being described by such a step function are twofold. Firstly in [33] a ZRP with a hop rate represented by a (downwards) step function (5.53) was investigated. It was shown that a true condensation

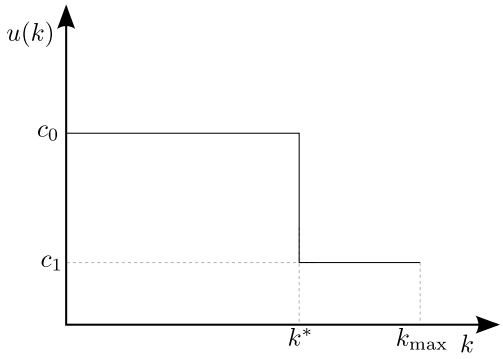

Figure 5.16: An illustration of the hop rate in equation (5.53). The step in the rate occurs at k^*. The rates are only defined up to the largest allowed domain size i.e. $k_{\max} = (1 - \rho_h)N$.

transition is only present if k^* is a function of the system size such that k^* tends to infinity in the thermodynamic limit. The calculations for this are presented in appendix B.2. Since the hop rate of the HSV model scales with system size it fulfils this requirement. Secondly in [49], motivated by studies in granular media, it was shown that such a phase transition is discontinuous. This would in turn be in agreement with the rapid increase in gap size observed in Fig. 5.8a.

However in [49] we find that condensation only occurs for systems above some non-zero critical density (see below). This is at odds with our our observation in section 5.5.3 that the HSV model should condense in the zero-density limit, or that at the very least the critical density is anomalously small. To resolve this issue we have to understand how the ZRP density is related to that of the HSV model.

A closer look at the mapping

In our HSV model we consider a domain to be an uninterrupted sequence of solutes and vacancies. We may therefore represent our model as an exclusion process (hereafter us) where solutes and vacancies are both particles of the same species and hosts are empty sites, see Fig. 5.17b. As a result we have

$$N_{us} = N_s + N_v \ , \qquad L_{us} = N_s + N_v + N_h = N \ . \tag{5.54}$$

We map this to a ZRP (Fig. 5.17a) by having all particles put on the next

empty site to their right. The result is

$$N_{GS} = N_{us} \ , \qquad L_{GS} = L_{us} - N_{us} = (1 - \rho_{us}) L_{us} \ , \tag{5.55}$$

where the GS subscript is a reference to the authors of [49]. As a result we find that the densities are related through

$$\rho_{GS} = \frac{N_{us}}{(1 - \rho_{us}) L_{us}} = \frac{\rho_{us}}{1 - \rho_{us}} \ , \tag{5.56}$$

$$\rho_{us} = \frac{\rho_{GS}}{1 + \rho_{GS}} \ . \tag{5.57}$$

Note that whereas $\rho_{us} \in [0, 1]$ we have that $\rho_{GS} \in [0, \infty]$. From this mapping we observe that the hop rates are defined in the same way in both pictures.

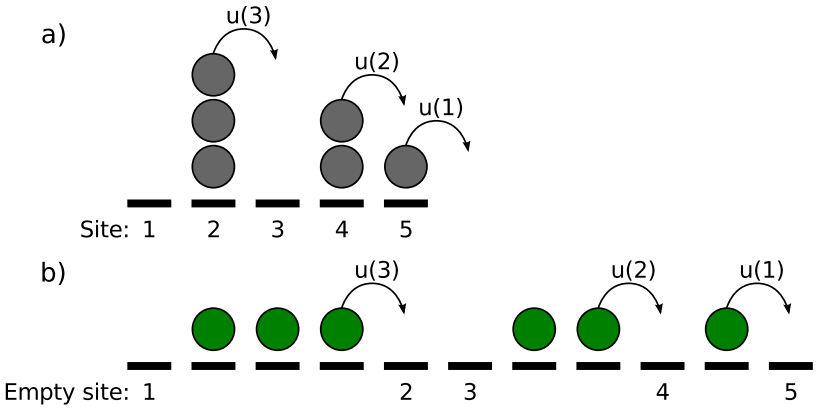

Figure 5.17: Mapping between a ZRP process (a) and our multi-particle process (b). Note that in (b) the particles represent solutes or vacancies and the empty sites are hosts.

The density dependence of HSV hop rates

We argued that the effective hop rates of the HSV model are described by equation (5.53) where, for clarity, we now attach a subscript to the position of the step, k^*_{us}. Note that subscripts are not strictly necessary since we observed that the rates, and therefore also k^*, are defined in the same way in both pictures. By comparing the position of the step at different densities, and for two system sizes,

we find (see Fig. 5.18) that the position is given by the expression

$$k^*_{us}/L_{us} = \alpha_0 \rho_{us} - \epsilon \ , \tag{5.58}$$

which we can rearrange to give

$$k^*_{us} = \left(\alpha_0 - \frac{\epsilon}{\rho_{us}}\right) N_{us} \ , \tag{5.59}$$

where α_0 and ϵ are positive parameters.

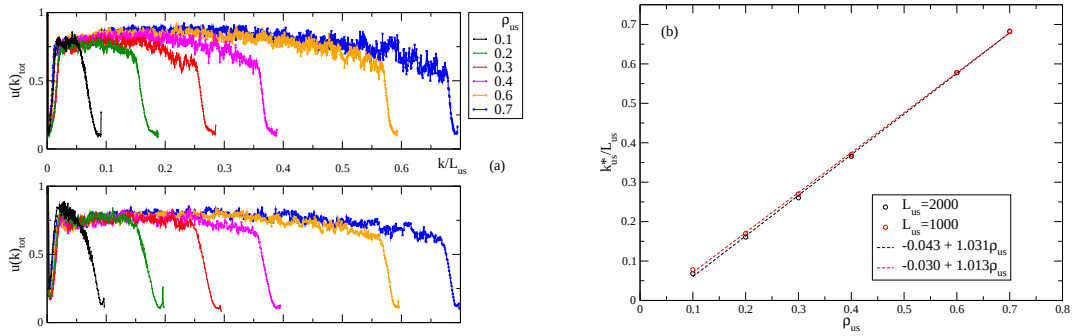

Figure 5.18: (a) Hop rates against fractional occupancy for systems at different densities, all for $g = 200.0$, $f_s = 1.25$. The top image shows a systems of size $L_{us} = 2000$ and the bottom one of size $L_{us} = 1000$. (b) A plot of the fractional step position k^*/L_{us} for the different densities shown in (a). Linear fits (dashed lines) have been added for each of the two system sizes.

The plot indicates that $\alpha_0 \sim 1$ and $\epsilon \sim 0$. However the constraint $k^*_{us} \in [0, N_{us}]$ requires that the bracket in (5.59) obeys

$$0 \leq \left(\alpha_0 - \frac{\epsilon}{\rho_{us}}\right) \leq 1 \ . \tag{5.60}$$

Thus there appears to be two separate possibilities. Either $\epsilon = 0$, thus requiring $\alpha_0 \leq 1$, or $\epsilon > 0$ in which case there will always exist some small ρ_{us} below which (5.60), and thus (5.59), does not hold. Also note that $\alpha_0 = 1$ and $\epsilon = 0$ is equivalent to letting $k^*_{us} = N_{us}$ i.e. a situation where there is no step in the hop rate.

We further note that for the HSV model c_0 appears to be a decreasing function of increasing ρ_{us} whilst c_1 appears to remain constant, Fig. 5.19.

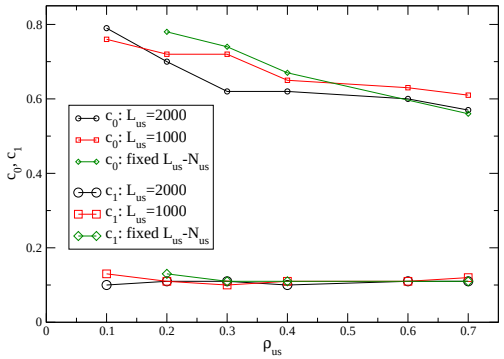

Figure 5.19: The rates c_0 and c_1 plotted against ρ_{us}. This was done for three separate measurements. For fixed system sizes of $L_{us} = 1000$, 2000 and for one realisation where L_{us} is varied whilst $L_{us} - N_{us}$ was kept fixed.

Known results from Großkinsky & Schütz 2008 (GS)

In [49] a ZRP with hop rates of the form (5.53) was considered. In their model the step position is defined to be proportional to the number of particles in the system,

$$k^*_{GS} = a_{GS} N_{GS} \ , \tag{5.61}$$

where $a_{GS} \in [0, 1)$. The phase transitions for such a system were found and illustrated by the phase diagram which is reproduced here, Fig. 5.20.

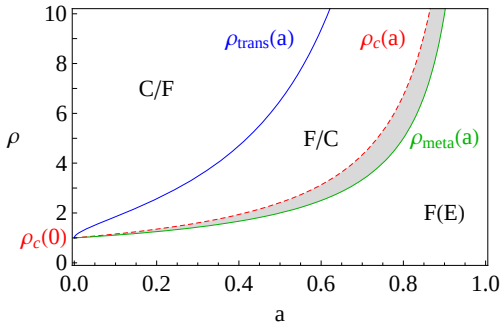

Figure 5.20: Stationary phase diagram for a ZRP with hop rates defined by (5.53) and (5.61) (density on the vertical- and a_{GS} on the horizontal axis). Here depicted for $c_0 = 2.0$, $c_1 = 1.0$. C/F is the condensed phase, F(E) the fluid phase and F/C is a metastable phase. The fluid and metastable phase overlap in the shaded region. Image reproduced from [49].

We note that there are three phases and, since two of them partially overlap, three critical densities. In terms of decreasing density we go from a state with

a condensate in a fluid background to a metastable state at $\rho_{GS,trans}$. The metastable state has a lifetime exponential in the system size. For densities below $\rho_{GS,meta}$ we are in a fluid state. Finally for densities above $\rho_{GS,meta}$ but below $\rho_{GS,c}$ we are in an overlap region between the metastable state and the fluid state. For our purposes the critical densities may be defined through:

$$\rho_{GS,c}(a_{GS}) = \frac{c_1^{1-a_{GS}}}{c_0^{1-a_{GS}} - c_1^{1-a_{GS}}} , \tag{5.62}$$

$$\rho_{GS,meta}(a_{GS}) = \frac{\rho_{GS,c}(0)}{1-a_{GS}} , \tag{5.63}$$

$$\rho_{GS,trans}(a_{GS}) \geq \rho_{GS,c}(a_{GS}) + a_{GS}\rho_{GS} . \tag{5.64}$$

Bringing the two pictures together

To resolve the issue of low-density condensation we thus require a situation whereby the critical densities in the GS picture decrease with decreasing particle density when viewed in the HSV (us) picture. To bring the GS and the HSV pictures together we combine the knowledge that the rates, and thus the step position, are defined in the same way in both pictures with (5.55) to find

$$\frac{k^*_{GS}}{N_{GS}} = \frac{k^*_{us}}{N_{us}} , \tag{5.65}$$

i.e. that the step position as the fraction of the maximum occupancy means the same thing in both pictures. Thus comparing (5.61) and (5.59) we find that

$$a_{GS} = \alpha_0 - \frac{\epsilon}{\rho_{us}} . \tag{5.66}$$

We may now use the density relation in (5.57) to write (5.62) as

$$\rho_{us,c} = \frac{\rho_{GS,c}}{1+\rho_{GS,c}} = \left[\frac{c_1}{c_0}\right]^{1-a_{GS}} . \tag{5.67}$$

Thus bringing in the identification of a_{GS} from (5.66) we find

$$\rho_{us,c}(\rho_{us}) = \left[\frac{c_1}{c_0(\rho_{us})}\right]^{1-\alpha_0+\frac{\epsilon}{\rho_{us}}} , \tag{5.68}$$

where the c_0 dependency on ρ_{us} (see Fig. 5.19) has now been made explicit. Observe that the equation for the critical density is now itself a function of density. Thus this, and the equations below, become self-consistent equations for which solutions may not exist.

We may now consider the two separate cases of a zero or non-zero ϵ. If $\epsilon = 0$ then per (5.60) it follows that we have $\alpha_0 \leq 1$. Then (5.68) reduces to

$$\rho_{us,c}(\rho_{us}) \sim c_0(\rho_{us})^{\alpha_0 - 1} \ . \tag{5.69}$$

Thus as ρ_{us} is decreased, c_0 increases and so the critical density $\rho_{us,c}$ also decreases. However we know from our results, Fig. 5.18b, that $\alpha \sim 1$ and it thus follows that, since the exponent is very small, $\rho_{us,c} \sim 1 > \rho_{us}$.

If $\epsilon > 0$ then (5.68), for $\alpha_0 \sim 1$ and small ρ_{us}, may be approximated by

$$\rho_{us,c}(\rho_{us}) \sim c_0(\rho_{us})^{-\frac{\epsilon}{\rho_{us}}} \ . \tag{5.70}$$

Again we find that $\rho_{us,c}$ decreased with ρ_{us}. However using the values for $c_0(\rho_{us})$ (Fig. 5.19) and ϵ (Fig. 5.18b) we find that $\rho_{us,c} > \rho_{us}$ for the $\rho_{us} \in [0.1, 0.7]$. Thus even if the critical density decreases with density decrease we still find that we are below the transition line for all but the smallest particle densities.

However the important transition is that given by the critical density for condensation $\rho_{us,trans}$ (5.64). This becomes

$$\rho_{us,trans}(\rho_{us}) \geq \left[\frac{c_1}{c_0(\rho_{us})}\right]^{1-\alpha_0+\frac{\epsilon}{\rho_{us}}} + \left(\alpha_0 - \frac{\epsilon}{\rho_{us}}\right)\frac{\rho_{us}}{1-\rho_{us}} \ , \tag{5.71}$$

in the HSV picture. This density remains larger than $\rho_{us,c}$ for all $\epsilon/\rho_{us} < \alpha_0$. Thus again we are below the transition line for all but the smallest densities.

Finally we can look at the transition into metastability. This occurs at (5.63) which becomes

$$\rho_{us,meta}(\rho_{us}) = \frac{c_1}{c_0(\epsilon/\alpha_0)\left(1 - \alpha_0 + \frac{\epsilon}{\rho_{us}}\right)} \ , \tag{5.72}$$

where the ϵ/α_0 factor comes from ρ_{us} being evaluated at $a_{GS} = 0$ per (5.66). Thus the position of the metastability transition is governed by the size of $c_0(\epsilon)$. Looking at Fig. 5.19 we find that if c_0 is not linear in ρ_{us} and instead increases rapidly for small densities then $c_0(\epsilon)$ could potentially be quite large. Again we

observe that $\rho_{us,meta}$ decreases with density decrease. Thus if $c_0(\epsilon)$ is sufficiently large then this could give us a $\rho_{us,meta}$ which is always smaller than ρ_{us}. This would then put our system in the metastable/fluid overlap region of the phase diagram, Fig. 5.20.

Concluding remarks on the density mapping

Unsatisfactorily the issue of low-density condensation—observed in the HSV model but not present in the ZRP with a step in the hop rate—could not be fully resolved. We may however make two tentative explanations. The first is that the mapping is correct and that $c_0(\epsilon)$ is sufficiently large to put us in the metastable/fluid overlap region. This would then indicate that we didn't observe a proper condensate. One mechanism for this would be large finite-size effects similar to those seen in AHR.

The second explanation is that the mapping, or the identification of the step, fails to take some subtle detail into account. One such detail could be the effect of the hop rates of low-occupancy sites (small domains), something we identified as important in chapter 4. If e.g. single particles move at much higher rates than those leaving other configurations then the empty sites do not map correctly. That is as $u(1) \to \infty$ particles essentially move from one domain straight to the next and in the ZRP picture we thus have $N_{GS} = N_{us}$, $L_{GS} \to N_{us}$ and so $\rho_{GS} \to 1$ for any ρ_{us}. We would therefore always find ourselves above the condensation transition line. The transition, as observed in the HSV model, would then rely on the binding energy and driving making $u(1)$ sufficiently small for the current mapping of empty sites to become appropriate.

5.7 Conclusion

In this chapter I have introduced a two-species driven exclusion process with an anti-ferromagnetic binding energy between one of the species (the solute) and vacant sites. The HSV model was inspired by the observation of reverse mass transfer in a two-dimensional model for electromigration. Unexpectedly we find that our model does not exhibit reverse mass transfer of the host species, it does however exhibit a condensation transition. The condensate exhibits internal structure and we thus identify three separate steady-states for the model: a fluid

phase where the particles move independently; a solid phase where the solutes form a condensate; a stripy phase where a condensate is made up of alternating solutes and vacancies.

I investigate how these three phases depend on two particular parameters, the binding energy and the driving force on the solute species. To do this I consider two measures of condensation the first of which is the largest separation between two consecutive solutes. I also introduce a new measure, the window scanner method, a measure which does not invoke any *ad hoc* definition of what type of object qualifies as a condensate. Together with a measure of the total energy these two approaches allow us to sketch out a phase diagram and investigate the transitions. We find that there is a rapid (potentially discontinuous) transition when going from the fluid to any of the condensed phases. By contrast the transition between the solid and the stripy condensate is smooth and involves a co-existence regime. It is therefore unclear whether the solid and stripy structures are distinct phases or just different regimes within one phase. It is further unclear whether the HSV model exhibits a condensation transition in the thermodynamic limit.

To clarify these issues and better understand the phase diagram we develop an algorithm for constructing an effective description of continuous-time processes as a zero-range process (ZRP). Reducing the HSV model to a ZRP allows us to measure an effective hop rate $u(k)$ which is compared with the known condensation requirement for the ZRP. We find that the hop rates have a different form to that of an ordinary ZRP, instead scaling with system size, $u(k) = f(k/N)$, when in either of the condensed phases. This suggests that there is only one condensed phase of which the solid phase is a special instance.

Needing a different mechanism by which the condensation occurs we observe that there appears to be a downward step in the hop rate. I therefore suggest that the effective hop rate may be described by the form

$$u(k) = \begin{cases} u_1 & \text{for } k < k^* \,, \\ u_2 & \text{for } k \geq k^* \,, \end{cases} \tag{5.73}$$

where k^* is proportional to the system size. Work by Evans and Großkinsky has shown that hop rates of this form result in a discontinuous condensation transition. This would therefore seem to explain the previously observed features

of the HSV model.

However we note that the transition described by Evans and Großkinsky is only present in a system with a density larger than some critical value ρ_c. In contrast we find that the HSV model undergoes condensation for small densities, even possibly in the zero-density limit. Attempts to reconcile this difference proved unfruitful and we are left with two alternatives. Either the observed condensate is merely metastable but appearing stable, due to e.g. finite-size effects, or our reduction of the HSV model to a ZRP neglected some subtle detail affecting the mapping of densities between the two pictures. One such detail may be the behaviour of small domains and thus the hop rates of the corresponding low-occupancy sites in the ZRP picture.

The study of the HSV model raises several interesting questions. The first is the lack of reverse mass transport. It would seem that either this is not possible in less than two dimensions or that our 2D-move failed to capture some part of the mechanism. One such detail may be taking the constant of proportionality $r \neq 1$. This would allow 2D-moves to become more, or less, favoured thereby changing their contribution to the overall movement of host particles. It would be of interest to investigate this further, especially if it proved possible to observe reverse mass transport in a one-dimensional system.

It is also unclear what role the drive on the host particles f_h plays in the behaviour of the HSV model. Apart from identifying that it must lie in the range $1 < f_h < f_s$ this was not something studied. It would be interesting to identify if there is a non-zero drive below which condensation is not observed. It would also be of interest to investigate the importance of the difference $(f_s - f_h)$ compared to the actual distance of f_s from equilibrium.

If the condensate is stable then we note that the HSV model displays a potentially new mechanism for condensation. The scaling phenomena of the hop rates also mean we need a different analysis whereby we cannot just look at the asymmetric hop rates as per normal. The identification of a step in the hop rates is a first attempt at such an analysis. Although this approach explains some of the observed features there remain unanswered questions with regards to low-density condensation and the origins of the internal structure of the condensate.

Chapter 6

Conclusions

In this thesis I have studied low-dimensional driven diffusive systems undergoing known non-equilibrium phase transitions. In particular I have explored how relatively simple modifications to the dynamics of these systems give rise to new and different phenomenology. To illustrate this I considered three systems in particular.

In chapter 3 we studied the driven asymmetric contact process where we saw how introducing an active boundary and asymmetry changes the behaviour of the much studied contact process. We observed how the absorbing state phase transition transforms into a transition whereby an active front may or may not propagate indefinitely far away from the boundary. In particular we observed how the velocity of this active front seemed to undergo a discontinuous transition even as the system underwent a continuous phase transition in the directed percolation universality class. We explained this apparent contradiction by an underlying travelling wave being attenuated by an envelope. The velocity of the underlying wave is continuous across the transition but appears discontinuous as the envelope is decaying below the transition. As a result we observed that the model describes a shearing of directed percolation space-time.

We also saw how the zero-range process could be modified so as to give rise to a propagating condensate. The Chipping model, chapter 4, modifies the dynamics of an asymmetric ZRP so the majority of the particles on a site depart during a single hopping event. The result is a system with a non-factorising steady-state which, in contrast to the ZRP, undergoes a condensation transition even in the low-density limit. We found that rather than condensation being contingent on

the hop rates decaying sufficiently slow with increasing occupancy, as is the case for ZRP, this model suggested a mechanism whereby this decay only needs to be slow for the smallest occupancies. Physically this takes the form of a few low-occupancy sites tailing the propagating condensate with the hop rate of the sites in this tail determining whether it may rejoin the condensate or whether it breaks apart.

The Host-Solute-Vacancy model (HSV) in chapter 5 is a two-species asymmetric driven exclusion process with an anti-ferromagnetic binding energy between one of the species and vacant sites. We found that the system undergoes a rapid (potentially discontinuous) condensation transition and that the resulting condensate has internal structure. Although this model was inspired by electromigration it may be viewed as a modification of any of several well-studied systems (section 5.2.1). In particular it may be considered a variation on AHR with anti-ferromagnetic interaction.

To better understand the HSV model we reduced it to an effective ZRP. Interestingly we found that the resultant hop rates decay faster with occupancy than is normally allowed for a condensing ZRP. Additionally the rates scale with system size which, to my knowledge, had not been observed in a similar model before. As a result we identified a different mechanism for the condensation transition, a downwards step in the hop rates at some occupancy k^* that is proportional to the system size. Just as for the Chipping model we also observed condensation in the low-density limit, which is not the case for either the AHR or the ZRP. This however appears to be at odds with known results for a ZRP with a step in the hop rate. It is therefore unclear whether the condensate is only metastable or if there is another subtle mechanism in addition to the stepped hop rate.

The work on these three systems shows how simple modifications to well-known systems can result in rich new phenomenology. The addition of an active wall and asymmetry turns the absorbing state phase transition of the contact process into a apparent discontinuous front velocity. A changed chipping kernel results in a new condensation mechanism for the zero-range process. Add asymmetry and you have a second example of a propagating front along with the possibility of zero-density condensation. Take the anti-ferromagnetic AHR model, add a kinetic constraint and asymmetric hop rates. Make the binding energy

multiplicative rather than additive and not only do we observe a new mechanism for condensation and a second possible case of zero-density condensation, but again the transition is apparently discontinuous.

Still lacking however, is an understanding of what new behaviour a given change to the dynamics will result in. For example, in each of the models we considered asymmetric hop rates. For the DACP system (section 3.4.3) we found that this is a key requirement for observing a discontinuous velocity. Similarly for the HSV model we observed that without the asymmetry we had an equilibrium system without any condensation transition (section 5.4.2). Finally for the Chipping model we observed (section 4.4.1) that, in addition to giving a propagating condensate, the asymmetry is also responsible for forcing all of the particles into the condensate. In the symmetric version there was instead, in the condensed phase, a background density of fluid particles. We also found that the condensation transition disappears as the density is decreased, in contrast to the asymmetric case where results suggested there is condensation even in the low-density limit. Thus we can isolate one change, asymmetry, which when combined with the existing dynamics gives rise to a whole score of new behaviour.

It is my belief that further research into modified dynamics and the resultant new behaviour will help us understand when a certain change in the dynamics will result in a given behaviour. Ideally this could then be taken further so that desired behaviour could be engineered through the interaction of selected dynamics. During this process of understanding we are also likely to encounter previously unseen behaviour which may prove to have untold uses.

Appendix A

Driven Asymmetric Contact Process - Appendix

A.1 Solution for the long time shape of the subcritical front

In this appendix I show the calculations involved in finding the long time density profile, (3.26), in the subcritical phase. Firstly we note that the long time subcritical equation (3.17) reduces to

$$\dot{f} = -sf' + Df'' \tag{A.1}$$

in the large x limit. That is the non-linear part decays away leaving us with a diffusive equation. This therefore suggests mapping the rescaled density distribution $f(x,t)$ to a Fokker-Planck equation

$$\dot{P}(x,t) = -\frac{\partial}{\partial x}\left(v(x,t)P\right) + \frac{\partial^2}{\partial x^2}\left(D(x,t)P\right) \ . \tag{A.2}$$

The Fokker-Plank equation (A.2) describes the time evolution of a probability distribution $P(x,t)$. Since $f(x,t)$ is a (rescaled) density distribution it should be possible to map f to P through

$$P(x,t) = -f(x,t)' \ , \tag{A.3}$$

where P would then be the probability distribution of the position of the wavefront, see Fig. A.1. Therefore if we assume that the front (in f) is, initially, sharp and centred at x_0 it follows that the initial condition for P is

$$P(x,0) = \delta(x - x_0) \; . \tag{A.4}$$

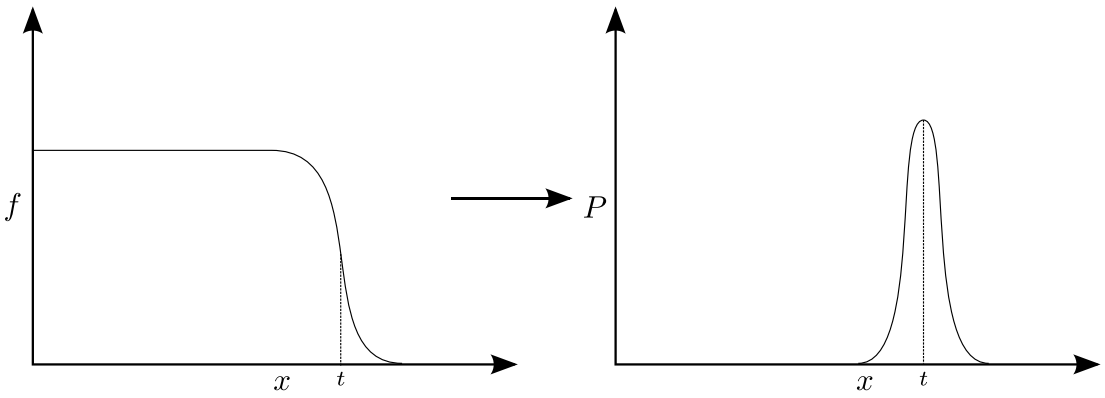

Figure A.1: Going from the (rescaled) density $f(x,t)$ to the probability distribution $P(x,t)$. For illustrative purposes the initial density decay (from the active wall) to the bulk density has been suppressed since this behaviour is unrelated to the front propagation, see Fig. 3.2 for a comparison.

Starting from (A.1) we take the derivative, with respect to x, of both sides to find

$$\dot{P} = -sP' + DP'' \; . \tag{A.5}$$

Next we have to solve for $P(x,t)$. Taking the Fourier transform,

$$\widetilde{P}(k,t) = \int_{-\infty}^{\infty} e^{-ikx} P(x,t) \mathrm{d}x \; , \tag{A.6}$$

of (A.5) and solving for $\widetilde{P}(k,t)$ gives

$$\widetilde{P}(k,t) = C \exp\left[- \left(isk + Dk^2 \right) t \right] \; . \tag{A.7}$$

C is determined by applying the initial condition, (A.4), thus giving

$$\widetilde{P}(k,t) = \exp\left[- \left(isk + Dk^2 \right) t - ikx_0 \right] \; . \tag{A.8}$$

Inverting the Fourier transform then gives the probability distribution as

$$\begin{aligned} P(x,t) &= \frac{1}{2\pi}\int_{-\infty}^{\infty} e^{ikx}\widetilde{P}(k,t)\mathrm{d}k \\ &= \frac{\exp\left[\frac{-(x-x_0-st)^2}{4Dt}\right]}{\sqrt{4\pi Dt}} \,. \end{aligned} \tag{A.9}$$

The final step is to recover the density distribution through $f(x,t) = -\int_{x^\dagger}^{x} P(x',t)\mathrm{d}x'$. Taking $x^\dagger = +\infty$ we get:

$$\begin{aligned} f(x,t) &= \frac{1}{\sqrt{4\pi Dt}}\int_{x}^{+\infty} \exp\left(\frac{-(x'-x_0-st)^2}{4Dt}\right)\mathrm{d}x' \\ &= \frac{1}{2}\,\mathrm{erfc}\left[\frac{x-x_0-st}{2\sqrt{Dt}}\right] \,. \end{aligned} \tag{A.10}$$

Thus we find that the (rescaled) density distribution for the long time subcritical case is given by:

$$f(x,t) = \frac{1}{2}\,\mathrm{erfc}\left[\frac{x-x_0-st}{2\sqrt{Dt}}\right] \,. \tag{A.11}$$

Appendix B

Host-Solute-Vacancy model - Appendices

B.1 Transfer matrix calculations for the Gap Size

These are the calculations which take us from the one-fugacity transfer matrix (5.18) to the gap size probability equation (5.36). In addition the differences necessary for a two-fugacity calculation are found in section B.1.5 and the $g = 1$ gap size calculation is done in section B.1.6.

B.1.1 Some definitions

Let x denote a site with a host (h), vacancy (v) or solute (s). And $\tilde{x}$ denote a site with a host or vacancy. The transfer-matrix (T) between two sites is then given by (5.18), namely:

$$xx \to T = \begin{pmatrix} hh & hv & hs \\ vh & vv & vs \\ sh & sv & ss \end{pmatrix} = \begin{pmatrix} z & z & z \\ 1 & 1 & g \\ 1 & g & 1 \end{pmatrix} . \tag{B.1}$$

From this we define certain other matrices which will be of use in later calculations:

$$\tilde{x}\tilde{x} \rightarrow \tilde{T} = \begin{pmatrix} z & z & 0 \\ 1 & 1 & 0 \\ 0 & 0 & 0 \end{pmatrix} ,$$

$$xsx \rightarrow S = \begin{pmatrix} 0 & 0 & z \\ 0 & 0 & g \\ 0 & 0 & 1 \end{pmatrix} \begin{pmatrix} 0 & 0 & 0 \\ 0 & 0 & 0 \\ 1 & g & 1 \end{pmatrix} = \begin{pmatrix} z & zg & z \\ g & g^2 & g \\ 1 & g & 1 \end{pmatrix} ,$$

$$xs\tilde{x} \rightarrow S_L = \begin{pmatrix} z & zg & 0 \\ g & g^2 & 0 \\ 1 & g & 0 \end{pmatrix} ,$$

$$\tilde{x}sx \rightarrow S_R = \begin{pmatrix} z & zg & z \\ g & g^2 & g \\ 0 & 0 & 0 \end{pmatrix} ,$$

$$\tilde{x}s\tilde{x} \rightarrow \tilde{S} = \begin{pmatrix} 0 & 0 & z \\ 0 & 0 & g \\ 0 & 0 & 0 \end{pmatrix} \begin{pmatrix} 0 & 0 & 0 \\ 0 & 0 & 0 \\ 1 & g & 0 \end{pmatrix} = \begin{pmatrix} z & zg & 0 \\ g & g^2 & 0 \\ 0 & 0 & 0 \end{pmatrix} ,$$

$$ss \rightarrow \begin{pmatrix} 0 & 0 & 0 \\ 0 & 0 & 0 \\ 0 & 0 & 1 \end{pmatrix} .$$

B.1.2 Eigenvalues and diagonalisation

Let P and R be matrices such that:

$$\begin{aligned} P^{-1}TP = W = \begin{pmatrix} \lambda_1 & 0 & 0 \\ 0 & \lambda_2 & 0 \\ 0 & 0 & \lambda_3 \end{pmatrix} , \\ R^{-1}\tilde{T}R = Y = \begin{pmatrix} \mu_1 & 0 & 0 \\ 0 & \mu_2 & 0 \\ 0 & 0 & \mu_3 \end{pmatrix} . \end{aligned} \tag{B.2}$$

Where λ_i (μ_i) are the eigenvalues of T ($\tilde{T}$), with the subscript i increasing as the size of the eigenvalues decrease. Thus the notation is slightly different to that in (5.19) where the eigenvalues/vectors of T, and thus P, were calculated. We therefore clarify that with respect to the previous notation: $\lambda_1 = \lambda_{\max}$, $\lambda_2 = \lambda_-$ and $\lambda_3 = \lambda_0$.

For $\tilde{T}$ we find $\mu_1 = z + 1$, $\mu_2 = \mu_3 = 0$ and thus we find

$$R = \begin{pmatrix} z & 0 & -1 \\ 1 & 0 & 1 \\ 0 & 1 & 0 \end{pmatrix} , \qquad R^{-1} = \begin{pmatrix} 1/(1+z) & 1/(1+z) & 0 \\ 0 & 0 & 1 \\ -1/(1+z) & z/(1+z) & 0 \end{pmatrix} . \tag{B.3}$$

B.1.3 Some useful results

By matrix multiplication and comparison we find the following results which I shall refer to in the gap size calculation:

$$S_L\tilde{T} = S\tilde{T} , \qquad \tilde{T}S_R = \tilde{T}S , \tag{$*$}$$

$$\tilde{T}\tilde{S}\tilde{T} = \tilde{T}S\tilde{T} , \tag{$**$}$$

$$xssx \to \begin{pmatrix} 0 & 0 & z \\ 0 & 0 & g \\ 0 & 0 & 1 \end{pmatrix} \begin{pmatrix} 0 & 0 & 0 \\ 0 & 0 & 0 \\ 0 & 0 & 1 \end{pmatrix} \begin{pmatrix} 0 & 0 & 0 \\ 0 & 0 & 0 \\ 1 & g & 1 \end{pmatrix} = S , \tag{$\dagger$}$$

$$\tilde{x}ss\tilde{x} \to \begin{pmatrix} 0 & 0 & z \\ 0 & 0 & g \\ 0 & 0 & 0 \end{pmatrix} \begin{pmatrix} 0 & 0 & 0 \\ 0 & 0 & 0 \\ 0 & 0 & 1 \end{pmatrix} \begin{pmatrix} 0 & 0 & 0 \\ 0 & 0 & 0 \\ 1 & g & 0 \end{pmatrix} = \tilde{S} , \tag{$\ddagger$}$$

$$S_L S_R = (z + g^2)S , \tag{$\star$}$$

$$S\tilde{T}^x S = SRY^x R^{-1} S = SR \begin{pmatrix} (z+1)^x & 0 & 0 \\ 0 & 0 & 0 \\ 0 & 0 & 0 \end{pmatrix} R^{-1} S = (z+g)^2 (z+1)^{x-1} S . \tag{$\star\star$}$$

B.1.4 Gap size calculation

Now consider a periodic one-dimensional lattice with N sites. Let n be the distance from a solute at the first site to the next site with a solute:

$$\overbrace{xs\underbrace{\tilde{x}\tilde{x}\ldots\tilde{x}\tilde{x}s}_{n}xx\ldots x}\,, \tag{B.4}$$

where the first and last x have been connected to illustrate that this is the same site (i.e., the 0^{th} and the N^{th} site) seen twice due to periodic boundary conditions.

Then for $2 < n < N-1$ the partition function for the configurations in (B.4) becomes

$$\begin{aligned}\mathcal{Z} &= \mathrm{tr}\left[S_L\tilde{T}^{n-2}S_RT^{N-n-2}\right] \overset{*}{=} \mathrm{tr}\left[S\tilde{T}^{n-2}ST^{N-n-2}\right] \overset{\star\star}{=} \\ &\overset{\star\star}{=} \mathrm{tr}\left[a(n)ST^{N-n-2}\right] = a(n)\,\mathrm{tr}\left[SPW^{N-n-2}P^{-1}\right] \\ &= a(n)\,\mathrm{tr}\left[MW^{N-n-2}\right]\ .\end{aligned} \tag{B.5}$$

Where $a(n) = (z+g)^2(z+1)^{n-3}$ and $M = P^{-1}SP$. The factor -2 in the powers of $\tilde{T}$ and T comes from the fact that S_L and S_R both include an $\tilde{x}$ and an x. The symbols over the equality signs indicate the results from section B.1.3 which were applied. The last equality comes from using the cyclic property of the trace.

For $n = 1$ the configurations are described by

$$\overbrace{xssxx\ldots x}\,, \tag{B.6}$$

which gives a partition function of the form

$$\mathcal{Z} \overset{\dagger}{=} \mathrm{tr}\left[ST^{N-3}\right] = \mathrm{tr}\left[MW^{N-3}\right] = 1\,\mathrm{tr}\left[MW^{N-n-2}\right]\ . \tag{B.7}$$

Whereas for $n = 2$ the configurations and the resulting partition function are

$$\overbrace{xs\tilde{x}sxx\ldots x}\,,$$

$$\mathcal{Z} = \mathrm{tr}\left[S_LS_RT^{N-4}\right] \overset{\star}{=} \mathrm{tr}\left[(z+g^2)ST^{N-4}\right] = (z+g^2)\,\mathrm{tr}\left[MW^{N-n-2}\right]\ . \tag{B.8}$$

And for $n = N-1$ they are

$$\overbrace{ss\tilde{x}\tilde{x}\ldots\tilde{x}s} = \overbrace{\tilde{x}ss\tilde{x}\ldots\tilde{x}}\,,$$

$$\begin{aligned}\mathcal{Z} &\overset{\ddagger}{=} \mathrm{tr}\left[\tilde{S}\tilde{T}^{N-3}\right] \overset{**}{=} \mathrm{tr}\left[S\tilde{T}^{N-3}\right] = \mathrm{tr}\left[S\tilde{T}^{n-2}\right] \\ &= (z+g)(z+1)^{n-3}\,\mathrm{tr}\begin{pmatrix} z & z & 0 \\ g & g & 0 \\ 1 & 1 & 0 \end{pmatrix} = (z+g)^2(z+1)^{n-3}\,,\end{aligned} \tag{B.9}$$

where the second to last step can be shown using the proof for $(\star\star)$.

Finally for $n = N$ the configurations and the partition function are

$$\overbrace{\tilde{x}s\tilde{x}\tilde{x}\ldots\tilde{x}}\,,$$

$$\mathcal{Z} = \mathrm{tr}\left[\tilde{S}\tilde{T}^{N-2}\right] \overset{**}{=} \mathrm{tr}\left[S\tilde{T}^{N-2}\right] = \mathrm{tr}\left[S\tilde{T}^{n-2}\right] = (z+g)^2(z+1)^{n-3}\,. \tag{B.10}$$

We note that $n = N$ (and $N-1$) requires there to be only one (two) solutes in the system. If we have N_s solutes there is therefore a maximum possible separation given by $n_{\max} = N - N_s + 1$. Comparing the case when $n = n_{\max}$ with our calculation for $n = N-1$ we find that the only difference is the introduction of more ss terms which per (†) and (‡) therefore give the same result as that for $n = N-1$ and $n = N$. Thus we summarise all the cases by:

$$\begin{aligned}\mathcal{Z}(n) &= \begin{cases} a(n) & \text{for } n = n_{\max}\,, \\ a(n)\,\mathrm{tr}\left[MW^{N-n-2}\right] & \text{for } n < n_{\max}\,. \end{cases} \\ a(n) &= \begin{cases} (z+g)^2(z+1)^{n-3} & \text{for } n > 2\,, \\ (z+g^2) & \text{for } n = 2\,, \\ 1 & \text{for } n = 1\,. \end{cases}\end{aligned} \tag{B.11}$$

Here the probability of finding a gap of size n is defined as

$$P(n) = \frac{A\mathcal{Z}(n)}{\mathrm{tr}\left[ST^{N-2}\right]} = \frac{A\mathcal{Z}(n)}{\mathrm{tr}\left[MW^{N-2}\right]}\,, \tag{B.12}$$

where the term in the denominator describes any configuration with a solute at the first site. A is a normalisation factor defined through

$$\sum_{n=1}^{n_{\max}} P(n) = 1\,. \tag{B.13}$$

For the case where $n < n_{\max}$ this simplifies further

$$\begin{aligned} P(n) =& Aa(n)\frac{M_{11}\lambda_1^{N-n-2} + M_{22}\lambda_2^{N-n-2} + M_{33}\lambda_3^{N-n-2}}{M_{11}\lambda_1^{N-2} + M_{22}\lambda_2^{N-2} + M_{33}\lambda_3^{N-2}} \\ =& Aa(n)\lambda_1^{-n}\frac{M_{11} + M_{22}\left(\frac{\lambda_2}{\lambda_1}\right)^{N-n-2} + M_{33}\left(\frac{\lambda_3}{\lambda_1}\right)^{N-n-2}}{M_{11} + M_{22}\left(\frac{\lambda_2}{\lambda_1}\right)^{N-2} + M_{33}\left(\frac{\lambda_3}{\lambda_1}\right)^{N-2}} \ . \end{aligned} \tag{B.14}$$

Since λ_1 is the largest of the eigenvalues (which we called $\lambda_{\max}$ in the energy calculation) this becomes

$$\lim_{N\to\infty} P(n) = Aa(n)\lambda_1^{-n} \tag{B.15}$$

in the thermodynamic limit.

Similarly for $n = n_{\max} = N\left(\frac{1+\rho_h}{2}\right) + 1$, where ρ_h is the density of host sites, we get

$$P(n_{\max}) = \frac{Aa(n_{\max})\lambda_1^{2-N}}{M_{11} + M_{22}\left(\frac{\lambda_2}{\lambda_1}\right)^{N-2} + M_{33}\left(\frac{\lambda_3}{\lambda_1}\right)^{N-2}} \ , \tag{B.16}$$

where M_{ii} are the diagonal entries of $M = P^{-1}SP$ given by

$$\begin{pmatrix} \frac{G_{(++)}\Gamma_+}{8\sqrt{B}} & \frac{zG_{(-+)}(g-1)}{4\sqrt{B}} & -\frac{\Gamma_+(g-1)}{4\sqrt{B}} \\ -\frac{zG_{(--)}(g-1)}{4\sqrt{B}} & -\frac{G_{(+-)}\Gamma_-}{8\sqrt{B}} & \frac{\Gamma_-(g-1)}{4\sqrt{B}} \\ -\frac{G_{(++)}(g-1)}{4} & -\frac{G_{(+-)}(g-1)}{4} & \frac{(g-1)^2}{2} \end{pmatrix} \tag{B.17}$$

where

$$\begin{aligned} G_{(\pm\pm)} &= (z \pm g + 1 \pm \sqrt{B}) \ , \\ \Gamma_\pm &= (3z - zg + (g+1)^2 \pm (g+1)\sqrt{B}) \ . \end{aligned} \tag{B.18}$$

B.1.5 Two fugacities

If the transfer-matrix T also includes a second fugacity y then equations ($\star$) and ($\star\star$) in section B.1.3 are slightly modified. Instead we find that

$$\begin{aligned} S_L S_R &= (z + yg^2)S \ , \\ S\tilde{T}^x S &= (z + yg)^2(z + y)^{x-1}S \ . \end{aligned} \tag{B.19}$$

The remaining results remain true although the matrices T, S, M and W, and their eigenvalues, are obviously changed.

As a result (B.11) is slightly changed and becomes:

$$a(n) = \begin{cases} (z+yg)^2(z+y)^{n-3} & \text{for } n > 2 \ , \\ (z+yg^2) & \text{for } n = 2 \ , \\ 1 & \text{for } n = 1 \ . \end{cases} \tag{B.20}$$

B.1.6 Random distribution

For a completely random distribution ($f_s = f_h = 1.0$ and $g = 1$) the gap size calculations simplify greatly. The eigenvalues of T become $\lambda_1 = z + 2$ and $\lambda_2 = \lambda_3 = 0$ and thus $\mathcal{Z} = \lambda_{\max}^N$ exactly. Further this means that

$$a(n) = \begin{cases} (z+1)^{n-1} & \text{for } n > 2 \ , \\ (z+1) & \text{for } n = 2 \ , \\ 1 & \text{for } n = 1 \ , \end{cases} \tag{B.21}$$

which reduces to $a(n) = (z+1)^{n-1}$. Also $\operatorname{tr} MW^x = M_{11}(z+2)^x$ where $M_{11} = (z+2)$. And so we find that the probability distribution, Fig. B.1, becomes

$$P(n) = \begin{cases} Aa(n)(z+2)^{-n} & \text{for } n < n_{\max} \ , \\ Aa(n)(z+2)^{1-N} & \text{for } n = n_{\max} \ . \end{cases} \tag{B.22}$$

B.2 Step in hop rate gives condensation

Based on the observations in section 5.6.2 we consider the hop rates (in the stripy and solid phase) taking the form

$$u(n) = \begin{cases} 1 & \text{for } \ n < r \ , \\ \beta & \text{for } \ n \geq r \ . \end{cases} \tag{B.23}$$

with $\beta < 1$ and r proportional to the system size, $r = \alpha N$. Following the calculations in [33] I will here show that a hop rate of this type results in a

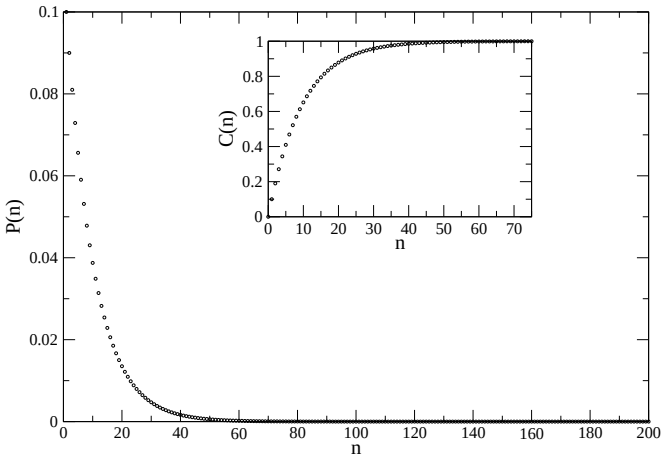

Figure B.1: The probability distribution for the distance between solutes for a randomly distributed system with $N = 1000$ and $\rho_s = 0.1$. The inset shows the cumulative probability against separation.

condensation transition. For simplicity we have taken the larger of the rates to be 1, however the calculations below hold for any finite value larger than β.

Assume that the homogeneous system can be described by a zero-range style process. Then, recall the condensation requirement from section 2.3.2, that the system supports a condensation transition in ρ only if ρ_c is finite. The critical density, in the thermodynamic limit, is given by

$$\rho_c = \lim_{z \to \beta'} = \frac{zF'(z)}{F(z)} \tag{B.24}$$

for

$$F(z) = \sum_{n=0}^{\infty} z^n \prod_{i=1}^{n} u(i)^{-1} \tag{B.25}$$

where β' is the radius of convergence of $F(z)$. Thus β' is the limiting value on $u(n)$ which, per (B.23), corresponds to β.

Returning to the hop rates in question, equation (B.23), we find that

$$F(z) = \sum_{n=0}^{r-1} z^n + \sum_{n=r}^{\infty} z^n \beta^{r-n-1} \tag{B.26}$$

which after performing the geometric series yields

$$\begin{aligned} F(z) &= \frac{1-z^r}{1-z} + \frac{z^r}{\beta - z} \,, \\ F'(z) &= \frac{1-z^r}{(1-z)^2} - \frac{rz^{r-1}}{1-z} + \frac{z^r}{(\beta-z)^2} + \frac{rz^{r-1}}{\beta - z} \,. \end{aligned} \tag{B.27}$$

As r is proportional to the system size N it follows that in the thermodynamic limit $r \to \infty$. Since $z < 1$ we therefore find that (B.24) reduces to

$$\rho_c = \lim_{z\to\beta} \lim_{r\to\infty} \frac{F'(z)}{F(z)} = \lim_{z\to\beta} (1-z)^{-1} = (1-\beta)^{-1} < \infty \,, \tag{B.28}$$

and we therefore have a condensation transition in the system.

Bibliography

[1] Andjel, E. D. Invariant measures for the zero range process. *Ann. Probab.* (1982), 525–547.

[2] Andjel, E. D., Bramson, M. D., and Liggett, T. M. Shocks in the asymmetric exclusion process. *Probab. Theory Relat. Fields 78* (1988), 231–247.

[3] Arndt, P. F., Heinzel, T., and Rittenberg, V. Spontaneous breaking of translational invariance in one-dimensional stationary states on a ring. *J. Phys. A: Math. Gen. 31*, 2 (1998), L45–L51.

[4] Arndt, P. F., Heinzel, T., and Rittenberg, V. Spontaneous breaking of translational invariance and spatial condensation in stationary states on a ring. I. The neutral system. *J. Stat. Phys. 97* (1999), 1–65.

[5] Arnold, R., Showalter, K., and Tyson, J. J. Propagation of chemical reactions in space. *J. Chem. Educ. 64*, 9 (1987), 740–742.

[6] Aronson, D. G., and Weinberger, H. F. Nonlinear diffusion in population genetics, combustion, and nerve pulse propagation. *Lect. Notes Math. 446* (1975), 5–49.

[7] Aronson, D. G., and Weinberger, H. F. Multidimensional nonlinear diffusion arising in population genetics. *Adv. Math. 30*, 1 (1978), 33–76.

[8] Baierlein, R. *Thermal physics*. Cambridge Univ. Press, 1999.

[9] Barrett-Freeman, C. *Effects of Advection on Non-Equilibrium Systems*. PhD thesis, University of Edinburgh, 2011.

[10] Barrett-Freeman, C., Evans, M. R., Marenduzzo, D., and Poon, W. C. K. Nonequilibrium phase transition in the sedimentation of reproducing particles. *Phys. Rev. Lett. 101*, 10 (2008), 100602.

[11] Barrett-Freeman, C., Evans, M. R., Marenduzzo, D., and Tailleur, J. The role of noise and advection in absorbing state phase transitions. *Europhys. Lett. 90*, 1 (2010), 16003.

[12] Baxter, R. J. *Exactly solved models in statistical mechanics*. Academic Press, 1982.

[13] Bayer, R. Symmetric binary B-Trees: Data structure and maintenance algorithms. *Acta Inform. 1* (1972), 290–306.

[14] Bezuidenhout, C., and Grimmett, G. The critical contact process dies out. *Ann. Probab. 18*, 4 (1990), 1462–1482.

[15] Blythe, R. A. *Nonequilibrium phase transitions and dynamical scaling regimes.* PhD thesis, University of Edinburgh, 2001.

[16] Blythe, R. A., and Evans, M. R. Slow crossover to Kardar-Parisi-Zhang scaling. *Phys. Rev. E 64*, 5 (2001), 051101.

[17] Blythe, R. A., and Evans, M. R. Nonequilibrium steady states of matrix-product form: a solver's guide. *J. Phys. A: Math. Theor. 40*, 46 (2007), R333.

[18] Bortz, A. B., Kalos, M. H., and Lebowitz, J. L. A new algorithm for Monte Carlo simulation of Ising spin systems. *J. Comput. Phys. 17*, 1 (1975), 10–18.

[19] Broadbent, S. R., and Hammersley, J. M. Percolation processes I. Crystals and mazes. *Mathematical Proceedings of the Cambridge Philosophical Society 53*, 3 (1957), 629–641.

[20] Bruce, A. D., and Wilding, N. B. Scaling fields and universality of the liquid-gas critical point. *Phys. Rev. Lett. 68* (1992), 193–196.

[21] Burda, Z., Johnston, D., Jurkiewicz, J., Kamiński, M., Nowak, M., Papp, G., and Zahed, I. Wealth condensation in pareto macroeconomies. *Phys. Rev. E 65*, 2 (2002), 026102.

[22] Chen, C.-C., Park, H., and den Nijs, M. Active width at a slanted active boundary in directed percolation. *Phys. Rev. E 60*, 3 (1999), 2496–2500.

[23] Chowdhury, D., Santen, L., and Schadschneider, A. Statistical physics of vehicular traffic and some related systems. *Phys. Rep. 329*, 46 (2000), 199–329.

[24] Cocozza-Thivent, C. Processus des misanthropes. *Probab. Theory Relat. Fields 70* (1985), 509–523.

[25] Costa, A., Blythe, R. A., and Evans, M. R. Discontinuous transition in a boundary driven contact process. *J. Stat. Mech. 2010*, 09 (2010), P09008.

[26] Costa, A., Blythe, R. A., and Evans, M. R. In preparation, 2012.

[27] Dekker, J. P., Volkert, C. A., Arzt, E., and Gumbsch, P. Alloying effects on electromigration mass transport. *Phys. Rev. Lett. 87*, 3 (2001), 035901.

[28] Derrida, B., Evans, M. R., Hakim, V., and Pasquier, V. Exact solution of a 1d asymmetric exclusion model using a matrix formulation. *J. Phys. A: Math. Gen. 26*, 7 (1993), 1493–1517.

[29] Derrida, B., and Simon, D. The survival probability of a branching random walk in presence of an absorbing wall. *Europhys. Lett. 78*, 6 (2007), 60006.

[30] Durrett, R. *Lecture Notes on Particle Systems and Percolation.* Wadsworth & Brooks/Cole, 1988.

[31] Eggers, J. Sand as Maxwell's demon. *Phys. Rev. Lett. 83*, 25 (1999), 5322–5325.

[32] Evans, M. R. Bose-Einstein condensation in disordered exclusion models and relation to traffic flow. *Europhys. Lett. 36*, 1 (1996), 13–18.

[33] Evans, M. R. Phase transitions in one-dimensional nonequilibrium systems. *Braz. J. Phys. 30*, 1 (2000), 42–57.

[34] Evans, M. R., and Hanney, T. Nonequilibrium statistical mechanics of the zero-range process and related models. *J. Phys. A: Math. Gen. 38*, 19 (2005), R195.

[35] Evans, M. R., Levine, E., Mohanty, P. K., and Mukamel, D. Modelling one-dimensional driven diffusive systems by the zero-range process. *Eur. Phys. J. B 41* (2004), 223–230.

[36] Evans, M. R., Majumdar, S. N., and Zia, R. K. P. Factorized steady states in mass transport models. *J. Phys. A: Math. Gen. 37*, 25 (2004), L275.

[37] Fisher, R. A. The wave of advance of advantageous genes. *Ann. Eugen. 7* (1937), 353–369.

[38] Frobenius, G. *Über Matrizen aus nicht negativen Elementen.* Königliche Akademie der Wissenschaften, 1912.

[39] Fröjdh, P., Howard, M., and Lauritsen, K. B. Directed percolation and other systems with absorbing states: Impact of boundaries. *Int. J. Mod. Phys. B 15*, 12 (2001), 1761–1798.

[40] Gibbs, J. W. *The elementary principles in statistical mechanics.* Scribner, 1902.

[41] Gibson, M. A., and Bruck, J. Efficient exact stochastic simulation of chemical systems with many species and many channels. *J. Phys. Chem. A 104*, 9 (2000), 1876–1889.

[42] Gillespie, D. T. A general method for numerically simulating the stochastic time evolution of coupled chemical reactions. *J. Comp. Phy. 22*, 4 (1976), 403–434.

[43] Godrèche, C. Dynamics of condensation in zero-range processes. *J. Phys. A: Math. Gen. 36*, 23 (2003), 6313–6328.

[44] Godrèche, C., and Luck, J. M. Dynamics of the condensate in zero-range processes. *J. Phys. A: Math. Gen. 38*, 33 (2005), 7215–7237.

[45] Goldenfeld, N. *Lectures on phase transitions and the renormalization group.* Addison-Wesley, 1992.

[46] Grassberger, P. On phase transitions in Schlögl's second model. *Z. Phys. B 47*, 4 (1982), 365–374.

[47] Grassberger, P., and de la Torre, A. Reggeon field theory (Schlögl's first model) on a lattice: Monte Carlo calculations of critical behaviour. *Ann. Phys. 122*, 2 (1979), 373–396.

[48] Grassberger, P., and Zhang, Y. C. "Self-organized" formulation of standard percolation phenomena. *Physica A 224*, 1 (1996), 169–179.

[49] Grosskinsky, S., and Schütz, G. M. Discontinuous condensation transition and nonequivalence of ensembles in a zero-range process. *J. Stat. Phys. 132* (2008), 77–108.

[50] Grosskinsky, S., Schütz, G. M., and Spohn, H. Condensation in the zero range process: Stationary and dynamical properties. *J. Stat. Phys. 113* (2003), 389–410.

[51] Guttmann, A. J., and Enting, I. G. Solvability of some statistical mechanical systems. *Phys. Rev. Lett. 76* (1996), 344–347.

[52] Harris, T. E. Contact interactions on a lattice. *Ann. Probab. 2* (1974), 969–988.

[53] Heger, D. A. A disquisition on the performance behavior of binary search tree data structures. *European Journal for the Informatics Professional 5* (2004), 67–75.

[54] Henkel, M., Hinrichsen, H., and Lubeck, S. *Non-Equilibrium Phase Transitions: Absorbing Phase Transitions.* Springer, 2008.

[55] Hinrichsen, H. Non-equilibrium critical phenomena and phase transitions into absorbing states. *Adv. Phys. 49*, 7 (2000), 815–958.

[56] Hinrichsen, H. On possible experimental realizations of directed percolation. *Braz. J. Phys. 30* (2000), 69–82.

[57] Howard, M. J., and Täuber, U. C. 'Real' versus 'imaginary' noise in diffusion-limited reactions. *J. Phys. A: Math. Gen. 30*, 22 (1997), 7721.

[58] Ispolatov, I., and Krapivsky, P. L. Phase transition in a traffic model with passing. *Phys. Rev. E 62* (2000), 5935–5939.

[59] Janssen, H. K. On the nonequilibrium phase transition in reaction-diffusion systems with an absorbing stationary state. *Z. Phys. B 42*, 2 (1981), 151–154.

[60] Jensen, I. Critical behavior of the three-dimensional contact process. *Phys. Rev. A 45* (1992), R563–R566.

[61] Jensen, I. Low-density series expansions for directed percolation: I. A new efficient algorithm with applications to the square lattice. *J. Phys. A: Math. Gen. 32*, 28 (1999), 5233–49.

[62] Jensen, I., and Dickman, R. Time-dependent perturbation theory for nonequilibrium lattice models. *J. Stat. Phys. 71* (1993), 89–127.

[63] Kadanoff, L. P. *Statistical physics: statics, dynamics and renormalization.* World Scientific, 2000.

[64] Kafri, Y., Levine, E., Mukamel, D., Schütz, G. M., and Török, J. Criterion for phase separation in one-dimensional driven systems. *Phys. Rev. Lett. 89*, 3 (2002), 035702.

[65] Kafri, Y., Levine, E., Mukamel, D., Schütz, G. M., and Willmann, R. D. Phase-separation transition in one-dimensional driven models. *Phys. Rev. E 68*, 3 (2003), 035101.

[66] Kafri, Y., Levine, E., Mukamel, D., and Török, J. Sharp crossover and anomalously large correlation length in driven systems. *J. Phys. A: Math. Gen. 35*, 30 (2002), L459.

[67] Katz, S., Lebowitz, J. L., and Spohn, H. Nonequilibrium steady states of stochastic lattice gas models of fast ionic conductors. *J. Stat. Phys. 34* (1984), 497–537.

[68] Knuth, D. E. *The Art of Computer Programming, Volume III: Sorting and Searching.* Addison-Wesley, 1973.

[69] Kolmogorov, A., Petrovskii, I., and Piskunov, N. Étude de l'équation de la diffusion avec croissance de la quantite de matière et son application à un problème biologique. *Bull. Univ. État Moscou A 1* (1937), 1–25.

[70] Korniss, G., Schmittmann, B., and Zia, R. K. P. Long-range order in a quasi one-dimensional non-equilibrium three-state lattice gas. *Europhys. Lett. 45*, 4 (1999), 431–436.

[71] Krug, J. Boundary-induced phase transitions in driven diffusive systems. *Phys. Rev. Lett. 67* (1991), 1882–1885.

[72] Krug, J., and Spohn, H. *Solids far from equilibrium.* Cambridge Univ. Press, Cambridge, 1992.

[73] Kundu, A., and Mohanty, P. K. Phase separation transition in a driven diffusive system with anti-ferromagnetic interaction. *Physica A 390*, 9 (2011), 1585–1590.

[74] Landau, D. P., and Binder, K. *A guide to Monte Carlo simulations in statistical physics.* Cambridge Univ. Press, 2009.

[75] Liggett, T. M. *Interacting particle systems.* Springer-Verlag, 1985.

[76] Lipowski, A., and Droz, M. Urn model of separation of sand. *Phys. Rev. E 65*, 3 (2002), 031307.

[77] Luther, R. Räumliche Fortpflanzung chemischer Reaktionen. *Z. Elektrochemie 12*, 32 (1906), 596–600.

[78] Majumdar, S. N., Krishnamurthy, S., and Barma, M. Nonequilibrium phase transitions in models of aggregation, adsorption, and dissociation. *Phys. Rev. Lett. 81* (1998), 3691–3694.

[79] Majumdar, S. N., Krishnamurthy, S., and Barma, M. Nonequilibrium phase transition in a model of diffusion, aggregation, and fragmentation. *J. Stat. Phys. 99* (2000), 1–29.

[80] Mallick, K. Shocks in the asymmetry exclusion model with an impurity. *J. Phys. A: Math. Gen. 29*, 17 (1996), 5375.

[81] Marro, J., and Dickman, R. *Nonequilibrium phase transitions in lattice models*. Cambridge Univ. Press, 1999.

[82] Matsumoto, M. Mersenne Twister home page. `http://www.math.sci.hiroshima-u.ac.jp/~m-mat/MT/emt.html`. Last visited on 2012-05-17.

[83] Matsumoto, M., and Nishimura, T. Mersenne Twister: A 623-dimensionally equidistributed uniform pseudo-random number generator. *ACM Trans. Model. Comput. Simul. 8*, 1 (1998), 3–30.

[84] Muñoz, M. A., Grinstein, G., and Tu, Y. Survival probability and field theory in systems with absorbing states. *Phys. Rev. E 56*, 5 (1997), 5101–5105.

[85] Mukamel, D. Phase transitions in non-equilibrium systems. In *Soft and Fragile Matter: Nonequilibrium Dynamics, Metastability and Flow* (2000), M. E. Cates and M. R. Evans, Eds., vol. 53 of *Scottish Universities Summer School in Physics*, Institute of Physics Publishing, Bristol, pp. 237–204.

[86] Müller, C., and Tribe, R. Stochastic pde's arising from the long-range contact and long-range voter processes. *Probab. Theory Relat. Fields 102*, 4 (1995), 519–545.

[87] Murray, J. D. *Mathematical biology*. Springer, 2003.

[88] O'Loan, O. J., and Evans, M. R. Alternating steady state in one-dimensional flocking. *J. Phys. A: Math. Gen. 32* (1999), L99.

[89] O'Loan, O. J., Evans, M. R., and Cates, M. E. Jamming transition in a homogeneous one-dimensional system: The bus route model. *Phys. Rev. E 58* (1998), 1404–1418.

[90] Perron, O. Zur Theorie der Matrices. *Math. Ann. 64* (1907), 248–263.

[91] Press, W. H., Teukolsky, S. A., Vetterling, W. T., and Flannery, B. P. *Numerical Recipes 3rd Edition: The Art of Scientific Computing.* Cambridge Univ. Press, 2007.

[92] Rajesh, R., and Majumdar, S. N. Exact phase diagram of a model with aggregation and chipping. *Phys. Rev. E 63* (2001), 036114.

[93] Rajewsky, N., Sasamoto, T., and Speer, E. R. Spatial particle condensation for an exclusion process on a ring. *Physica A 279*, 14 (2000), 123–142.

[94] Riley, K. F., Hobson, M. P., and Bence, S. J. *Mathematical methods for physics and engineering.* Cambridge Univ. Press, 1997.

[95] Sasamoto, T., and Zagier, D. On the existence of a phase transition for an exclusion process on a ring. *J. Phys. A: Math. Gen. 34*, 24 (2001), 5033.

[96] Schinazi, R. The asymmetric contact process on a finite set. *J. Stat. Phys. 74*, 5 (1994), 1005–1016.

[97] Schmittmann, B., Hwang, K., and Zia, R. K. P. Onset of spatial structures in biased diffusion of two species. *Europhys. Lett. 19*, 1 (1992), 19.

[98] Schonmann, R. H. The asymmetric contact process. *J. Stat. Phys. 44*, 3 (1986), 505–534.

[99] Schütz, G. M. Critical phenomena and universal dynamics in one-dimensional driven diffusive systems with two species of particles. *J. Phys. A: Math. Gen. 36*, 36 (2003), R339.

[100] Schütz, G. M., and Domany, E. Phase transitions in an exactly soluble one-dimensional exclusion process. *J. Stat. Phys. 72* (1993), 277–296.

[101] Showalter, K., and Tyson, J. J. Luthers 1906 discovery and analysis of chemical waves. *J. Chem. Educ. 64*, 9 (1987), 742–744.

[102] Simon, D., and Derrida, B. Quasi-stationary regime of a branching random walk in presence of an absorbing wall. *J. Stat. Phys. 131*, 2 (2008), 203–233.

[103] Smoluchowski, M. Drei Vorträge über Diffusion, Brownsche Bewegung und Koagulation von Kolloidteilchen. *Physik. Z. 17* (1916), 557–585.

[104] Spitzer, F. Interaction of Markov processes. *Adv. Math. 5*, 2 (1970), 246–290.

[105] Sweet, T. The asymmetric contact process at its second critical value. *J. Stat. Phys. 86*, 3 (1997), 749–764.

[106] Takeuchi, K. A., Kuroda, M., Chaté, H., and Sano, M. Experimental realization of directed percolation criticality in turbulent liquid crystals. *Phys. Rev. E 80*, 5 (2009), 051116.

[107] Tretyakov, A. Y., Inui, N., and Konno, N. Phase transition for the one-sided contact process. *J. Phys. Soc. Jap. 66*, 12 (1997), 3764–3769.

[108] van der Meer, D., van der Weele, K., and Lohse, D. Coarsening dynamics in a vibrofluidized compartmentalized granular gas. *J. Stat. Mech. 2004*, 04 (2004), P04004.

[109] van Saarloos, W. Front propagation into unstable states. *Phys. Rep. 386*, 2-6 (2003), 29–222.

[110] Vicsek, T., Czirók, A., Farkas, I. J., and Helbing, D. Application of statistical mechanics to collective motion in biology. *Physica A 274*, 1 (1999), 182–189.

[111] Voigt, C. A., and Ziff, R. M. Epidemic analysis of the second-order transition in the Ziff-Gulari-Barshad surface-reaction model. *Phys. Rev. E 56* (1997), R6241–R6244.

[112] Waclaw, B., and Evans, M. R. Explosive condensation in a mass transport model. *Phys. Rev. Lett. 108* (2012), 070601.

[113] Weisstein, E. W. Bertrand's test. From MathWorld—A Wolfram Web Resource. `http://mathworld.wolfram.com/BertrandsTest.html`. Last visited on 2012-05-17.

[114] Zia, R. K. P., Evans, M. R., and Majumdar, S. N. Construction of the factorized steady state distribution in models of mass transport. *J. Stat. Mech. 2004*, 10 (2004), L10001.

Publications

Costa, A. and Blythe, R. A. and Evans, M. R. Discontinuous transition in a boundary driven contact process. In *J. Stat. Mech.*, 2010.